Multi-Scale Modeling, Surrogate-Based Analysis, and Optimization of Lithium-Ion Batteries for Vehicle Applications

by

Wenbo Du

A dissertation submitted in partial fulfillment
of the requirements for the degree of
Doctor of Philosophy
(Aerospace Engineering)
in the University of Michigan
2013

Doctoral Committee:

Professor Wei Shyy, Co-Chair
Associate Professor Joaquim R. R. A. Martins, Co-Chair
Associate Professor Wei Lu
Assistant Professor Veera Sundararaghavan

To my family

Acknowledgements

This dissertation could not have been possible without the support, encouragement, and guidance of numerous colleagues, friends, classmates, and faculty members. It would be impossible to adequately acknowledge and thank everyone who has assisted me on my journey, although in this section I would like to try.

First, I would like to thank Professor Wei Shyy for welcoming me to his research group and inspiring me to pursue my academic dreams. Throughout the years, he has been an unwavering source of profound ideas and discerning discussions that have guided the course of my research, and I could not overvalue his patience during my less productive phases. I would like to thank Professor Joaquim Martins for also advising me, and for keeping a watchful eye on my research activities. I hope that this dissertation reflects the good research and writing practices that he has taught me. I would also like to thank Professors Wei Lu and Veera Sundararaghavan for agreeing to serve on my committee, and for being so accommodating.

I would like to thank Dr. Ann Marie Sastry for overseeing the founding of the ABCD research center, which has provided me with valuable opportunities to learn more about battery science and design from experts at GM and UM. I would also like to thank Professor Margaret Wooldridge for continuing to head ABCD, along with Professor Lu. And I would like to thank all of the other ABCD researchers for providing their expertise to help shape my research.

I would like to thank all of my research groupmates/labmates, classmates, and officemates for their tolerance over the years. In particular, I must thank Dr. Xiangchun Zhang, Dr. Amit Gupta, and Nansi Xue for their close research collaboration and helping to co-author several publications. I would also like to offer my sincere thanks to Mengshi Guo, who, along with Nansi Xue, worked together with me in creating the hybrid electric aircraft model and performing the corresponding mission analysis. And finally, I would also like to thank my officemates and the rest of the Shyylab and MDOLab members for

the fruitful group meetings and office discussions: Clara Ang, Dr. Hikaru Aono, Dr. Yeon Baik, Dr. Young-Chang Cho, Dr. Peter Hamlington, Dr. Ez Hassan, John Hwang, GaRam Jun, Uros Kalabic, Dr. Chang-Kwon Kang, Jason Kao, Dr. Gaetan Kenway, Chih-Kuang Kuan, Peter Lyu, Sabrina Marquina, Alex Morozov, Dr. Jaeheon Sim, Dr. Emre Sozer, Dr. Jianing Tang, Dr. Pat Trizila, Dr. Chien-Chou Tseng, Derrick Yeo, Seokjun Yun, and Dr. Daniel Zaide. Additionally, I would like to thank my friends from high school and undergrad, for keeping me optimistic and sane: Alice, Jon, Linda, Paul, Quillan, Raghav, Rohit, Simon, Stephen, and Victor.

I would like to thank Professor Greg Carman at UCLA for first giving me the idea to pursue a doctorate degree, although I must apologize to him for not seeking it in structural mechanics. In the end, I would have to agree that the educational journey, though difficult, has been worth the effort.

And finally, I must thank my parents and my sister for their endless words of encouragement and for always believing in me.

Table of Contents

List of Figures

List of Tables

List of Symbols

A	adjacency matrix or perturbation amplitude
a	surface area
b	basis function coefficient or random perturbation
C	cycling rate, capacity, or lift/drag coefficient
c	ion concentration
D	drag or diffusion coefficient
d	distance
E	energy or expected value
F	Faraday's constant
f	fuel or function
g	inequality constraint or gravitational acceleration
H	Hessian matrix
h	altitude, equality constraint, or step size
I	current
i	current density
J	volumetric reaction current
j	local reaction current density
k	constant
L	electrode thickness, lift, or Lagrangian
m	mass or number of nodes/elements
N	number of dimensions, variables, etc.
P	power
Q	charge/capacity
R	particle radius, resistance, or correlation function
R^2	coefficient of determination

r	radial dimension
S	sensitivity index or reference area
s	engine speed
T	thrust or temperature
t	time or transference number
Th	throttle setting
U_{OCP}	open circuit potential
U_{OCV}	open circuit voltage
V	voltage/potential, velocity, variance, or volume
W	power
x	distance, stoichiometric parameter, or design variable
y	stoichiometric parameter
α	angle of attack or Bruggeman power
γ	flight angle
δ	electrode thickness or tolerance
ε	porosity or error
η	efficiency or overpotential
θ	correlation coefficient
κ	ionic conductivity
ρ	density
σ	electronic conductivity
σ^*	dimensionless conductivity
τ	tortuosity
τ^*	dimensionless diffusivity/time
φ	electric potential

List of Abbreviations

AOA:	Angle of Attack
AR:	Aspect Ratio
BFGS:	Broyden Fletcher Goldfarb Shanno (optimization method)
CG:	Conjugate Gradient
DMC:	Dimethyl Carbonate
DOD:	Depth of Discharge
DOE:	Design of Experiments
EC:	Ethylene Carbonate
EV:	Electric Vehicle(s)
FCCD:	Face Centered Composite Design
FEM:	Finite Element Method
GEO:	Geostationary Earth Orbit
GMRES:	Generalized Minimum RESidual
GSA:	Global Sensitivity Analysis
HALE:	High Altitude Long Endurance
HEV:	Hybrid Electric Vehicle(s)
KRG:	Kriging
LEO:	Low Earth Orbit
LHS:	Latin Hypercube Sampling
MAV:	Micro Air Vehicle(s)
MCMB:	Meso Carbon Micro Beads
MD:	Molecular Dynamics
MDO:	Multidisciplinary Optimization
MEMS:	Micro Electro-Mechanical Systems
MUAV:	Miniature Unmanned Aerial Vehicle(s)
NASA:	National Aeronautics and Space Administration

Ni-MH:	Nickel Metal Hydride
NMC:	Nickel-Manganese-Cobalt ($Ni_{1/3}Mn_{1/3}Co_{1/3}$)
OCP/OCV:	Open Circuit Potential/Voltage
PRESS:	Prediction Error Sum of Squares
PRS:	Polynomial Response Surface
PSO:	Particle Swarm Optimization
PVDF:	Polyvinylidene Fluoride
QP:	Quadratic Programming
RBNN:	Radial Basis Neural Network
REV:	Representative Elementary Volume
RMS:	Root Mean Square
SEI:	Solid Electrolyte Interface/Interphase
SNOPT:	Sparse Nonlinear Optimizer
SOC:	State of Charge
SQP:	Sequential Quadratic Programming
SSOR:	Symmetric Successive Over-Relaxation
UAV:	Unmanned Aerial Vehicle(s)
WAS:	Weighted Average Surrogates

Abstract

A common attribute of electric-powered aerospace vehicles and systems such as unmanned aerial vehicles, hybrid- and fully-electric aircraft, and satellites is that their performance is usually limited by the energy density of their batteries. Although lithium-ion batteries offer distinct advantages such as high voltage and low weight over other battery technologies, they are a relatively new development, and thus significant gaps in the understanding of the physical phenomena that govern battery performance remain. As a result of this limited understanding, batteries must often undergo a cumbersome design process involving many manual iterations based on rules of thumb and ad-hoc design principles.

A systematic study of the relationship between operational, geometric, morphological, and material-dependent properties and performance metrics such as energy and power density is non-trivial due to the multiphysics, multiphase, and multiscale nature of the battery system. To address these challenges, two numerical frameworks are established in this dissertation: a process for analyzing and optimizing several key design variables using surrogate modeling tools and gradient-based optimizers, and a multi-scale model that incorporates more detailed microstructural information into the computationally efficient but limited macro-homogeneous model. In the surrogate modeling process, multi-dimensional maps for the cell energy density with respect to design variables such as the particle size, ion diffusivity, and electron conductivity of the porous cathode material are created. A combined surrogate- and gradient-based approach is employed to identify optimal values for cathode thickness and porosity under various operating conditions, and quantify the uncertainty in the surrogate model. The performance of multiple cathode materials is also compared by defining dimensionless transport parameters.

The multi-scale model makes use of detailed 3-D FEM simulations conducted at the particle-level. A monodisperse system of ellipsoidal particles is used to simulate the

effective transport coefficients and interfacial reaction current density within the porous microstructure. Microscopic simulation results are shown to match well with experimental measurements, while differing significantly from homogenization approximations used in the macroscopic model. Global sensitivity analysis and surrogate modeling tools are applied to couple the two length scales and complete the multi-scale model.

Chapter 1.
Introduction

1.1 Background and Motivation

Lithium-ion batteries have attracted significant attention in recent years due to their high voltage and low weight, resulting in much higher achievable energy density than other battery technologies [1, 2, 3]. Their successful development and implementation in portable electronic devices has created further interest in their application in electric automobiles and aircraft, especially in light of increasing costs and dwindling supplies of fossil fuels. In fact, despite significant disparity in projections for oil prices and reserves, it is very likely that future oil prices will continue to increase and that production will decrease [4]. These effects are particularly important to the airline industry, which is a significant consumer of fossil fuel, with U.S. airliners alone consuming over 16.3 billion gallons of fuel (mostly Jet-A) at a cost of over $46.8 billion [5]. Furthermore, environmental concerns over the effect of carbon emissions on global climate change have also been a source of motivation for the development of lower-emissions vehicles. Estimates for global emissions of carbon dioxide due to aviation alone range from 300 to 600 million metric tons by 2025, and 500 million to 1.1 billion metric tons by 2050 [6, 7]. In order to mitigate these effects, an enormous amount of research is currently being conducted on the science and engineering of renewable energy technologies. Although many renewable energy sources exist, each has its limitations and drawbacks, as documented by the United States Department of Energy [8].

A common limitation of many energy systems is that a device such as a battery, fuel cell, or mechanical flywheel is required when simultaneous energy extraction and consumption is not feasible. This is true of propeller-driven hybrid and fully electric aircraft that use electric motors to power the main shaft, as the electricity must be stored in a battery carried aboard the vehicle. Batteries are also required in aerospace

applications where combustion-based engines such as jets and rockets are not feasible for providing the required thrust for the vehicle, or power to the subsystems. Typically, this occurs due to size (mass or volume) or environmental (e.g., lack of oxygen) constraints. It is clear, therefore, that the performance of the battery has a critical impact on the overall performance of the system.

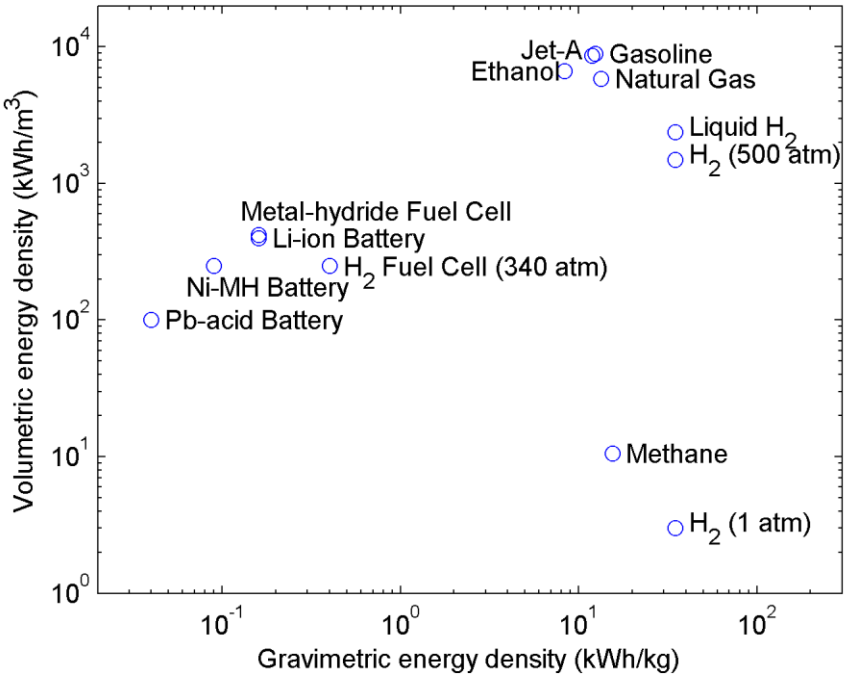

Figure 1-1: Comparison of gravimetric and volumetric energy densities of various energy storage technologies

As shown in Figure 1-1, lithium-ion batteries outperform their lead-acid and nickel-metal hydride counterparts, but still have energy densities that are two orders of magnitude lower than conventional fuels. Although part of the performance deficiency can be compensated for by the lower weight and greater efficiency of electric motors compared to combustion engines (90-100% for batteries and electric motors, 25-30% for gasoline engines, 50% for turbofan engines), it is nonetheless clear that significant improvements are needed in order for lithium-ion batteries to be considered a reliable power source in aerospace vehicles. The following sections include an overview of competing battery technologies, followed by several case studies to highlight the needs and potential of various electric-powered aerospace vehicles and systems.

1.2 Overview of Batteries

Batteries can be broadly categorized as primary and secondary. In primary batteries, the electrode materials are consumed in the cell reaction and thus cannot be recharged. Primary batteries are commonly used to power the subsystems of launch vehicles, since they offer higher energy and power density (the common alkaline primary battery has a comparable energy density to the current state of the art lithium-ion secondary battery [9]), and are only required to last a few minutes. However, the majority of aerospace applications require batteries with long cycle life. As a result, current research is heavily focused on secondary batteries, which can be recharged by applying a large voltage in the opposite direction of the battery. Even for applications in which the battery cannot be charged while in operation, it is far more cost-effective to recharge a secondary battery than to replace an entire primary battery. Therefore, this dissertation focuses exclusively on secondary batteries.

1.2.1 Past and Current Secondary Batteries

Common secondary battery technologies used in the past include lead-acid, nickel-cadmium (Ni-Cd), and nickel-metal hydride (Ni-MH). Lead-acid was the first widely used, as the propulsion system in the earliest automobiles (before the advent of the gasoline engine cars). Lead-acid batteries are still used today to help initiate the ignition of the engine, due to their low cost and the relatively lax performance requirements. Ni-Cd batteries provide superior energy density performance, but like lead-acid, they contain toxic materials. Ni-MH batteries have now replaced Ni-Cd almost completely, due to better safety and the lack of a memory effect, in which performance can be permanently reduced by charging at certain levels. They can also provide a high power density, which has made them a viable choice in early hybrid-electric vehicles.

A rough comparison of past and current secondary batteries is summarized in Table 1-1. The technologies are listed roughly in chronological order, with lead-acid being the oldest and lithium-ion and lithium-polymer being the newest. The progressive improvement in battery performance, especially in terms of the energy density, can be observed. This trend is of critical performance since, as will be demonstrated in the case

studies contained in the following sections, energy density is the most critical performance requirement in many aerospace applications.

Table 1-1: Comparison of past and current secondary battery technologies

Type	Cell Voltage	Energy Density		Power	Cycle Life
	(V)	(W-h/kg)	(W-h/L)	(W/kg)	(cycles)
Lead-acid	2.1	~35	~70	~200	~600
Ni-Cd	1.2	~35	~100	~150	~1500
Ni-MH	1.2	~75	~240	~500	~500-1000
Li-ion	3.6	~150	~400	~400	~1000
Li-polymer	3.7	~170	~300	~400	~750
Zn-Air	1.6	~150	~160	~200	400 hours

1.2.2 Lithium-Ion Batteries

From Table 1-1, it is easy to see why lithium-ion batteries have attracted significant interest. The well-known relationship between electrical power *P*, and current *I* and voltage *V*, is given by

$$P(t) = I(t)V(t) \tag{1}$$

This equation demonstrates the importance of having a high cell voltage. Since the voltage of a battery cell is determined by the difference in electric potential between the two electrodes, and since lithium is the most electropositive element, cells making use of lithium-based electrodes are able to achieve high power performance. The energy supplied by the cell is equal to the accumulated amount of power over time, and thus the high cell voltage of lithium-ion batteries allows for high energy as well:

$$E(t) = \int_{t_0}^{t} P(\tau)d\tau = \int_{t_0}^{t} I(\tau)V(\tau)d\tau \tag{2}$$

Finally, since lithium has the lowest atomic mass of all metals, lithium-ion batteries have a lower weight than other types of batteries for a fixed amount of energy or

power, making them ideal in applications where mass is a critical design constraint. A schematic diagram of a battery cell is shown in Figure 1-2.

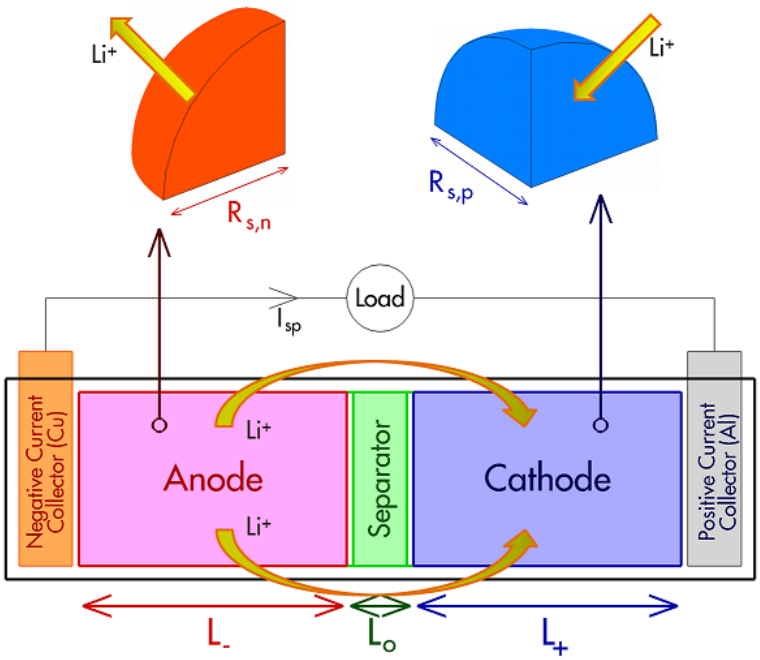

Figure 1-2: Schematic diagram of lithium-ion battery cell during discharge; during charge the process is reversed

A lithium-ion battery is a collection of individual lithium-ion cells connected in series, in parallel, or a combination of both. Single-cell batteries also exist, and are common for small-size applications such as portable electronics. A lithium-ion cell consists of a positive electrode (also called the cathode) and a negative electrode (anode) separated by a porous membrane called a separator. The electrodes are also porous, with electrolyte filling the pores and the solid consisting of active material in the form of microscopic particles, along with additives and binder materials. Each electrode is attached to a metal current collector containing the external tabs to which a load is connected. When the load is connected, a circuit involving the current collectors and electrolytes is completed, and the cell is discharged as electrons flow from the negative to the positive current collector, producing a current. To retain charge balance, positively charged lithium ions travel from the anode to the cathode via an electrolyte. The term "lithium-ion battery" typically refers to a case in which the electrolyte is a liquid containing lithium salt, while "lithium-polymer" or "lithium-ion polymer" refers to a case

where the electrolyte consists of a polymer gel material. Upon reaching the cathode, the ions are then intercalated (inserted) into the solid part of the cathode matrix. To charge the cell, an external voltage greater than the cell voltage is applied as the load, and the electrons and ions travel in the opposite direction. This is known as the "rocking chair" mechanism, as the ions travel back and forth between the electrodes as the cell is repeatedly charged and discharged. An important concept in the operation of a battery is known as the cycling rate (also known as C-rate), typically denoted in terms of a parameter C. A reference value of 1C corresponds to the rate at which the battery would be completely charged or discharged within one hour. Other C-rates are proportional to this reference value; rates less than 1C are commonly denoted as a fraction (e.g., C/2 = 2 hours to charge/discharge).

As will be discussed throughout this dissertaiton, the choice of electrode materials is an important decision in the design process. Due to the importance of cell voltage on both the power and energy of a cell, the cathode is typically a high potential transition metal oxide, while the anode is a low potential material such as a metal or graphite. The electrode materials should ideally also accommodate fast intercalation (insertion) and de-intercalation of lithium ions, have a high electron conductivity, and low weight. The electrolyte should have a high ionic conductivity and have good thermal and mechanical stability. This dissertation focuses on lithium-ion batteries with the following configuration that satisfies these criteria: lithium manganese oxide cathode ($LiMn_2O_4$) and graphite (LiC_6) anode, with an organic solvent consisting of a mixture of ethylene carbonate (EC) and dimethyl carbonate (DMC). The salt dissolved in the electrolyte is lithium hexfluorophosphate ($LiPF_6$), and the positive and negative current collectors are aluminum and copper foil, respectively. Of course, this is by no means the only possible cell configuration, and the search for materials with better voltage, capacity, and reliability characteristics has motivated significant research into new materials. Since lithium-ion battery technology is relatively new compared to lead-acid and Ni-MN, there exists considerable room for improvement, and the currently achieved performance metrics given in Table 1-1 may be exceeded with the discovery of better materials and improvements to the manufacturing process (where nanotechnology is particularly promising). To address the uncertainty in material choice, this dissertation focuses on

generalized model development and analysis that can be readily conducted on batteries of different materials, as well as seeking to obtain better understanding of the battery physics that are relevant to all systems. Furthermore, Chapter 4 contains significant analysis comparing the performance of different electrode materials.

1.2.3 Alternative and Future Batteries

Although this dissertation focuses on lithium-ion batteries, it is important to note that other less mature battery technologies have shown significant promise and may become viable candidates for next generation energy storage applications to satisfy even higher performance requirements. These include lithium-metal, lithium-air, and organic batteries.

A lithium-metal battery is a lithium-ion battery with lithium metal foil as the anode. Rather than the rocking chair mechanism in which lithium ions are inserted into opposite electrodes as the cell is charged and discharged, in a lithium-metal battery the anodic metal itself is consumed in the electrochemical reaction. Compared to the more commonly used graphite anode, lithium metal has a lower weight, lower electric potential, and higher electronic conductivity – superior performance in three important criteria discussed in Chapter 1.2.2. In fact, they have been demonstrated to provide energy density up to 230 Wh/kg [1], approximately 20% higher than the best lithium-ion batteries. Indeed, lithium metal is commonly used in applications requiring high energy without regard for cycling, such as primary lithium batteries. However, they suffer from poor cycle life due to uneven dendrite growth during charge cycles when the previously consumed lithium metal is restored to the anode. This dendrite growth leads to significant safety and reliability problems due to short-circuiting of the cell [10]. Nonetheless, there remains significant research interest in lithium-metal batteries, as recent efforts have attempted to circumvent the dendrite growth problem by replacing the liquid electrolyte with a solid-polymer material (the Li-SPE battery) [11, 12].

The lithium-air battery has been recently proposed as a candidate for achieving energy densities up to 1000 Wh/kg, more than five times that of a typical lithium-ion battery [13]. In a lithium-air battery, the anode consists of lithium metal and the cathode

is formed by the oxidation of lithium metal by oxygen, by exposing the metal to air. The previously successful zinc-air battery showed good stability in aqueous and alkaline electrolytes without significant corrosion, and has thus been used in small, high energy density applications with low cycling rates, such as hearing aids. Despite their high energy density, low cost, and long shelf life, lithium-air batteries have exhibited poor power output and a limited operating temperature range. In spite of significant recent research efforts to address these limitations [14], lithium-air batteries remain far from viable in large-scale applications.

Finally, organic lithium batteries have been proposed not because of superior performance, but rather the recyclability and renewability of the electrode materials, thus reducing their carbon footprint. If effective processes can be developed, production costs could be lowered such that the electrodes could be synthesized from cheap, readily available materials. Although capacity and energy density are expected to be high, power rate is expected to be limited [2]. This will likely make organic lithium batteries unsuitable for automotive applications, but they may still be useful in certain aerospace applications such as long-endurance flyers or satellites where power is of lesser concern.

1.3 Batteries in Aerospace Systems: Case Studies

Recent advancements in materials science and the development of micro-electro-mechanical systems (MEMS) have aroused the interest of engineers for the substitution of conventional combustion engines with battery-powered electric systems. Significant headway has been achieved in partially replacing the internal combustion engine with batteries in automobiles, such as in hybrid- and electric vehicles, but achievements in aerospace applications have been more limited. In this section, several case studies of hybrid or electric vehicles are presented to highlight important challenges related to the power and energy requirements in aerospace systems, as well as document the potential performance enhancements that can be enabled by improvements to battery technology. These case studies are also intended to demonstrate the shortcomings of current battery systems, thus motivating the need for the research featured in this dissertation.

In much of this dissertation, a strong focus is placed on energy density, which as

discussed previously is the most critical performance metric in many applications. However, it is important to be aware of the other objectives that must be satisfied in battery design. Table 1-2 provides an overview of the requirements of various battery-powered systems.

Table 1-2: Comparison of battery requirements for various engineering systems

Requirement	Electronics	Automotive	Manned Aircraft	UAV/MAV	Satellites and Spacecraft
Power	Not important except in highly specialized devices	Critically important	Critically important for takeoff and climb	Less important for hand-launched vehicles	Varies considerably depending on mission
Weight	Less important than volume	Important for EV, less important for HEV	Critically important	Critically important	Critically important
Volume	Depends on device, but typically the most critical limiting performance metric	Moderately important; typically weight is limiting factor for Li-ion	Moderately important; typically weight is limiting factor for Li-ion	Less important than weight due to flexible cell geometry	Typically less important than weight, but can be critically important
Cycle Life	Depends on device, but less important in designs with removable battery	Critically important	Not important except for very frequent flying	Depends on mission, but typically not important	Critically important for satellites; unimportant for planetary missions
Sensitivity to Environment	Not important except in highly specialized devices (e.g. implantable medical devices)	Moderate temperature range capability required	Low temperature capability critical due to altitude	Depending on operating altitude, can range from negligible to similar to manned aircraft	Critically important due to extreme temperatures and radiation; requires thermal regulation
Scaling and System Integration	Not important; single-cell may be sufficient	Critically important	Critically important	Depends on size, but scaling is typically not a limitation	Depends on system, but often critically important

Safety	Important, but not as critical as in automobiles and aircraft	Critically important due to high power rates	Critically important high power at takeoff; motor failure could be catastrophic	Desired but not critically important	Critically important in manned spacecraft; unimportant in satellites

It is immediately clear that in spite of some common objectives, battery systems in aerospace applications must be designed differently from those in automobiles or electronics, as certain irrelevant considerations in one application must be enforced as strict constraints in another. One example is weight, which is of less importance than volume in hybrid electric vehicles (HEV) that make efficient use of regenerative braking. On the other hand, the design of multifunctional materials with batteries embedded in the structure has reduced the importance of volume in applications such as UAV/MAV [15], while, as is demonstrated in Chapter 1.3.2, weight is of much greater importance. In yet other applications, such as satellites and spacecraft, both weight and volume are of critical importance, while power might not be. The complicated design process that results from needing to consider tradeoffs between multiple objectives, including those listed in Table 1-2 and those discussed in the following case studies, reinforce the need to better understand the physical processes that occur within a battery cell, and the interplay between performance criteria and design variables. This is especially true of new systems and vehicles that make greater use of electrical systems by using them to supplant less efficient, less robust mechanical systems.

Notable examples of this trend include the Chevrolet Volt, a plug-in hybrid electric automobile, and the Boeing 787 Dreamliner, a mid-size long-range jet airliner. The 787 makes much greater usage of electrical systems than previous airliners, with generators producing electricity from the main engines and auxiliary power unit [16]. The reduced number of mechanical components improves overall efficiency and substantially reduces fuel emissions, especially during idling and taxiing, but places a much higher demand on the batteries and generators to supply sufficient electricity. Therefore, the overall cost reductions and other benefits of greater electrification are highly sensitive to the relative performance and efficiency of the electric and conventional systems. In the case of the 787, the greater electricity demand necessitates larger batteries, electric

motors, and generators, which all increase the total weight of the aircraft and thus reduce the overall fuel efficiency. Therefore, high-energy, high-power, low-weight batteries are of critical importance to achieving Boeing's goals of long-term reductions in operating cost and fuel burn for the next generation of airliners. However, the recently discovered safety concerns regarding leaking in the 787's battery packs [17] have also highlighted the importance of satisfying multiple objectives simultaneously.

1.3.1 Solar-Powered Aircraft

Solar power has become a leading candidate as part of a broad portfolio of green technologies that do not consume fossil fuels. In recent years, with the gradual improvement in photovoltaic cell efficiency and manufacturing capabilities [18], the extension of solar power to aircraft has been proposed and realized in a few applications. Perhaps the best-known examples in this category are NASA's Pathfinder family of experimental unmanned aircraft, which includes the original Pathfinder along with the more recent models Pathfinder Plus, Centurion, and Helios. Like most solar-powered aircraft, they consist of a very long, high aspect ratio wing (AR = 31 for Helios), with a large array of photovoltaic cells on the upper surface. These provide power to electric motors that power propellers to generate thrust. The wings necessarily have a large surface area and high aspect ratio due to limitations in incident light and cell efficiency. The Pathfinders fly at very high altitudes: maximum altitude ranges from 65,000 feet for Pathfinder to over 96,000 feet for Helios, although optimal efficiency occurs at lower altitudes. For their high service ceiling and high efficiency, they are part of a class of vehicles known as high altitude long endurance (HALE) flyers. NASA's stated long-term goal is to sustain long-term flight for atmospheric research purposes (as "atmospheric satellites"); therefore, nighttime flight will require battery power. For instance, a 24 hour non-stop flight with the Helios prototype requires approximately 1×10^5 MJ of energy [19]. Current battery technology is insufficient for meeting this goal, so a second configuration for Helios, which includes an additional hydrogen-air fuel cell system, has been designed for maximizing endurance.

A more recent project is the Solar Impulse, with the stated mission goal of

crossing the Atlantic Ocean in a single continuous flight, as well as making a trip around the world in segments lasting a few days at a time. Powered by 11,628 photovoltaic cells providing power to 4 10-horsepower electric motors during day and 400 kg of lithium-polymer batteries at night, the aircraft is manned by a single pilot and has successfully completed a 26-hour flight that involved 9 hours of night-time flying. Battery performance is the most critical limiting factor to the aircraft performance, as the lithium-polymer batteries that power the aircraft account for 25% of the total design mass of 1600 kg. In fact, in a 2010 interview that has since been removed from their website, the Solar Impulse team confirmed that battery energy density was indeed the most critical limitation to vehicle performance:

> *Question: What area still limits the plane's performance?*
> *Answer: It is above all, the energy density of the batteries. Their stocking capacity is still limited and their influence has a great bearing on the total mass of the airplane. By doubling their storage capacity, it would be possible to allow a second person on board and therefore carry out longer flights.*

A critical reason why the stated trans-Atlantic goal has not been achieved in spite of the aircraft's demonstrated capability of flying for a continuous 24-hour period is the physiological limitations on a single pilot. This is an excellent example to highlight the potential benefits of improving the energy density of current lithium-ion batteries.

1.3.2 Unmanned Aerial Vehicles (UAV)

The past decade has also seen a rapid incline in the capabilities and functionality of unmanned aerial vehicles (UAV). Since the first operationally significant Air Force UAV program, known as the Lightning Bug, came into inception, UAVs have primarily found applications in tactical reconnaissance. The turning point in the perception of these systems came in 1980s, when Israel deployed UAVs in the Bekaa valley to counter Syrian forces. After the Bekaa valley campaign, US purchased unmanned vehicles, such as 'Pioneer' and initiated a development program of its own that led to systems such as

RQ-1 predator (commonly known as “Predator A”). Subsequently, in 1998, RQ-4 (Global Hawk) accomplished its first flight, and has been flown for more than 7000 hours since. Small UAVs, such as Raven and Pointer, have also been developed and are man-portable, low-altitude, short-range systems that assist in reconnaissance and targeting. In addition to military uses, RPAs (Remote Piloted Aircraft) and UAVs have potential applications such as homeland defense (for example, in border-control and anti-drug warfare), civilian search and rescue, point-to-point cargo delivery, weather data collection, environmental monitoring and emergency management. Rapid recent advancements in aerospace and materials engineering have facilitated new RPA and UAV designs that make use of lighter and smaller sensor and weapon payloads (and hence a high capability per unit weight). Advances in UAV design also enable the operation of such systems in environments that are hazardous for humans, such as those contaminated by chemical, biological or radioactive agents.

The term UAV encompasses a broad range of flyers of various configurations and sizes. Two notable subclasses of smaller flyers include miniature unmanned aerial vehicles (MUAV) and micro-air vehicles (MAV). Although unmanned flyers typically have greater endurance than manned systems due to the lack of payload, it is well known that energy and power generation become increasingly difficult as the size of the vehicle is decreased due to scaling differences between aerodynamics and weights [20]. In this section, a case study analyzing the performance gains for a MUAV that can be achieved with higher energy batteries is presented. Although no formal definition for MUAV exists, they are typically used for low-altitude reconnaissance, surveillance and target acquisition, and have a wingspan of a few feet (1-2 meters) and weight of a 2-3 kg. Examples include the Desert Hawk (Lockheed Martin), Aladin (EMT), and RQ-11 Raven (AeroVironment) models, the latter of which is the subject of this case study.

The RQ-11 Raven is used by the U.S. Army, Air Force, Marine Corps, and Special Operations Command, in addition to military forces in 8 other countries. It can be controlled either remotely from a ground station, or autonomously using GPS waypoint navigation. The specifications for the vehicle are provided in Table 1-3, based on the data sheet available at the AeroVironment website [21].

Table 1-3: Specifications for RQ-11 Raven (MUAV)

Wingspan	4.25 feet
Weight	4.2 lbs
Endurance	80 minutes
Range	6.2 miles (limited by communications)
Cruise speed	60 mph

The total energy requirement for this MUAV can be estimated by knowledge of the cruise speed, endurance time, and required thrust:

$$E_{req} = \frac{TV_{cruise}t_{end}}{\eta_{prop}\eta_{motor}\eta_{batt}} \tag{3}$$

The required thrust can be determined by estimating the lift-to-drag ratio. This case study assumes $L/D = 9$, a value typical of small aircraft [22]. The thrust can then be calculated by assuming that under cruise conditions, thrust must equal drag and lift must equal weight:

$$T = D = \frac{L}{L/D} = \frac{W}{L/D} \tag{4}$$

Based on Eq. (4) and the specifications in Table 1-3, the required thrust is about 2.08 N. Assuming propeller, electric motor and battery efficiencies of 85%, 95% and 90%, respectively, the total energy requirement calculated using Eq. (3) is about 3.68×10^5 J, or 102 Wh. For a typical battery energy density of 150 Wh/kg, the battery mass is 0.68 kg, or 36% of the total vehicle mass. By increasing battery energy density from 150 to 250 Wh/kg, the battery mass can be reduced by 0.27 kg, allowing the installation of a second payload device. Alternatively, for the same mass, the higher energy density battery would provide enough additional energy to extend the endurance by 53 minutes.

1.3.3 Satellites and Spacecraft

A third class of systems in which batteries play a critical role on the overall system level performance are satellites and spacecraft. Mass is a critical limitation in spacecraft design, with launch costs often estimated on a per-kilogram basis. Spacecraft

are one area where the superior energy density of lithium-ion batteries have not made much impact, as energy density is superseded by an even more important performance objective: cycle life. For this reason, Ni-H_2 batteries are still commonly used, as they have proven to be highly reliable (the original Hubble Telescope batteries lasted 19 years). Nonetheless, recent studies have shown that lithium-ion batteries hold great promise in this regard, as up to 30,000 cycles can be achieved for a battery cycled to 40% depth of discharge (DOD) [23]. For satellites in low earth orbit (LEO) such as the International Space Station, which experience 35 minutes of eclipse per 90 minute orbit cycle, this corresponds to about a 5 year lifetime, although more cycles can be expected if the depth of discharge can be reduced. Meanwhile, geostationary earth orbit (GEO) missions require 10+ year lifetimes due to the impossibility of periodic battery replacement. In this section, two case studies based on cost are considered: the Hubble Telescope in LEO, and a Boeing 702 communications satellite in GEO.

According to data from the Hubble Telescope website [24], the satellite orbits at an altitude of 569 km at a 28.5 degree inclination, meaning it experiences 36 minutes of eclipse per 97 minute orbit. It is powered by 6 Ni-H_2 batteries totalling 340 kg, which accounts for about 3% of its total launch mass of 11,110 kg. Since lithium-ion batteries typically offer about double the mass-specific energy density of their Ni-H_2 counterparts, launch costs alone could be reduced by $1.7 million, based on the commonly quoted $10,000/kg launch cost for LEO satellites [25]. Boeing 702 is a large communications satellite that operates at GEO, used by DirecTV, XM Radio, and others. GEO has an altitude of 35,786 km, ensuring that the satellite orbits at the same rate as Earth. This is useful for communications purposes, as the satellite remains in the same position relative to the Earth. Unlike satellites in LEO, those in GEO only experience eclipse during two 45-day periods per year, with a maximum duration of 72 minutes. However, launch costs are even greater, with estimates of $36,000/kg in 2002 and $20,000/kg in 2010 [26]. Although no data are available for total available energy, it is known that the Boeing 702 satellites use Ni-H_2 batteries rated at 328 Ah [27]. Assuming the same capacity-mass relationship as in the Hubble Telescope (450 Ah, 340 kg), converting to lithium-ion technology could reduce the satellite mass by 217 kg. At the 2010 specific launch cost to GEO, this corresponds to a savings of $4.3 million. If the projections of 60,000 cycles at

25% DOD at LEO conditions by Fellner *et al.* [23] can be validated for prismatic batteries, lithium-ion technology can substantially reduce launch costs and enable addition of more complex satellite subsystems.

Another important challenge facing lithium-ion batteries in space applications is their relatively narrow operating temperature range compared to older nickel-based chemistries, which have all demonstrated a wide operating temperature range from at least -20 to 50°C [28]. While considerable ongoing research has shown promising results towards achieving a comparable operating range for lithium-ion batteries, a systematic method of analysis and optimization is necessary to properly incorporate them into the design the satellites and spacecraft [29, 30].

1.3.4 Hybrid Electric Aircraft Propulsion System

This final case study presents a more detailed model for analyzing the performance of a hybrid-electric generation aviation aircraft. Specifically, the flight dynamics, engine, and battery of a hybrid version of a Cessna 172 are modeled by coupling it to a controller. Although several all-electric aircraft such as the PC-Aero Elektra One, Pipistrel Taurus Electro G2, and ElectraFlyer-C have been developed, their range is limited by the low energy density of the battery. In this study, a hybrid aircraft propulsion system is proposed, which couples a downsized version of the Cessna 172's piston engine with a lithium-ion battery pack as the secondary energy storage system. In addition to reducing carbon emissions and fuel costs, the electric component of a hybrid system also does not lose power as altitude increases as air-breathing systems do. The additional cost of introducing a battery pack can also be mitigated if it is added to an existing aircraft configuration, as a $10,000 pack would only inrcrease the cost of a Cessna 172 by about 3%. This is a much lower percentage of the total vehicle cost than comparable hybrid-electric automobiles, and thus the hybridization of existing aircraft models holds significant prommise. However, the additional battery mass also results in reduced payload and fuel capacity, which could limit the benefits of hybridization. The purpose of this case study is to quantify these tradeoffs in greater detail using physics-based models, in order to tradeoffs of costs and benefits of hybridizing a general aviation

aircraft.

Three individual physical models for the aircraft, battery, and engine are included in the analysis. Additionally, a controller model regulating the inputs and outputs of these individual models is developed. Figure 1-3 contains a diagram showing how these models are linked. Note that a single global controller is used to control all individual models, which to not communicate with one another directly.

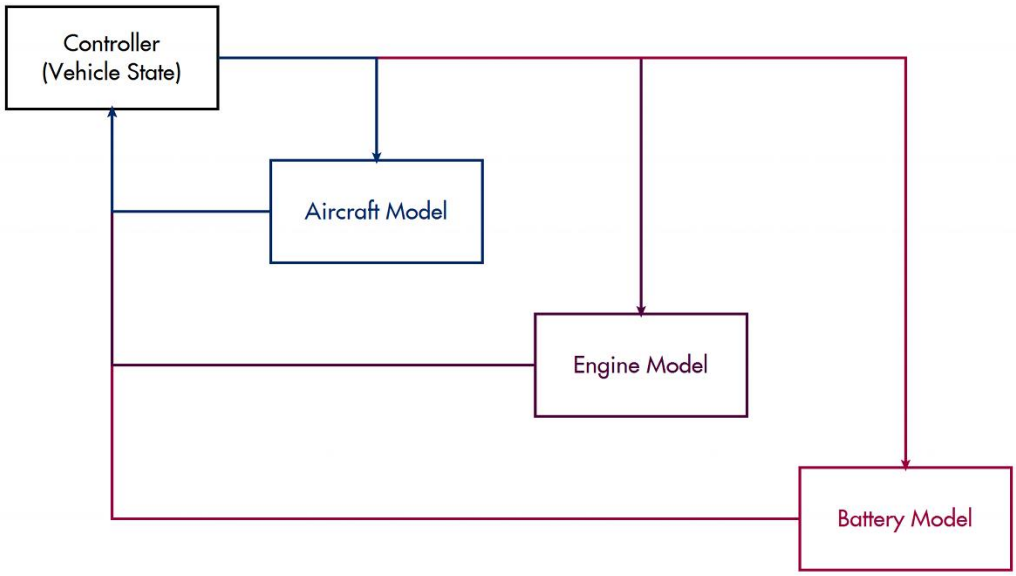

Figure 1-3: Schematic of model hierarchy

The baseline aircraft model is the Cessna 172 Skyhawk SP, a four-seat, single-engine, fixed-wing aircraft that has been in production since 1955. According to the Cessna company website [31], more of this model have been build than any other aircraft. Since the goal of this study is not to design a hybrid aircraft, but rather to analyze its propulsion system and performance, no modifications are made to the aerodynamic properties of the aircraft. Some of the key parameters are listed in Table 1-4. The inputs to the aircraft model are the velocity, altitude, and vehicle mass (which gradually decreases as fuel is consumed). Based on these inputs, the model is able to calculate the corresponding forces acting on the aircraft (lift, weight, drag, and thrust), from which the required power from the engine can in turn be computed. Since the aircraft is not modified, existing aerodynamic data can be used in the aircraft model.

Table 1-4: Properties of Cessna 172 SP

Wing area (m^2)	16.2
Empty weight (kg)	781
Max take-off weight (kg)	1157
Max fuel weight (kg/gal)	144 / 56
Propeller diameter	1.92
Max engine power (hp)	180
Cruise speed (km/hr)	233 (75% power)
Stall speed (km/hr)	99

Figure 1-4 contains wind tunnel testing data for a Cessna 172 over a wide range of angles of attack (AOA), and shows that the maximum lift-to-drag ratio occurs at an angle of attack of 5 degrees. This is the design cruise condition for optimal fuel economy and maximum range. A detailed explanation of the equations of motion for maximizing range can be found in Appendix A.

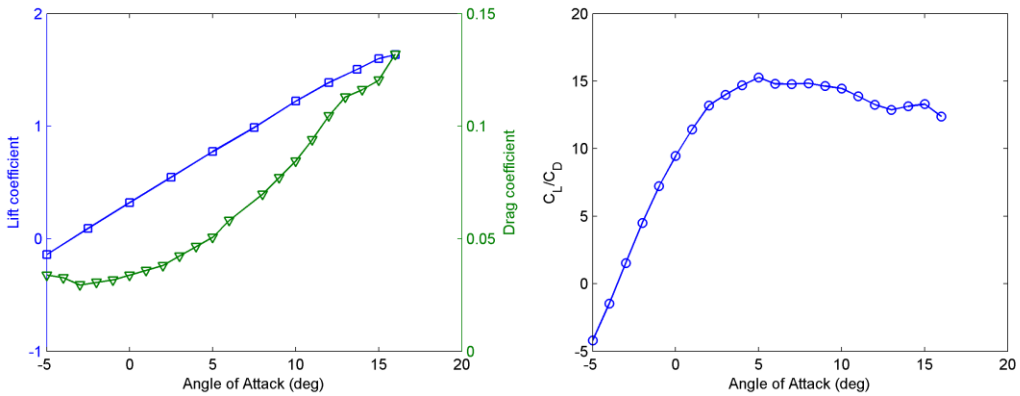

Figure 1-4: Lift, drag, and L/D as a function of AOA for Cessna 172

The battery pack in this case serves two purposes: to provide additional power to the aicraft during periods of high power demand (i.e., takeoff), and to provide an efficient alternative to the engine while cruising. In this study, an equivalent-circuit (internal resistance) model is applied to $LiNi_{1/3}Mn_{1/3}Co_{1/3}$ batteries, a type of lithium-ion battery commonly known as NMC. Relevant parameters for the battery pack are listed in Table 1-5.

Table 1-5: Battery parameters at 22°C

Capacity	56 A-hr
Max Power	151 kW
Min Voltage	374 V
Max Voltage	412 V
SOC Limit	0.2
Mass	180 kg
Internal Resistance	0.28 Ω
Discharging Efficiency	0.97

The battery pack is assumed to be thermally regulated with a constant temperature of 22°C, and includes 60 pouches with 100 layers in each pouch. The total power, voltage, and current of the battery pack can be calculated from the corresponding values for a representative cell, multiplied by the number of pouches and layers:

$$W_{pack} = W_{cell} \cdot n_{pouch} \cdot n_{layer} \tag{5}$$

$$V_{pack} = V_{cell} \cdot n_{pouch} \tag{6}$$

$$I_{pack} = I_{cell} \cdot n_{layer} \tag{7}$$

The rate of change in the state of charge (SOC) is calculated from the open circuit voltage, internal resistance, and battery capacity:

$$\frac{dSOC}{dt} = -\frac{V_{OC} - \sqrt{V_{OC}^2 - 4P_{batt}R_{\text{int}}}}{2C_{batt}R_{\text{int}}} \tag{8}$$

This quantity is outputted from the battery model to the controller, while the inputs are the current SOC and the required power. In this study, the SOC is tracked separately by the controller, so there is no need to integrate Eq. (8) within the battery model itself. In this analysis, no electric motor is considered. Instead, the motor efficiency is lumped together with the battery efficiency, and subsequent analysis assumes that the battery power is delivered directly to the vehicle with the lumped

efficiency. The mass of the motor is also lumped together with the battery pack.

Most of the models of the Cessna 172 use one of the 360-class engines produced by Lycoming Engines. This study models the O-360-A model, a four-cylinder direct-drive air-cooled piston engine that consumes 100LL, a type of aviation gasoline with similar properties to unleaded automobile gasoline. In order to model the power delivered for various throttle settings and engine speeds, as well as the fuel consumption at all engine operating points, torque and fuel maps need to be created. Since torque and fuel map data are not available for the O-360-A, available data for a Corvette engine are used, and scaled according to available Lycoming engine specifications. Although the accuracy of the simulated aircraft performance is reduced due to this simplification, the scope of this study is to establish a simulation framework and demonstrate the value of such modeling to systems-level design. The model can always be improved by substituting the data used in this study with those corresponding to the actual engine, with minimal modification to the framework. Specifications for the Lycoming Engine are as follows: the maximum power delivered is 180 horsepower at 2700 rpm. The model scales the torque map of the Corvette engine linearly based on this calibration point. Additionally, there are two calibration points used for the fuel consumption map: at an altitude of 8000 feet, the Cessna-172 with the Lycoming O-360-A engine has a range of 580 nautical miles (nmi) and endurance of 4.8 hours, with the engine operating at 80% power. At 10000 feet, the range and endurance are 687 nmi and 6.6 hours respectively, at 60% power. The fuel consumption map is scaled to fit through these two points via linear interpolation. For verification, the fuel consumption rate at zero-throttle is a small positive value at all engine speeds, ensuring physically realistic scenarios at all operating conditions.

An additional consideration in the modeling of an aircraft engine is the effect of altitude on the engine performance. This is due to the change in ambient air properties at high altitudes. In this study, Eq. (9) from McCormick [22] is used to model the power delivered, for maximum sea level power $P_{0,max}$ = 180 hp. The efficiency η and throttle setting σ are accounted for in the torque map, and the air density ρ is found by linear interpolation using standard atmosphere tables:

$$P = P_{0,\max}\eta\sigma\left(\frac{\rho}{\rho_0}\right)^{0.6} \tag{9}$$

As implemented in the current study, the engine model's inputs are the engine speed and throttle setting, and the outputs are the delivered power and fuel consumption.

In the aircraft model, there are several targets that the controller must consider. In addition to vehicle velocity, there are constraints on the altitude, flight angle, and angle of attack. Therefore, attempts at implementing an existing controller, such as MATLAB's proportional-integral-derivative (PID) controller have been unsuccessful. Instead, a "target-based" controller is used in this study, which adjusts the engine throttle setting and battery power load based on the current vehicle state at each time step. The "target" vehicle state is the set of conditions that the vehicle would like to operate at based on cruise efficiency and the current vehicle state. At each time step, the throttle setting and battery load are adjusted based on the difference between the target and current states. The target conditions are calculated using the equations given in Appendix A.

Table 1-6: Vehicle state variables and constraints

State	Symbol	Units	Constraint
Distance	x	m	-
Altitude	h	m	$0 \le h \le 4115$
Velocity	V	m/s	$0 \le v \le 63.03$
Angle of Attack	α	degrees	$-5 \le \alpha \le 16$
Flight Angle	γ	degrees	-
Vehicle Mass	w	kg	$w \le 1111$
Engine Power	P_e	W	$P_e \le 134226$
Battery Power	P_b	W	$P_b \le 60000$
Engine Speed	s	rpm	$600 \le s \le 6000$
Throttle Setting	Th	percent	$0 \le th \le 100$
Fuel	f	gallons	$f \le 3$
State of Charge	SOC	-	$0.20 \le \text{SOC} \le 0.99$

Table 1-6 lists the vehicle state variables tracked by the controller model, as well as their constraints. Note that no explicit constraints are placed on the flight path angle,

allowing for potential instability in the controller if the angles become too large. Also note that no distance constraint is considered, since the range would be determined by the remaining vehicle states. The equations for adjusting the battery load and throttle setting at each time step are given in the following equations:

$$P_{b,target} = \frac{P_{b,\max}}{\eta_b}\left(\frac{SOC - SOC_{\min}}{SOC_{\max} - SOC_{\min}}\right)\left(\frac{V_{cruise} - V}{V_{cruise}}\right) \tag{10}$$

$$P_{b,i+1} = P_{b,i} + \left(\Delta P_b\right)_{\max}\left(\frac{P_{b,target} - P_{b,i}}{P_{b,target}}\right) \tag{11}$$

$$Th_{target} = Th_i - 0.5556\gamma - 100\left(\frac{V - V^*}{V^*}\right) \tag{12}$$

$$Th_{i+1} = Th_i + \left(\Delta Th\right)_{\max}\left(\frac{Th_{target} - Th_i}{Th_{target}}\right) \tag{13}$$

The term V^* in Eq. (12) is the target cruise velocity based on quasi-steady analysis. The remaining vehicle states are then updated using a forward Euler scheme,

$$y_{i+1} = y_i + \left(\frac{\partial y}{\partial t}\right)_i dt \tag{14}$$

where the state variable *y* can be any of the ones listed in Table 1-6.

As shown in Figure 1-3, the individual aircraft, engine, and battery models do not interact with one another. Instead, each one supplies a set of outputs to the controller, which are then used to update the vehicle state. The controller then assigns new inputs to each of the individual models based on newly calculated target states. Superficially, the lack of communication between individual models seems like a disadvantage, as it does not maximize the use of globally available information about the vehicle state. However, there are important advantages to setting up the controller this way. For example, the vehicle state can be easily tracked at each time step, and that simple control schemes can be readily implemented and modified for each of the individual models. Another advantage is that each of the individual models can be easily substituted when more sophisticated models are available, such as torque and fuel maps based on actual data for the Lycoming engine, or more detailed battery models that account for physical phenomena not captured by the equivalent circuit model.

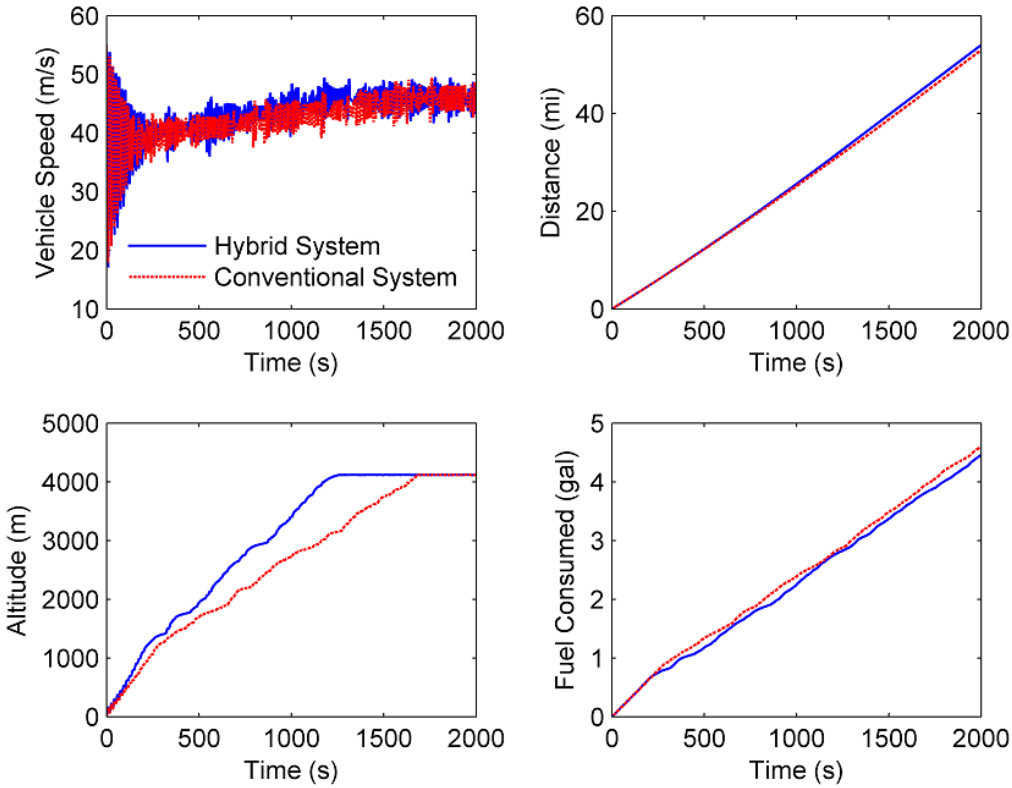

Figure 1-5: Time history plots of the vehicle state for hybrid and conventional systems

In order to compare the relative performance of the hybrid and conventional systems, simulations of 20,000 time steps of 0.1 seconds are run for each system. Both simulations use the same initial takeoff condition, where the altitude is specified to be at sea level and the initial velocity is equal tot the takeoff velocity of a Cessna 172. Time history plots of important state variables for the two systems are shown in Figure 1-5. The extra power provided by the battery greatly improves the rate of climb, and the hybrid vehicle is able to reach the cruise altitude much more quickly. However, note that the fuel consumption and distance traveled show little difference between the two systems. To investigate why the two systems show such similar performance characteristics despite the additional power provided by the battery pack, it is useful to examine the engine and battery power for the hybrid system. The time histories of the two power sources are shown in Figure 1-6.

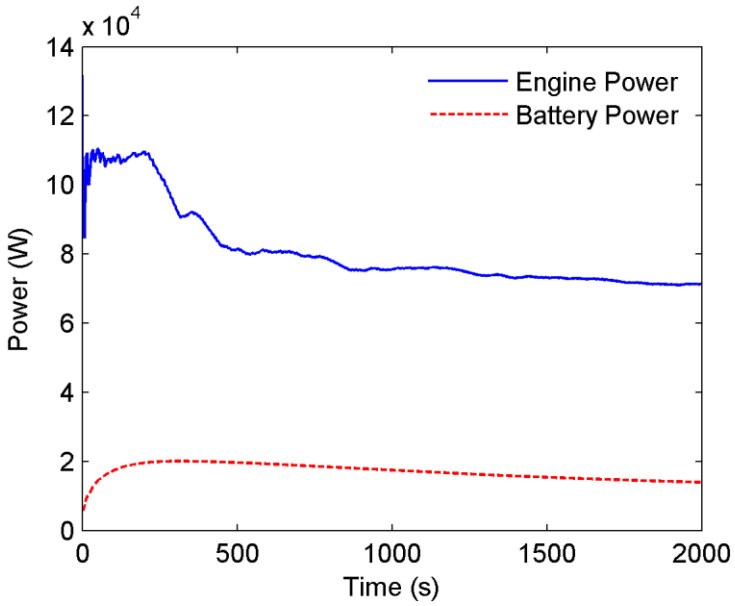

Figure 1-6: Time-averaged engine and battery power for hybrid system

Note that the engine power greatly exceeds the battery power. Since the battery power comprises only a small proportion of the total power delivered, its effect on overall performance is limited. The final SOC after 2000 seconds is 0.63, for an average C-rate of about 0.65C. This suggests that most of the battery mass is essentially acting as deadweight, thus requiring even more power from the engine than for the conventional system. Increasing the maximum allowed power would make greater use of the hybrid propulation system. The velocity plot in Figure 1-5 also shows that the controller selected for this study is a critical factor in limiting the efficiency of the hybrid system due to the inability to achieve steady-state conditions without large fluctuations.

Although significant difficulties with the controller has given results that do not indicate substantial differences in aircraft performance between a hybrid and a conventional propulsion system, the modeling framework established has been structured in a way that allows easy replacement with enhanced controller or component models. Another reason the hybrid system is not found to offer significant performance gains is the limited energy density offered by the batteries. Although LiNMC batteries can achieve higher energy density than most other battery technologies, they are still far below the levels attainable with conventional fuels such as 100LL. Nonetheless, Boeing has proposed a hybrid-electric airplane called Subsonic Ultra Green Aircraft Research (SUGAR) Volt, for which preliminary studies have identified a threshold energy density

value of 750 Wh/kg that would meet NASA's N+3 goal of 70% reduction in fuel burn [32].

1.3.5 Summary of Case Studies

Four specific classes of aerospace vehicles are presented in this chapter: solar-powered aircraft which include both the unmanned HALE and manner Solar Impulse; unmanned aerial vehicles (UAV) which includes the subclasses MUAV and MAV; satellites/spacecraft in various orbits such as LEO and GEO; and a much more detailed model of the propulsion system of a hybrid-electric general aviation aircraft based on the Cessna 172. In all cases, the energy density of the batteries is found to be a critical limitation to the performance of the vehicle. In the Pathfinder family of HALE flyers, the stated goal of achieving 24 hour continuous flight with the Helios is not yet realizable because of insufficient battery energy density. Instead, Helios relies on hydrogen fuel cells to achieve continuous flight, which as shown in Figure 1-1 have energy density values over 400 Wh/kg, compared to 150-200 Wh/kg for state of the art lithium-ion batteries. The design of new lithium-ion cells with a comparable energy density would allow Helios to be powered by batteries instead of fuel cells, thus eliminating the need for hydrogen fuel. Similarly, although Solar Impulse has demonstrated the ability to fly continuously during the nighttime, the aircraft's endurance is still limited by the need for the pilot to rest. A doubling of the battery energy density from 200 to 400 Wh/kg would allow a second person on board, allowing the aicraft to fly for much longer periods as the two pilots alternate.

In contrast to Solar Impulse and Helios, the RQ-11 Raven, an example of a miniature unmanned aerial vehicle (MUAV), is able to meet its stated objectives, which is to provide 80 minutes of endurance at a cruise speed of 60 mph while being controlled from a portable ground station. In this class of vehicles, range is not of critical concern, since the radio transmission range is a greater limitation to range than the battery. However, as demonstrated in Chapter 1.3.2, improvements to energy density can still offer important advantages, such as extending the endurance by 53 minutes with an increase in energy density from 150 to 250 Wh/kg, or the capability to carry a second

payload device in addition to the on-board camera. Satellites and spacecraft are another class of vehicles whose performance is not limited by the energy density of lithium-ion batteries. In fact, they typically carry the older nickel metal hydride (NiMH) battery technology due to its superior cycle life. Therefore, the design goal of lithium-ion batteries for space applications is not the increase in energy density, but rather the extension of cycle life and calendar life. Low earth orbit (GEO) satellites require much greater cycle life due to the frequency of eclipses during which its solar photovoltaic cells are inactive, while geostationary earth orbit (GEO) satellites do not experience as many eclipses, but also cannot be serviced due to their high orbit altitude, and thus require batteries that can last its entire mission life of 10+ years. In addition, battery systems designed for space missions must meet additional environmental constraints, and appropriate design features such as radiation protection must be properly considered.

In the final case study, the results are somewhat inconclusive due to the lack of a suitable controller model, resulting in unreliable results for a simulated flight mission. The inclusion of the battery in the hybrid configuration resulted in a greater rate of climb, thus allowing the vehicle to reach its cruising altitude about 500 seconds earlier. However, the decrease in the amount of fuel consumed by the combustion engine is very small, and does not demonstrate any major benefits of the hybrid configuration over the conventional configuration. As seen in Figure 1-6, this is due to the limited use of the battery by the controller, as the time-averaged power and total energy provided by the battery is several times less than that provided by the engine. Nonetheles, it is important to point out that the design of a battery with higher capacity would allow the controller to draw a greater proportion of the total system power from the battery while maintaining the same SOC, and thus improve the performance of the hybrid configuration.

1.4 Objectives and Outline of the Dissertation

The examples in Chapter 1.3 have been presented to demonstrate some of the potential gains that can be achieved with high energy batteries. However, the energy density of presently available battery systems is limited to about 200 Wh/kg, about half of what is required in several classes of vehicles. This is in large part due to a limited

understanding of battery physics and limited use of systematic modeling and optimization techniques in the battery design process. Therefore, there exists a need to apply efficient numerical methods to gain a better understanding of the relevant physical phenomena occuring within battery cells, in order to design and build higher energy and higher power batteries that can satisfy the vehicle performance requirements. This is compounded by the capabilities of existing battery models, which, as will be discussed in Chapters 2.2 and 2.5, tend to be either overly simplified or computationally expensive. Specifically, the macroscopic cell models commonly used to study battery performance contain simplifications based on homogenization for important properties such as transport coefficients and interfacial reaction rates, which actually depend on the electrode microstructure. Therefore, the following objectives must be satisfied to to realize the potential gains in these vehicles:

i. Develop a numerical framework based on surrogate-based analysis tools to systematically analyze the effect of multiple design variables such as operation, morphology parameters, and material properties on battery performance;

ii. Apply dimensional analysis and optimization techniques to better understand the underlying physics that govern and limit battery performance;

iii. Develop microscopic and multi-scale models that can accurately incorporate the effects of microstructure in simulating battery performance, to rectify limitations in the presently available homogeneous models.

The research presented in this dissertation is motivated by the aerospace vehicles and systems discussed in Chapter 1.3. It is logical, then, to place emphasis on the implications of this research on the benefits that may be realized in the design of those systems. The term “battery performance” most frequently refers to energy density, as it is a critical performance objective in all of the case studies shown in this chapter. However, some of the results must also be interpreted in the context of other relevant design objectives such as power density in high-power applications like hybrid-electric general aviation aircraft, and minimizing degradation for long cycle life applications like LEO

satellites. Where appropriate, the research presented in this dissertation seeks to address these other objectives in addition to energy density.

In Chapter 2, the numerical tools used to obtain results in the following chapters of the dissertaiton are summarized. This includes the macroscopic homogeneous battery cell model, surrogate modeling framework, gradient-based optimization schemes, and microscopic modeling techniques. Governing equations and a comprehensive literature review for these methods is included, as well as important details about the numerical implementation of the tools. Where appropriate, examples are provided to highlight the capabilities of the methods, and to compare alternative approaches.

In Chapter 3, surrogate-based analysis is applied to the macroscopic cell model, to study the effect of cycling rate, particle size, diffusivity, and conductivity on the cell energy density. The process of repeatedly refining the design space by introducing additional cell simulations is documented, along with shifts in surrogate model fidelity within the design space. A strategy for partitioning the design space based on global sensitivity analysis is presented, and the benefits of using multiple surrogates in different regions of the design space, compared to a single global surrogate, are discussed. The chapter concludes with an analysis of the tradeoff between energy and power.

The surrogate-base analysis is continued in Chapter 4, with the introduction of additional design variables. In this chapter, optimization is performed using two different strategies: by applying the gradient-based optimizer directly to the cell model, and by applying the same optimizer to the surrogate model. The relative accuracy and computational cost of the two methods are compared. This chapter also examines the relative performance of several different electrode materials, in the context of dimensionless diffusivity and conductivity parameters obtained using dimensional analysis.

Chapter 5 focuses on the modeling of material properties, namely the effective transport coefficients and interfacial electrochemical reaction current density, at the microscopic level using clusters of electrode particles. Results for effective transport rates calculated using graph analysis algorithms are also presented. Comparisons between the detailed 3-D FEM simulation results with the homogenization approximations used in the macroscopic models are made, and the microscopic modeling results are incorporated

into a multi-scale model, which uses surrogate modeling to couple the macroscopic and microscopic length scales. The multi-scale modeling section includes a survey of the literature and discussion of different multi-scale modeling strategies, followed by a discussion of numerical issues such as definition of the deriatives of state variables within the multi-scale model, and robustness of the coupling function. The chapter concludes with a comparison of the internal state of the battery modeled using multi-scale and homogeneous methods, and a discussion of the implications of the results on battery design.

Chapter 2.
Methodology

2.1 Introduction

This chapter provides an overview of the numerical tools used in this research. These include the physical models for the battery cells and their components, the surrogate-based modeling and analysis framework and toolbox, and the gradient-based optimization methods. The numerical tools appear in this chapter in roughly the order they are utilized within the dissertation: the macroscopic battery cell model and surrogate modeling framework are presented first, followed by the gradient-based optimization methods, and finally microscopic models.

2.2 Macroscopic Battery Cell Model

Since the advent of lithium-ion batteries, various models have been developed to describe and simulate their behavior and performance. These include single-particle models [33, 34, 35], equivalent circuit models [36, 37], capacity-fade models [38], microscopic models [39, 40], 3-D models [41], and reformulated homogeneous models [42, 43]. In order to apply surrogate- and gradient-based analysis techniques to investigate the relationship between design variables related to the operation, manufacturing process, and configuration of battery cells and their performance, the macroscopic battery cell model must possess the following properties:

i. Simulating the system-level behavior of the entire cell, and not just individual components;

ii. Sufficient detail into the physical processes within the cell to capture the

effect of all specified input/design variables and provide modeling solutions with a reasonable level of accuracy;

iii. And computational efficiency that allows for a large number of simulations to be conducted for design space sampling and optimization.

Each of the class models listed above fails in at least one of these three criteria. 3-D models are too computationally expensive to be feasible for problems in which hundreds or thousands of simulations need to be conducted, while microscopic models cannot be used to calculate the overall cell voltage or capacity. The remaining models are unable to accurately the effects of varying certain parameters due to excessive simplification of the model physics.

Fortunately, a macroscopic homogeneous pseudo-2D model based on porous electrode and concentration theory is available. Developed by Doyle, Fuller, and Newman [44, 45], it models lithium ion diffusion and electron conduction in both the solid and liquid phases of the porous electrode matrix, which is assumed to be homogeneous. This model has been validated against experimental data [46], and is sufficiently detailed for analysis and optimization of a large number of variables. Furthermore, it retains good computational efficiency, with the available Fortran implementation (also called the `dualfoil` program) typically requiring tens of seconds to compute a single constant-current discharge cycle on a single-CPU computer. It has thus become a commonly used method for studying cell performance [47, 48]. However, numerical issues have been observed to cause convergence difficulties for certain cases with low diffusivity and a low discharge cutoff; for these cases alternative numerical platforms such as the COMSOL Multiphysics implementation of the model are preferred. The following is a summary of this model, which is used for all cell simulations in Chapters 3 and 4. In this dissertation, this model is sometimes referred to as the macro-homogeneous model, or simply the cell model.

The model is called a pseudo-2D because it models lithium ion and electric potential distributions along an axial dimension across the thickness of the cell, while accounting for the effect of particle size by applying the superposition principle to introduce a radial pseudo-dimension at each computational node to compute the rate of

ion diffusion within a spherical pseudo-particle. Along the axial dimension, the electric potential distribution in the solid and liquid phases is modeled using steady transport equations:

$$\nabla \cdot \left(\sigma^{\text{eff}} \nabla \varphi_1 \right) - J = 0 \tag{15}$$

$$\nabla \cdot \left(\kappa^{\text{eff}} \nabla \varphi_2 \right) + \nabla \cdot \left(\kappa_D \nabla \left(\ln c_2 \right) \right) + J = 0 \tag{16}$$

The axial dimension also models transient lithium ion diffusion in the liquid phase:

$$\varepsilon_2 \frac{\partial c_2}{\partial t} = \nabla \cdot \left(D_2^{\text{eff}} \nabla c_2 \right) + \frac{1 - t_+^0}{F} \nabla \cdot \mathbf{i}_2 - \frac{\mathbf{i}_2 \cdot \nabla t_+^0}{F} \tag{17}$$

At the interfaces between electrodes and current collectors, fixed boundary conditions are applied:

$$\nabla \varphi_1 = \frac{-I_{dis}}{\sigma} \tag{18}$$

$$\sigma \nabla \varphi_2 = 0 \tag{19}$$

$$\nabla c_2 = 0 \tag{20}$$

Note that all three equations in the axial dimension involve an effective transport coefficient, which are calculated from bulk properties using the Bruggeman equation to account for electrode porosity ε:

$$\frac{\sigma^{eff}}{\sigma^{bulk}} = \frac{\kappa^{eff}}{\kappa^{bulk}} = \frac{D_2^{eff}}{D_2^{bulk}} = \varepsilon^{\alpha} \tag{21}$$

The empirical value of α = 1.5 is most commonly used, although microscopic modeling results discussed in Chapter 5 suggest a different value. As mentioned, the second radial dimension models the time-dependent ion concentration distribution within spherical particles:

$$\frac{\partial c_1}{\partial t} = \frac{1}{r^2} \frac{\partial}{\partial r} \left(D_s r^2 \frac{\partial c_1}{\partial r} \right) \tag{22}$$

Boundary conditions for the temporal and spatial dimensions are applied at the center and surface of the sphere, respectively:

$$\left.\frac{\partial c_1}{\partial t}\right|_{r=0} = 0 \tag{23}$$

$$-D_s \left.\frac{\partial c_1}{\partial r}\right|_{r=R_{s,j}} = \frac{i_{n,j}}{F} \tag{24}$$

Note that the solid and liquid phases are coupled via the Butler-Volmer equation which models electrochemical kinetics at the interface between the phases based on the local surface overpotential η:

$$J = \begin{cases} a_{s,p} i_{n,p} & \text{in the positive electrode} \\ 0 & \text{in the separator} \\ a_{s,n} i_{n,n} & \text{in the negative electrode} \end{cases} \tag{25}$$

$$i_{n,j} = i_{0,j}\left[\exp\left(\frac{\alpha_{a,j} F}{RT}\eta_j\right) - \exp\left(-\frac{\alpha_{c,j} F}{RT}\eta_j\right)\right] \tag{26}$$

$$a_{s,j} = \frac{3\varepsilon_{1,j}}{r_{s,j}} \tag{27}$$

$$\eta_j = \varphi_1 - \varphi_2 - U_{OCP} \tag{28}$$

The exponential terms in Eq. (26) make the entire system of equations very sensitive to the overpotential, which in turn is sensitive to the open circuit potential U_{OCP}. The open circuit potential is defined as the difference in potential between the two electrodes when no load is applied, and is a function of the SOC. Each electrode material has a unique open circuit potential function; in models such as this one, a curve fit of experimental measurements is typically used. For $LiMn_2O_4$, the most frequently used cathode material in this dissertation, the following equation based on empirical measurements is used:

$$\begin{aligned} U_{OCP} &= 4.06 + 0.0678\tanh\left(-21.9y + 12.8\right) \\ &-0.106\left[\left(1.00 - y\right)^{-0.380} - 1.58\right] - 0.045e^{-71.69y^8} + 0.01e^{-200(y-0.19)} \end{aligned} \tag{29}$$

With the inclusion of these equations, the system is fully coupled and can be solved for the four state variables (c_1, c_2, φ_1, φ_2). Note that although in this dissertation a single constant-current discharge cycle is simulated to calculate the energy and power

performance of the cell, the model is also capable of simulating arbitrary charge and discharge cycles.

2.3 Surrogate Modeling Framework

The concept of using systematic numerical tools in engineering analysis and design is quite common, as the notion of design variables influencing system performance can be found in numerous engineering systems. Nonetheless, many engineering system and modeling designs are still conducted as open loop, feed-forward processes involving many manual iterations in what is effectively a trial-and-error process. In order to make proper use of computational resources in addressing engineering challenges, a proper mathematical framework capable of simultaneously evaluating multiple variables and objectives is necessary. A good candidate for accomplishing this is the surrogate-based analysis framework, also known as surrogate modeling or metamodeling, which seeks to construct an approximation of the objective function (a "surrogate" for the true function) based on a finite number of discrete sample points obtained from experiments or numerical simulations. In this sense, it is similar to a set of curve-fitting tools, but has the following key advantages:

i. Surrogate models do not require calculation of the local sensitivity of each design variable, making them useful for optimizing problems in which the objective function is not smooth;

ii. Information collected from various sources and by different tools can be combined;

iii. Optimization of multiple objectives and criteria can be performed by quantifying tradeoffs between multiple design points;

iv. Tasks can be easily performed in parallel;

v. Noise intrinsic to numerical and experimental data can be effectively filtered via smoothing parameters;

vi. And the surrogate models provide an approximation for functions that can be easily used to bridge disparate length or time scales in multi-scale problems.

Each of these advantages is demonstrated in the following chapters of this dissertation. This section provides a summary of the underlying concepts and principles of the surrogate modeling framework with emphasis on the most commonly applied components in this dissertation, as well as the implementation details of the MATLAB toolbox developed within the research group. Surrogate modeling has been used in a variety of engineering problems, including estimation of intercalation-induced stress in lithium-ion battery electrode particles [40], tuning adjustable parameters in a cavitation model for cryogenic fluids [49], shape optimization of diffuser vanes in an engine pump [50], and aerostructural optimization of long-range aircraft [51]. Other examples of this framework can be found in the following references: [47, 52, 53, 54, 55, 56, 57].

2.3.1 Concepts

A schematic diagram highlighting the key steps in the surrogate modeling process is shown in Figure 2-1.

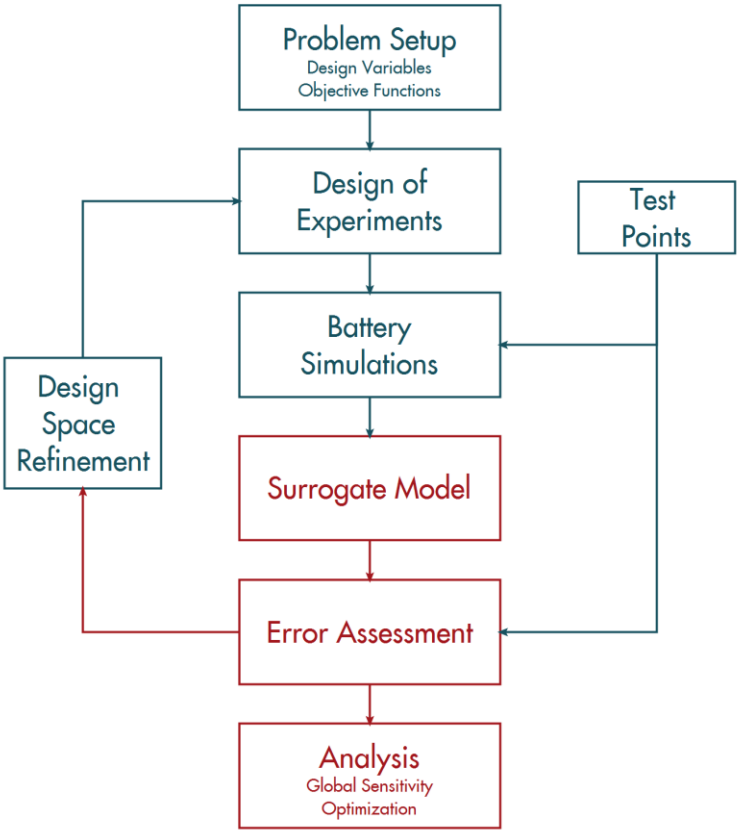

Figure 2-1: Surrogate modeling process; steps shown in red are part of the surrogates toolbox while those in blue are problem-specific

The process begins with constructing a set of numerical experiments to sample the design or parameter space, known as the design of experiments. In most problems the nature of the objective function is not known beforehand, so it may be simplest to use random sampling to avoid systematic bias. However, since computational resources typically limit the number of samples that may be selected, a more efficient strategy is desired. One improvement over pure random sampling is Latin Hypercube sampling (LHS), which provides a random sampling but ensures a stratified sample within the full range of each dimension of the sample space [58].

In many cases it is also desirable to have a deterministic sample that can be reproduced. Furthermore, LHS provides a limited sampling of the extrema of the design space, which may be of special interest. One deterministic sampling method considered in this study is the two-level face-centered composite design (FCCD), which includes the face-center points and vertices of the design hypercube [59]. Other deterministic

sampling methods also exist, such as multi-level factorial and Halton sequencing [60]. However, these are not used in this dissertation as a combination of LHS and FCCD was generally found to be adequate.

A set of simulations are then conducted based on the design of experiments, and a surrogate function $\hat{y}$ is used to approximate the true function y for a vector of design variables **x**. The next section discusses the different approaches for accomplishing this.

2.3.2 Classes of Surrogate Models

In general, different types of surrogate models should be attempted and compared if possible, since the best method is problem-dependent (and, as will be seen, region-dependent within a single design space) and cannot be predicted beforehand. In this dissertation, four classes of surrogate models are considered: polynomial response surface (PRS), kriging (KRG), radial-basis neural network (RBNN), and weighted averaging of multiple surrogates (WAS). Other classes of surrogate models such as support vector regression and splines exist, but are not considered here.

A polynomial response surface approximates the objective function as a linear combination of polynomial basis functions:

$$\hat{y}(\mathbf{x}) = \sum_i b_i f_i(\mathbf{x}) \tag{30}$$

The basis functions include both first-order and cross terms, and the coefficient vector $\boldsymbol{b}$ is selected using a least-squares regression routine. Kriging models add a set of basis functions [61] that act as a systematic departure $Z(\mathbf{x})$:

$$\hat{y}(\mathbf{x}) = \sum_i b_i f_i(\mathbf{x}) + Z(\mathbf{x}) \tag{31}$$

The systematic departure components are assumed to be correlated as a function of distance between the locations under consideration, and the maximum likelihood estimation is used to determine the parameter estimates [62]. In this study a variety of correlation functions are considered: Gaussian, linear, exponential, cubic, spline, and spherical. A detailed formulation of these correlation functions has been summarized by Lophaven *et al.* [63].

A radial-basis neural network model approximates the objective function as a linear combination of radial basis functions, also known as neurons [50]. In this dissertation, the following form containing Gaussian radial basis functions is considered:

$$\hat{y}(\mathbf{x}) = \sum_{i=1}^{N_{RBF}} w_i a_i(\mathbf{x}) \tag{32}$$

$$a_i(\mathbf{x}) = e^{-(\|\mathbf{s}_i - \mathbf{x}\|\beta)^2} \tag{33}$$

Note that the basis functions depend directly on the distance between the point **x** and the neurons. The number of neurons and associated weights are determined by satisfying the user defined error "goal" on the mean squared error in approximation. Figure 2-2 contains a graphical example of how different types of surrogate models fit an approximate function based on the discrete sample points shown. Note that the KRG and RBNN models fit the training data points exactly while interpolating between them, whereas the PRS does not.

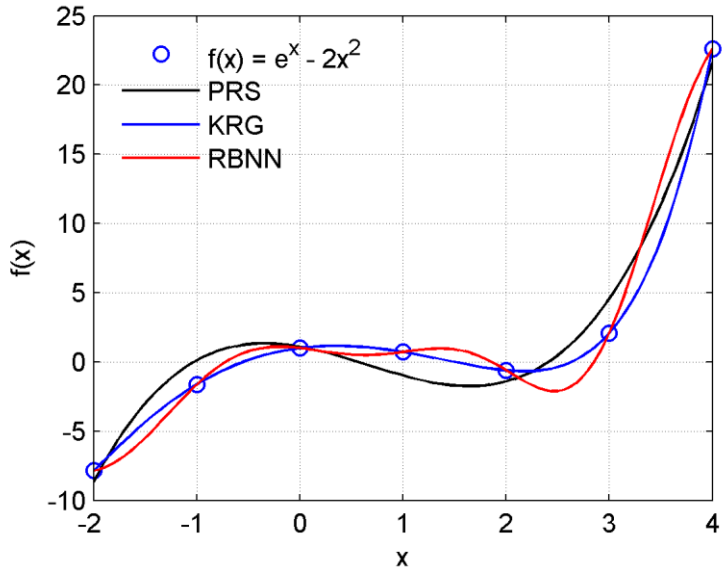

Figure 2-2: Surrogate models for an analytical function

Finally, weighted averaging of multiple individual surrogate models can reduce uncertainties in selecting the best model based on limited validation criteria. Various weighting strategies are possible; in this dissertation a method based on the prediction error sum of squares (PRESS) value (defined in the following section) of individual surrogates is used. Further details of weighting strategies for multiple surrogates have

been summarized by Goel *et al.* [64].

2.3.3 Cross-Validation

Despite the advantages listed above, an important challenge is the quantification of uncertainty in the surrogate model. Since a design of experiments consists of a limited number of samples, the surrogate model introduces an additional layer of error, known as the prediction error, to the uncertainty intrinsic to the simulation of the physical system (such as the macroscopic battery cell model). Error estimation is also important as a method for comparing the accuracy of multiple surrogate models. Various procedures for comparing error measures have been documented by Goel et al. [65]; this dissertation focuses on the following:

i. Coefficient of determination (including the adjusted version) for polynomial regression models;

ii. Prediction errors at independently sampled test points;

iii. Prediction error sum of squares (PRESS).

Both standard and adjusted coefficients of determination are considered in this dissertation:

$$R^2 = 1 - \frac{\sum_{i=1}^{N_s} \left(y(\mathbf{x}_i) - \hat{y}(\mathbf{x}_i) \right)^2}{\sum_{i=1}^{N_s} \left(y(\mathbf{x}_i) - \bar{y} \right)^2} \tag{34}$$

$$R^2_{adj} = 1 - \frac{\sum_{i=1}^{N_s} \left(y(\mathbf{x}_i) - \hat{y}(\mathbf{x}_i) \right)^2}{\sum_{i=1}^{N_s} \left(y(\mathbf{x}_i) - \bar{y} \right)^2} \frac{(N_s - 1)}{(N_s - N_\beta)} \tag{35}$$

Note that both measures are always less than or equal to 1, and that the equality condition is met when the approximate surrogate function $\hat{y}$ matches the true function y exactly for all sampling points $\mathbf{x}$. Therefore, a value closer to 1 indicates a more accurate surrogate model. Also note that the difference between the two measures is that the adjusted coefficient of determination includes a dependency on the number of sampling

points N_s and degrees of freedom N_β.

Like the coefficients of determination, PRESS is computed directly from the training data does not require independent test points. It is defined as the sum of the "leave-one-out" prediction errors at all data points, defined as the prediction error at a particular point using the surrogate model with the same input parameters constructed from all other data points. In a more general formulation allowing an arbitrary number of data points to be left out at a time, this parameter is known as the generalized mean square error (GMSE). Mathematically, PRESS is defined as follows:

$$PRESS = \sqrt{\frac{1}{N_s}\sum_{i=1}^{N_s}\left(y_i - \hat{y}_i^{(-i)}\right)^2} \tag{36}$$

Note that when N_s is sufficiently large, it is possible to calculate approximate PRESS values by leaving out more than a single point at a time. More details about these "leave-k-out" approaches can be found in work published by Meckesheimer *et al.* [66]. No formulas are included here for calculating prediction errors using independent test points, although the mean, RMS, and maximum errors are the most commonly used quantities in this dissertation.

Each of these methods has its limitations: coefficients of determination are not useful for interpolation schemes such as kriging which match the training data from the design of experiments exactly, validation using test points requires the use of a second independent design of experiments in addition to the computational cost of conducting the corresponding simulations, and PRESS can be unwieldy and cumbersome to compute as the number of iterations scales with the square of the number of data points in the sample. Therefore, a comprehensive error assessment should consider multiple error criteria.

2.3.4 Global Sensitivity Analysis with Surrogate Models

Since the analytic function approximating the true objective function that can be evaluated much more quickly, surrogate models enable analysis techniques that require a large number of function evaluations. One example used in this dissertation is global sensitivity analysis, which quantifies the relative impact that each design variable has on

the objective function as it is varied. This is useful for identifying variables that little effect, as the problem dimensionality can be reduced by removing those variables from consideration. The following section summarizes Sobol's method [67], which is employed in this framework.

The function *f* as defined by the surrogate model can be decomposed as a linear combination of functions of subspaces of the design space, also known as additive functions. A generalized form of this decomposition can be written:

$$f(\mathbf{x}) = f_0 + \sum_i f_i(x_i) + \sum_{i<j} f_{ij}(x_i, x_j) + \cdots + f_{1\ldots N_v}(x_1, \cdots, x_{N_v}) \tag{37}$$

The total variance *V(f)*, defined as the expected value of the square of the summation of all non-zero order additive functions, can also be expressed as a sum of partial variances of individual variables and combinations of variables:

$$V(f) = \sum_{i=1}^{N_v} V_i + \sum_{i<j} V_{ij} + \cdots + V_{1\ldots N_v} \tag{38}$$

The partial variances are in turn defined in terms of the expected value of the additive functions:

$$\begin{aligned} V_i &= V\left(E\left[f \mid x_i\right]\right) \\ V_{ij} &= V\left(E\left[f \mid x_i, x_j\right]\right) - V_i - V_j \\ &\cdots \end{aligned} \tag{39}$$

The expected value of the additive functions and their variances can be expressed as integrals of the additive functions:

$$E\left[f \mid x_i\right]_i = \int_0^1 f_i dx_i \tag{40}$$

$$V\left(E\left[f \mid x_i\right]_i\right) = \int_0^1 f_i^2 dx_i \tag{41}$$

These integrals are estimated using numerical approximations. In this dissertation, three-point and five-point Gauss quadrature schemes are used, as well as a Monte Carlo method. The partial variances can then we used to compute main and total sensitivity indices:

$$S_{Mi} = \frac{V_i}{V(f)} \tag{42}$$

$$S_{Ti} = S_{Mi} + \frac{\sum_{j,j\neq i} V_{ij} + \cdots}{V(f)} \tag{43}$$

Note that the difference between the main and total sensitivity indices is that the total index includes cross-terms between multiple variables; that is, the index for the i^{th} variable includes all variance terms involving i. In comparison, the main index for the i^{th} variable includes all variance terms involving only i. The relative importance of the design variables can be observed by comparing either their partial variances (main sensitivity indices) or their total variances (total sensitivity indices). The difference between the main and total sensitivity indices for each variable also gives an indication of the degree of interaction between variables. Note that Sobol's method is just one of many available methods for quantifying the global sensitivity of a model output to multiple inputs. For example, Saltelli *et al.* have provided a comprehensive discussion of GSA theory and propose an alternative method based on the Fourier amplitude sensitivity test (FAST) [68].

2.3.5 Pareto Front

The optimization of a single continuous objective function can be performed by simply searching the design space for the minimum or maximum value of the objective, using any established optimization method (see Section 2.4 for examples). However, many engineering problems involve multiple competing objectives, such as maximizing both energy and power in lithium-ion batteries. In such cases, there exists not a single optimal design, but many designs in which one objective can be improved at the cost of another [69]. A useful way to analyze these tradeoffs is to construct a Pareto front, i.e., the set of Pareto-optimal or Pareto-efficient solutions. The criterion for Pareto-optimality is based on the concept of dominated designs, per the following definition: A design or solution is said to be dominated if and only if the following conditions are satisfied:

i. There exists another solution that is no worse in any objective;

ii. And the other solution is better in at least one objective.

Thus, the Pareto front represents the set of all solutions that represent the optimum for some relative weighting of the objectives. Inspection of the Pareto front can be useful for revealing the existence of favorable tradeoffs between competing objectives, making it another useful tool in the design process. In the surrogate modeling framework, the Pareto front is constructed by training a separate surrogate model for each objective and then using them as data generators to populate the multidimensional objective space.

2.4 Gradient-Based Optimization

In a mathematical context, optimization is the process of identifying the minimum (optimum) value of a function. In a general optimization problem, the goal is to find the minimum of the objective function $f(x)$ within the bounds x_{lower} and x_{upper} of n design variables, subject to m inequality constraints $g(x)$ and k equality constraints $x(h)$:

$$\text{minimize} \quad f(x) \qquad f:\Re^n$$

$$\text{subject to} \quad \begin{cases} x_{lower} \le x \le x_{upper} & \\ g(x) \ge 0 & g:\Re^n \to \Re^m \\ h(x) = 0 & h:\Re^n \to \Re^k \end{cases} \tag{44}$$

Maximization problems (e.g., energy density) can be converted to minimization problems by defining the objective function as the negative or inverse of the quantity being optimized. Optimization algorithms can generally be classified into two groups: gradient-based and gradient-free. Most methods operate by iteratively improving the objective function by searching the design space, until some convergence criterion is satisfied. For gradient-based methods, the most common convergence criterion is the satisfaction of the KKT conditions [70], although other choices exist. Although gradient-free methods such as Nelder-Mead (NM) simplex [71] and Particle Swarm Optimization (PSO) [72] have proven to be effective at locating optima for various well-defined problems, this dissertation focuses on gradient-based methods which are more efficient and capable of handling a larger number of design variables for smooth objective functions [73]. Specifically, the well-established sequential quadratic programming (SQP) is used as the primary gradient-based optimizer [74].

This dissertation makes use of two different implementations of the SQP optimizer. When applied to a function supplied by a surrogate model operating in the MATLAB environment, the native MATLAB function `fmincon` is used. However, in other cases the optimizer is applied directly to the `dualfoil` program, which as explained in Chapter 2.2 is an executable written in the Fortran programming language. In this case, the Sparse Nonlinear OPTimizer (SNOPT) is selected, as it interfaces well with external executable programs [75]. In both cases, the SQP algorithm is a quasi-Newton line-search method that determines the search direction by solving a series of quadratic programming (QP) subproblems. Each QP subproblem minimizes a quadratic approximation of the Lagrangian function corresponding to the optimization problem, subjected to linearized constraints. For the k^{th} QP problem, the Lagrangian function corresponding to the objective function f_k and gradient vector g_k is treated as the objective function to be minimized:

$$\begin{aligned} &\text{minimize} && L(x) = f_k + g_k^T (x - x_k) + \tfrac{1}{2}(x - x_k)^T H_k (x - x_k) \\ &\text{subject to} && c_k + J_k (x - x_k) = 0 \end{aligned} \tag{45}$$

The second-order (Hessian) derivative matrix H_k is pproximated using the BFGS method [76]. An important challenge to gradient-based optimization methods, including SQP, is the computation of the derivatives (gradients) of the objective function. Although first-order finite-difference approximations are simple to program and easy to understand, they are subject to cancellation errors due to the subtraction operator in the formula that limit their numerical precision. To address this limitation, the complex-step derivative approximation [77] is used instead:

$$f'(x) = \frac{\text{Im}[f(x + ih)]}{h} + O(h^2) \tag{46}$$

Note that unlike classical finite-difference formulas, Eq. (46) does not involve any subtraction operation and thus retains full numerical precision for arbitrarily small step size h. It is also important to note that the complex-step method requires complex arithmetic. The optimization methodology presented here has been applied to optimize cathode and anode material properties for a single lithium ion cell [78].

2.5 Microscopic Models

Although the macroscopic cell model is computationally efficient and satisfies the requirements listed in Chapter 2.2, it does suffer some limitations. In particular, note that the effective transport coefficients and interfacial reaction current density modeled in Eqs. (21) and (27), respectively, are based on homogeneous approximations that do not account for electrode microstructure. It has been well documented that the oversimplified treatment of these "closure terms" often does not accurately describe the effects of porosity and tortuosity on these quantities [57, 79, 80], and thus the utility of the surrogate modeling and optimization processes are limited. This problem can be addressed by conducting detailed 3-D simulations of the entire cell, but the computational cost of such an approach would be impractical for simultaneously analyzing and optimizing a large number of design variables. Therefore, as discussed in Chapter 1.4, a multi-scale modeling approach, in which microscopic simulations conducted on sample microstructures consisting of clusters of particles are used to model the closure terms, is taken in this dissertation. This section documents the concepts and numerical tools used to establish these models, which include the governing equations for the effective transport and reaction rate governing equations, the generation of sample microstructures, the voxel meshing algorithm, and finally the graph analysis algorithms based on graph and network theory. The microscopic simulations are conducted using COMSOL Multiphysics, a commercial FEM software package. COMSOL contains a variety of numerical solvers and preconditioners, which are discussed in greater detail in Chapter 5. The voxel meshing and graph analysis are performed in MATLAB, and as shown in Figure 2-3 the entire microscopic modeling process makes extensive use of the MATLAB-COMSOL interface, allowing a large number of REV to be simulated without manual iterations.

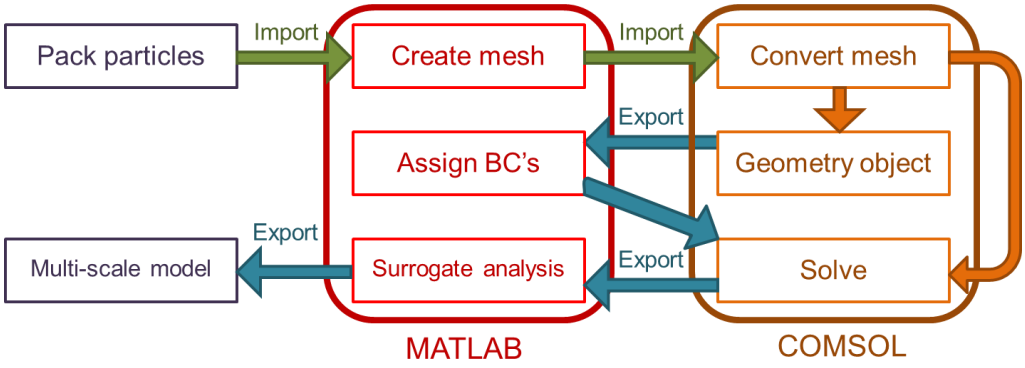

Figure 2-3: Numerical implementation of automated microscopic modeling procedure

2.5.1 Concepts and Governing Equations: Effective Transport Coefficients

The microscopic simulations are conducted on representative elementary volumes (REV). Each REV is generated by randomly packing a specified number of spherical or ellipsoidal particles into a cubic control volume using a molecular dynamics (MD) algorithm. The resulting geometry consists of two phases: active solid defined as the volume occupied by the particles, and liquid electrolyte defined as the void space in the remainder of the cubic volume. Further details of the REV generation and meshing can be found in the following sections. For the effective transport simulations, the state variable being solved is the ion concentration c, within the liquid phase. The effective transport coefficients are computed by solving the steady-state diffusion equation for a 3-D REV:

$$\nabla \cdot \left(D^{bulk} \nabla \cdot c \right) = 0 \tag{47}$$

Since the bulk transport coefficient D^{bulk} is independent of the concentration c, Eq. (47) reduces to the Laplace equation:

$$\nabla^2 c = 0 \tag{48}$$

Dirichlet (fixed concentration) boundary conditions are applied to opposite ends of the REV. For simplicity, the values 0 and 1 are used for an REV of dimension L:

$$c_{z=0} = 0 \tag{49}$$

$$c_{z=L} = 1 \tag{50}$$

Since no electrochemical reactions or ion transport are assumed to occur at the interface between the two phases, the interface is modeled as an insulated wall. From the computed steady-state solution, the effective diffusivity and conductivity can be obtained by integrating the concentration gradient over an arbitrary cross-section in the normal direction (for $L = 1$):

$$D^* \equiv \frac{\sigma^{eff}}{\sigma^{bulk}} = \frac{\kappa^{eff}}{\kappa^{bulk}} = \frac{D_2^{eff}}{D_2^{bulk}} = \int_A \nabla c dA\Big|_z \tag{51}$$

2.5.2 Concepts and Governing Equations: Interfacial Reaction Rate

The interfacial reaction simulations involve simultaneously solving a set of four transport equations, two in each of the solid and liquid phases. Steady-state equations for ion concentration c and electric potential φ in each phase are solved:

$$\nabla \cdot \left(\sigma \nabla \varphi_1 \right) = 0 \tag{52}$$

$$\nabla \cdot \left(-\kappa \nabla \varphi_2 - \frac{\kappa RT}{F} \left(1 + \frac{\partial \ln f}{\partial \ln c_2} \right) \left(1 - t_+^0 \right) \nabla \ln c_2 \right) = 0 \tag{53}$$

$$\nabla \cdot \left(-D_s \nabla c_1 \right) = 0 \tag{54}$$

$$\nabla \cdot \left(-D_2 \nabla c_2 \right) + \frac{\vec{i}_2 \cdot \nabla t_+^0}{F} = 0 \tag{55}$$

As in the effective transport simulations, Dirichlet boundary conditions are applied at opposite ends of the REV for all four state equations. In this dissertation, the selection of boundary conditions is based on either the instantaneous, localized state variables from a macroscopic cell simulation, or on a design of experiments. The boundary conditions make use of both the concentration $c_{1,i}$ and its directional gradient in

the axial direction:

$$c_{1,z=0} = c_{1,i} - \frac{L}{2}\frac{\partial c_{1,i}}{\partial x} \tag{56}$$

$$c_{1,z=1} = c_{1,i} + \frac{L}{2}\frac{\partial c_{1,i}}{\partial x} \tag{57}$$

Analogous forms of the boundary conditions are used for the other state variables c_2, φ_1, and φ_2. Note that aside from the liquid-phase concentration and potential, the state equations are not coupled. Also note that the electrochemical reaction kinetics at the solid-liquid interface is not modeled explicitly. In fact, the solid-liquid interface is modeled, as in the effective transport simulations, as an insulated wall. Instead, a localized version of the Butler-Volmer equation on the steady-state solution:

$$j_{flux} = k c_e^{0.5}\left(c_t - c_s\right)^{0.5} c_s^{0.5}\mathrm{BV}\left(\eta\right) \tag{58}$$

$$\mathrm{BV}\left(\eta\right) = \left[\exp\left(\frac{F}{2RT}\eta\right) - \exp\left(-\frac{F}{2RT}\eta\right)\right] \tag{59}$$

$$\eta = \varphi_1 - \varphi_2 - U_{OCP} \tag{60}$$

$$J = \frac{F}{V}\int_{A_s}\left(D_s \nabla c_s\right)\cdot \vec{n} dA = \frac{F}{V}\sum_{\Delta A} j_{flux}\Delta A \tag{61}$$

Therefore, these simulations are an example of quasi-steady analysis. Since the electrochemical reactions occur much faster than the ion diffusion process within solid particles, the quasi-steady formulation can significantly reduce the computational expense of conducting a large number of simulations. A comparison of Eqs. (58)-(61) to (25)-(28) in the macroscopic model shows that homogenization is removed in the microscopic model by applying the Butler-Volmer kinetics computation to the locally refined ion and potential distribution, and integrating over the true interfacial surface area. Figure 2-4 summarizes the governing equations in the two phases for a sample REV, along with a visualization of the interface.

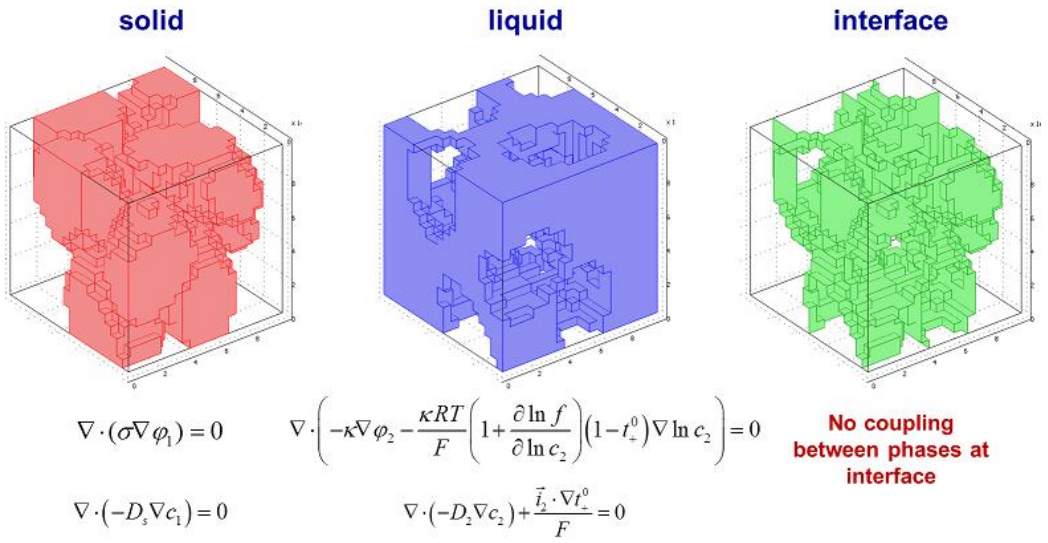

Figure 2-4: Summary of governing equations in solid and liquid phases for sample geometry (Case 1180)

2.5.3 Microstructure Generation using Molecular Dynamics Simulations

As previously mentioned, sample microstructures are generated based on the random packing of ellipsoidal particles. In the cases demonstrated in this dissertation, a fixed number of monodisperse prolate ellipsoidal particles with AR = 2 are packed using a molecular dynamics algorithm developed by Donev *et al.* [81]. Although the MD model is capable of handling polydisperse particles, this dissertation considers only a uniform particle size and shape since reliable data on size and shape distribution are not available. The aspect ratio is selected in order to minimize intercalation-induced stress, based on the results of Zhang *et al.* [40]. In this dissertation, three different REV sizes are considered: 10 μm, 20 μm, and 40 μm, which contain 10, 80, and 640 particles respectively. By scaling the number of particles with the total volume of the REV, an approximately constant equivalent particle size of about 5 μm can be maintained.

The MD simulation begins by randomly initializing the position and orientation of each particle, and sets the size of each particle to some infinitesimally small size. The size of the particles then proceeds to iteratively increase until they come into contact with one another, upon which they begin to translate and rotate based on a collision algorithm. This process continues until either the specified packing density (solid volume fraction) is reached, or a jamming condition is satisfied in which case the particles can no longer

move beyond some tolerance. At the end of the simulation, the particles are touching one another but do not overlap; in order to ensure that the particle cluster forms a single continuous solid object, the particle semi-axes are scaled by a constant overlap factor. Unless otherwise specified, an overlap factor of 1.1 is used in this dissertation.

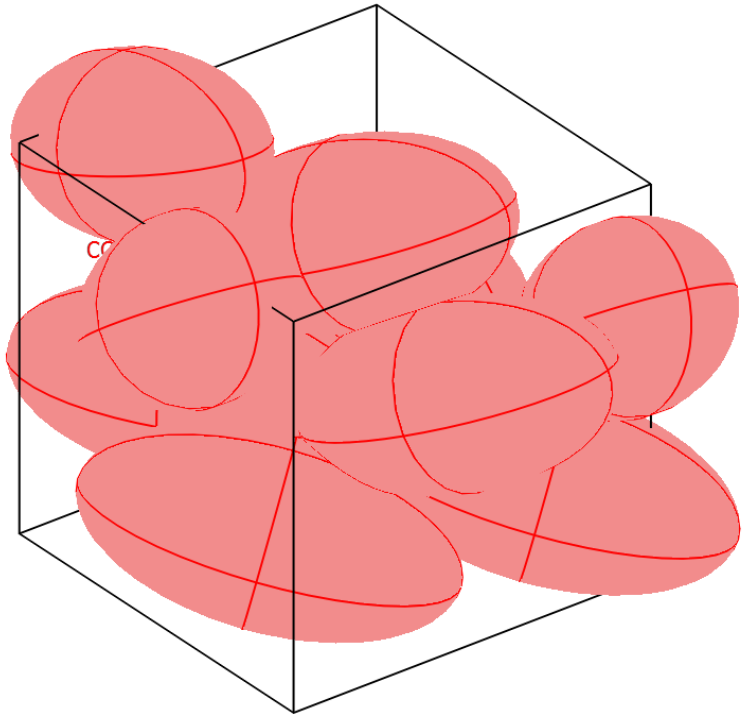

Figure 2-5: Sample packing geometry with 10 ellipsoidal particles

A sample 10 μm REV containing 10 particles with an overlap factor of 1.1 is shown in Figure 2-5. As a result of overlapping and the random nature of the MD algorithm, the particle size cannot be controlled exactly. However, an inspection of cases for the same number of particles shows a size variation of less than 10%, which is considered acceptable given that sizes of particles found in real battery electrodes often span several orders of magnitude. Also note that no other phases beyond active solid and liquid electrolytes are modeled. Therefore, macroscopic simulations used to verify results against the microscopic models do not include any inert binder. To finalize the geometry, portions of the particle cluster protruding outside the cubic REV are removed. Although this can result in irregularly shaped particles at the boundaries, this treatment is necessary to ensure a robust method for defining boundary conditions for a large number of REV. In the subsequent chapters, a single REV is sometimes referred to as a realization of the

particle packing geometry.

2.5.4 Voxel Meshing Algorithm

Although many different meshing approaches have been developed, a Cartesian voxel method is found to be most suitable for both the effective transport and interfacial reaction rate simulations. This voxel method has been previously applied to various engineering problems, including FEM investigation of biomechanical stress [82] and seismic ground motion [83]. As shown in Figure 2-6, which contains a high resolution voxel mesh of the same sample REV as in Figure 2-5, the rectangular mesh elements are arranged uniformly. In this dissertation, cubic mesh elements are used since the REV are cubic, although the voxel method only requires that the elements be rectangular. This method is especially well suited for problems in which a uniform mesh quality is required within the entire geometry. It is also very robust, as it ensures a consistent mesh quality, eliminating problems related to sharp edges and corners which often lead to highly stretched mesh elements when other methods are utilized.

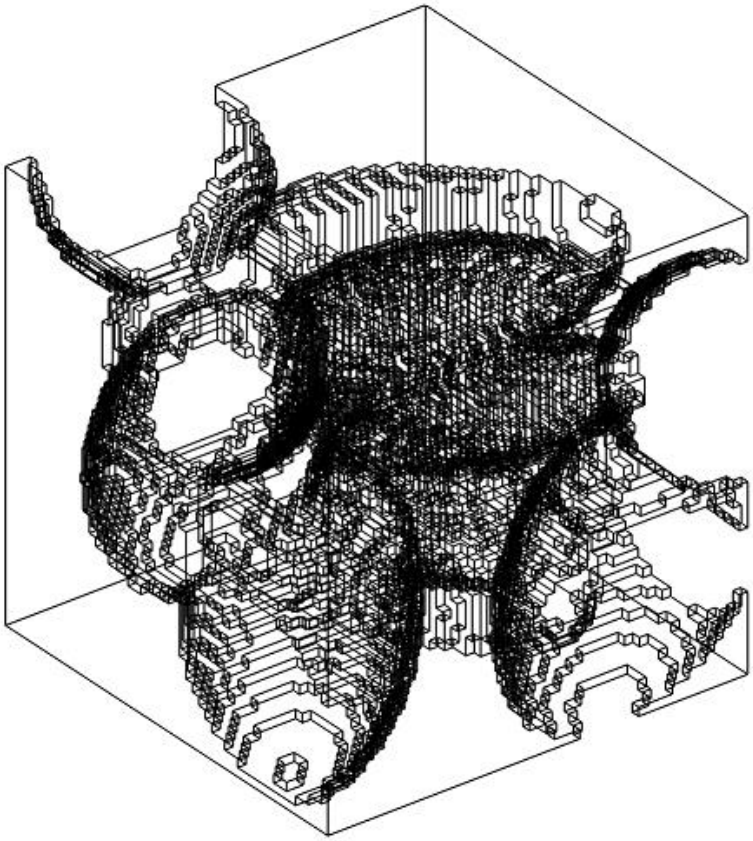

Figure 2-6: Voxel mesh of sample packing geometry with 10 particles

The main drawback of this meshing approach is that smooth diagonal edges and surfaces are modified due to the shape of the mesh elements. Therefore, it is not suitable for problems where the surface geometry must be preserved, and converges to mesh-independent solutions much more slowly than body-conforming meshing approaches. As an example, consider a single spherical particle inscribed within a cube. The volume fraction of the void around the sphere has an analytical solution:

$$\varepsilon_l = 1 - \rho = 1 - \frac{\pi}{6} \approx 0.4764 \tag{62}$$

As shown in Figure 2-7, a triangular mesh converges more closely to this exact value at $O(10^4)$ elements than the voxel mesh does at $O(10^6)$.

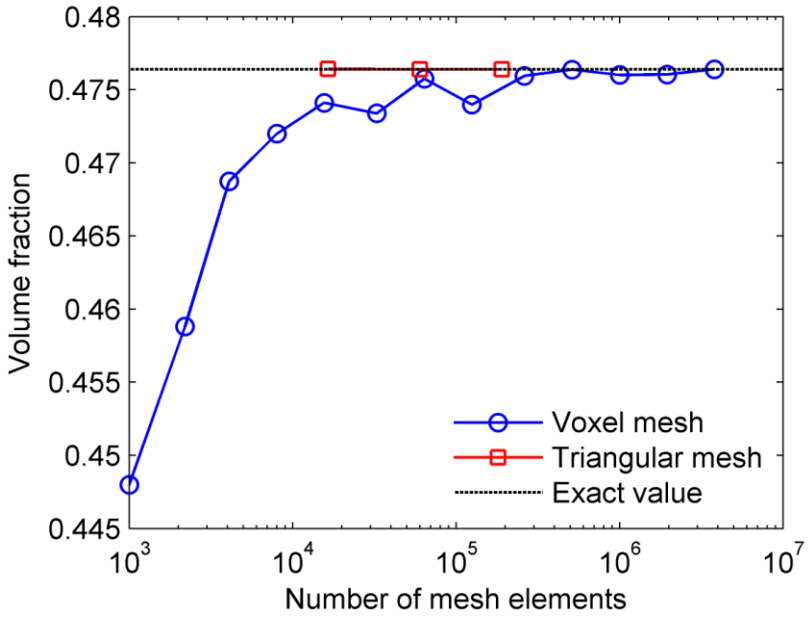

Figure 2-7: Volume fraction convergence of voxel and triangular meshes for sphere inscribed in a cube

This difference can be observed by comparing how the two meshing approaches manipulate the particle-void interface. In Figure 2-8, even for a quite fine mesh the cubic elements comprising the interface can be clearly seen. In contrast, at a comparable mesh resolution the triangular elements conform much more closely to the smooth spherical interface.

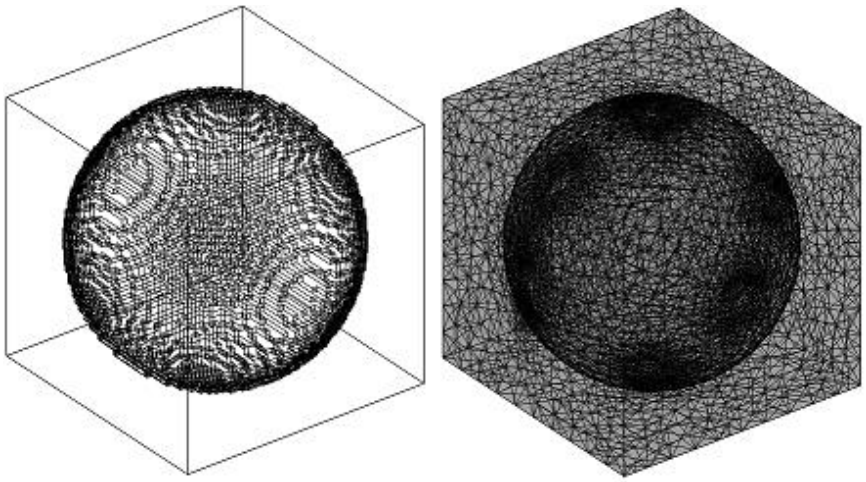

Figure 2-8: Comparison of voxel (left) and triangular (right) meshes with $O(10^5)$ elements

In spite of this inefficient convergence to mesh-independence and the loss in

precision, the robustness of the voxel meshing approach remains valuable, and compensates for its shortcomings. When body-conforming triangular meshes are applied, poor mesh quality at the interfaces between adjacent particles often requires considerable manual manipulation in the simulation setup process. Chapter 5.6 discusses the automated simulation framework that is enabled by the robustness of the voxel meshing approach. Except for in certain mesh sensitivity/convergence studies, a mesh resolution of 0.5 μm is used in this dissertation, which corresponds to a mesh size of 8.0×10^3, 6.4×10^4, and 5.1×10^5 mesh elements for the 10 μm, 20 μm, and 40 μm REV cases, respectively.

2.5.5 Graph Analysis

Graph analysis can be a useful tool to complement the FEM simulations, especially for the effective transport properties. Per Eq. (63), a graph is a mathematical structure comprising an ordered pair consisting of a set of vertices *V*, and edges *E* that connect them [84]:

$$G = (V, E) \tag{63}$$

Mathematically, the voxel mesh structure can be readily treated as a graph, in which the mesh elements are the vertices and interfaces between orthogonally adjacent mesh elements are the edges. A key concept in graph theory is the adjacency matrix, which contains information about which vertices in the graph are connected (adjacent) to which other vertices. The adjacency matrix can be constructed using the following rules:

$$\begin{aligned} A_{i,j} &= 1 \text{ if } i, j \text{ are adjacent} \\ A_{i,j} &= 0 \text{ otherwise} \end{aligned} \tag{64}$$

The adjacency matrix has the important property that $A^m_{i,j}$ gives the number of paths of exactly length *m* between vertices *i* and *j*. Within the voxel mesh, two vertices are considered to be adjacent if their corresponding mesh elements are adjacent AND they are both of the same phase (solid or liquid). This can be demonstrated using a simplified 2-D example.

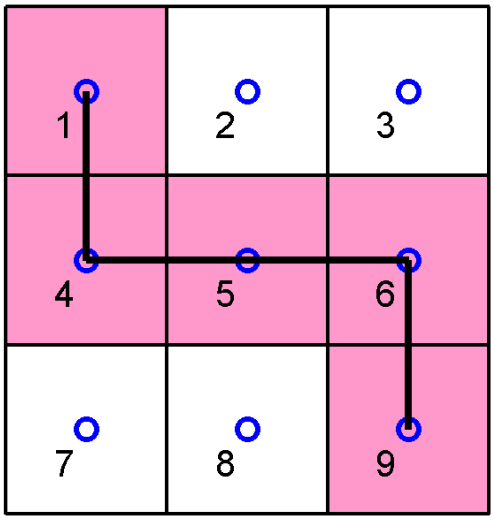

Figure 2-9: 2-D example of a microstructure graph

Figure 2-9 depicts a mesh consisting of 9 square cells, with the highlighted cells being the liquid phase through which ions diffuse. The nodes are numbered, and located at the cell centers. By applying Eq. (64), the adjacency matrix A for this graph is obtained:

$$A = \begin{bmatrix} 0 & 0 & 0 & 1 & 0 & 0 & 0 & 0 & 0 \\ 0 & 0 & 1 & 0 & 0 & 0 & 0 & 0 & 0 \\ 0 & 1 & 0 & 0 & 0 & 0 & 0 & 0 & 0 \\ 1 & 0 & 0 & 0 & 1 & 0 & 0 & 0 & 0 \\ 0 & 0 & 0 & 1 & 0 & 1 & 0 & 0 & 0 \\ 0 & 0 & 0 & 0 & 1 & 0 & 0 & 0 & 1 \\ 0 & 0 & 0 & 0 & 0 & 0 & 0 & 1 & 0 \\ 0 & 0 & 0 & 0 & 0 & 0 & 1 & 0 & 0 \\ 0 & 0 & 0 & 0 & 0 & 1 & 0 & 0 & 0 \end{bmatrix} \tag{65}$$

It can be verified by inspection that the property in Eq. (64) holds for this matrix and graph. Note that this matrix is symmetric, since the graph is bi-directional. It can also be readily seen that the shortest path from the top row to the bottom row has length 4, via the path 1→4→5→6→9. This path is also unique and thus the elements $A^4(1,9)$ and $A^4(9,1)$ should both be equal to 1. By computing the 4^{th} power of A, this can be verified by inspection:

$$A^4 = \begin{bmatrix} 2 & 0 & 0 & 0 & 3 & 0 & 0 & 0 & 1 \\ 0 & 1 & 0 & 0 & 0 & 0 & 0 & 0 & 0 \\ 0 & 0 & 1 & 0 & 0 & 0 & 0 & 0 & 0 \\ 0 & 0 & 0 & 5 & 0 & 4 & 0 & 0 & 0 \\ 3 & 0 & 0 & 0 & 6 & 0 & 0 & 0 & 3 \\ 0 & 0 & 0 & 4 & 0 & 5 & 0 & 0 & 0 \\ 0 & 0 & 0 & 0 & 0 & 0 & 1 & 0 & 0 \\ 0 & 0 & 0 & 0 & 0 & 0 & 0 & 1 & 0 \\ 1 & 0 & 0 & 0 & 3 & 0 & 0 & 0 & 2 \end{bmatrix} \tag{66}$$

Since Eq. (64) can be applied to define the adjacency matrix directly from the voxel mesh data, the number of paths between any two mesh elements within an REV can be determined by successively computing higher powers of the adjacency matrix. Note that the adjacency matrix has dimensions of $N \times N$, where N is the number of graph nodes (mesh elements). Since N scales with the cube of the number of mesh elements along a single dimension in the REV, n, the adjacency matrix has dimensions $n^3 \times n^3$. Also note that in 3-D, the adjacency matrix is less sparse than in 2-D, as each non-boundary node is adjacent to 6 neighboring nodes, compared to 4 in 2-D. Due to the unfavorable computational scaling with problem size, the graph analysis is limited to 10-particle cases in this dissertation. In Chapter 5.3, graph analysis is used to calculate the minimum diffusion path length across an REV, as well as the number of diffusion paths available for some fixed path length. These and other parameters can be used to quantify tortuosity in the microstructure, which has been established to be an important parameter for properly characterizing diffusivity and conductivity [85].

Chapter 3.
Surrogate-Based Analysis of the Cathode Design Space: Cycling Rate, Particle Size, and Transport Properties

3.1 Introduction

As discussed in Chapter 1, a critical obstacle to the adoption of lithium-ion batteries in various aerospace applications is their limited energy density. In order to gain a better understanding of the physical phenomena governing the behavior and performance of lithium-ion batteries, a systematic study of several critical design variables such as particle size and diffusivity, is necessary. Although many experimental and numerical studies have investigated the dependence of battery and cell performance on various operational, morphological, and material-dependent variables, they typically consist of parametric sweeps that sequentially vary one variable at a time. Examples of experimental investigations include Lu and Lin [86], who found experimentally that the capacity and coulomb efficiency of lithium manganese oxide particles increase substantially as the particle size is reduced. Similarly, Drezen *et al.* found that the size of lithium manganese phosphate particles in a cathode has a critical influence on the cell performance [87]. Tran *et al.* investigated the effect of cycling rate on the measured capacity of graphite anode particles, concluding that the rate effect differs considerably for different-sized particles [88]. The effect of introducing conductive additives to alter the electrode material properties has also been investigated by Ahn *et al.* [89]. It was found that metal fibers helped enhance capacity and high rate capability, while exhibiting minimal capacity loss.

Numerical simulations have also been used in similar studies, such as Garcia *et al.* [90], who used simulations to investigate the effects of particle size and diffusivity on cell performance. It was demonstrated that performance improves with increasing

diffusivity and decreasing particle size, and that the morphology of the particle aggregates also plays an important role. Darling and Newman also used simulations to examine the effect of particle size distribution [91]. A uniform size distribution was found to maximize capacity for different cycling rates. Zhang *et al.* have shown that larger particles and higher discharge rates lead to higher intercalation-induced stress [40]. Despite providing useful insight into the physical processes occurring within battery cells, these studies all employ inefficient methods and are tunable to account for nonlinear interactions between variables. Therefore, a proper multivariate analysis to study the complicated multi-physics phenomena within a lithium-ion cell is necessary. As described in Chapter 2.3, the surrogate modeling framework is ideal for this purpose.

In this chapter, simulations based on the macroscopic homogeneous battery cell model are used in conjunction with the surrogate modeling framework to examine the effect of cycling rate and of cathode properties (namely, the particle size, diffusion coefficient, and electronic conductivity within the cathode) on energy and power density. The following sections document the problem formulation, including the definition of the design variables and objective functions, as well as the process for constructing and cross-validating the surrogate models. This is followed by a discussion of refining the design space, performing global sensitivity analysis, and partitioning of the design space based on the GSA results and dimensional analysis. Specifically, a dimensionless time parameter based on the relative characteristic time scales for the discharge and diffusion processes is shown to be an excellent indicator of cell performance within a diffusion-limited operating regime. The chapter concludes with an analysis of the tradeoffs between the two objectives, energy and power. A significant portion of this chapter has been previously documented by Du *et al.* [47].

3.2 Problem Definition

The focus of this study, so the design variables (particle size, diffusivity, conductivity) apply only to the cathode material. The design variables modeled and their ranges are summarized in Table 3-1. The range of cycling rates is selected to roughly correspond to requirements in aerospace applications: the maximum rate of 4C refers to a

high-power situation in which the battery would be completely discharged in 15 minutes, such as the takeoff and climb section of a hybrid-electric airplane. The minimum rate of C/10 refers to a long-range or long-endurance situation lasting 10 hours, such as the nighttime period of a continuously operating high altitude solar flyer.

Table 3-1: Design variables and ranges for surrogate-based analysis

Variable	Symbol	Minimum	Maximum
Cycling rate	C	C/10	4C
Particle radius	$R_{s,p}$	0.2 μm	20 μm
Diffusion coefficient	$D_{s,p}$	0.1×10^{-13} m^2/s	10×10^{-13} m^2/s
Electronic conductivity	σ	1 S/m	100 S/m

Since the electrode can be assumed to be composed of multiple layers, the particle size range is selected to be an order of magnitude less than the electrode thicknesses, which are summarized in Table 3-2 along with other important simulation parameters. This range is also consistent with particle sizes found in real electrodes [92].

Table 3-2: Electrode materials and fixed simulation parameters

Parameter	Cathode	Anode
Material	$Li_yMn_2O_4$	Li_xC_6
Thickness	100 μm	100 μm
Initial stoichiometric parameter	0.2	0.495
Porosity (liquid volume fraction)	0.3	0.3
Inert filler volume fraction	0.2	0.1
Particle radius	Variable	10 μm
Diffusivity	Variable	5.0×10^{-13} m^2/s
Electrical conductivity	Variable	100 S/m

Data reported in the literature for transport properties, such as solid-phase diffusivity and electronic conductivity, varies substantially as a result of experimental

uncertainty, differences in electrode microstructure, phase changes due to different states of charge, and differences in measurement techniques [93, 94, 95, 96]. Ultimately, the ranges for the transport coeffients in Table 3-1 are chosen to (a) cover the order of magnitude difference in the reported literature values, and (b) account for the geometric characteristics of the electrode.

The primary objective function considered in this study is the energy density, also known as mass-specific energy or specific energy. The power density, also known as mass-specific power or specific power, is also considered in the context of tradeoffs between objectives. In this dissertation, the terms "energy density" and "specific energy" are used interchangeably, as are the terms "power density" and "specific power". The following is a description of how these objectives are calculated from the cell simulation data. The total energy is obtained by integrating the voltage curve obtained from the simulation over time, and multiplying by the discharge current and other appropriate constants, as shown in Eq. (2). This is computed using the trapezoidal approximation:

$$E = I_{sp} \sum_{i=1}^{N_t} \frac{V_i + V_{i-1}}{2} \left(t_i - t_{i-1} \right) \tag{67}$$

Dividing the total energy by the discharge time T_{dis} gives the time-averaged total power:

$$P = \frac{E}{T_{dis}} = \frac{I_{sp}}{T_{dis}} \sum_{i=1}^{N_t} \frac{V_i + V_{i-1}}{2} \left(t_i - t_{i-1} \right) \tag{68}$$

Finally, the mass-specific values of both quantities are obtained by dividing by the total cell mass, which includes the mass of the cathode, anode, separator, and current collectors:

$$m_{cell} = m_+ + m_- + m_0 + m_{cc} \tag{69}$$

In turn, the masses of each of these components can be calculated based on their thickness, and the volume fraction and density of their sub-components (solid, liquid, and inactive materials). Using the notation diagrammed in Figure 1-2:

$$m_+ = m_{s,+} + m_{l,+} + m_{i,+} = L_+ \left(\varepsilon_{s,+} \rho_{s,+} + \varepsilon_{l,+} \rho_l + \varepsilon_{i,+} \rho_{i,+} \right) \tag{70}$$

$$m_{-} = m_{s,-} + m_{l,-} + m_{i,-} = L_{-}\left(\varepsilon_{s,-}\rho_{s,-} + \varepsilon_{l,-}\rho_{l} + \varepsilon_{i,-}\rho_{i,-}\right) \tag{71}$$

$$m_0 = m_{i,0} = L_0\rho_l \tag{72}$$

$$m_{cc} = m_{cc,+} + m_{cc,-} = L_{cc,+}\rho_{cc,+} + L_{cc,-}\rho_{cc,-} \tag{73}$$

The volume fractions and thicknesses are listed in Table 3-2, while the densities are found in the database in version 5.1 of the `dualfoil` program. A cut-off voltage of 2.0 V is selected as the termination criterion for the simulations, in accordance with actual battery cycling in which deep discharge is avoided as it leads to permanent loss of performance due to irreversibility in the electrochemical reactions [97].

3.3 Error Estimation and Design Space Refinement

Before attempting to construct high fidelity surrogate models for the four design variables considered in this study, it is worthwhile to examine their impact within the selected range based solely on FCCD sampling. In this case, it is found that varying the electronic conductivity by two orders of magnitude within the specified range has a negligible effect on the energy density as compared to the variation recorded for the other variables (less than 1%). As a result, the number of design variables can be reduced prior to proceeding with the surrogate modeling procedure, by removing conductivity from future consideration. A constant value of σ = 10 S/m is used for the subsequent simulations.

An initial design of experiments of 50 design points consisting of a combination of 15 FCCD and 35 LHS points is selected. From these simulation data, a kriging model is found to have the lowest normalized PRESS from all 17 surrogate models considered. However, the PRESS value of about 20% is quite high, suggesting a need for design space refinement. A close inspection shows that of the 50 training data points, 3 outliers are located in the region with high cycling rate, large particle, size and low diffusivity, where a sharp gradient in the energy density is observed. This sparsely-populated "critical" region is populated by refining the design space such that an additional 100

design points are added to the original DOE. This is accomplished by applying a logarithmic transformation (base-10 log in this case) to the DOE sampling in linear space, leading to a concentration of sampling points near one extreme of the design space. For error estimation, 9 independent test points in the "critical" region are selected using the same logarithmic transformation, as well as 6 from other regions of the design space. A kriging model constructed from the data of the refined DOE (150 sampling points) exhibits a mean prediction error of 3.9% at the 9 transformed test points, a significant improvement compared to the 29.8% for the original DOE. However, its PRESS value is actually significantly increased compared to the original DOE, despite the refinement. This differing performance between the "critical" region and the rest of the design space suggests a shift in fidelity as a result of the domain refinement.

In order to improve overall surrogate model accuracy within the entire design space, an additional 165 are selected using LHS without applying the logarithmic transformation. The resulting set of training data consists of 315 points distributed over three levels of refinement, with about 100 points concentrated in the "critical" region. Multiple kriging, RBNN, and PRS surrogate models are considered. An additional of 64 test points are selected in a full factorial arrangement for a more detailed error assessment, and a modified definition of the relative prediction error definition is used to normalize the absolute error by a constant value, taken to be the mean value of all test data points:

$$err_i = \frac{\left|\hat{y}_i - y_{i,test}\right|}{\overline{y}_{test}} \tag{74}$$

This formulation helps avoid deceptively large errors due to normalizing by different test data values. A comparison among different types of surrogate models reveals that the best kriging model, with a spline correlation function and 1st-order polynomial regression, outperforms any RBNN or PRS model. This kriging model yields a mean prediction error of 2.5% at the test points and PRESS of 3.0%.

3.4 Global Sensitivity Analysis and Design Space Partitioning

A preliminary GSA of the entire design space using the kriging model shows a comparable magnitude of impact from all three design variables. As seen in Figure 3-1,

similar results are found when the analysis is applied to other classes of surrogate models.

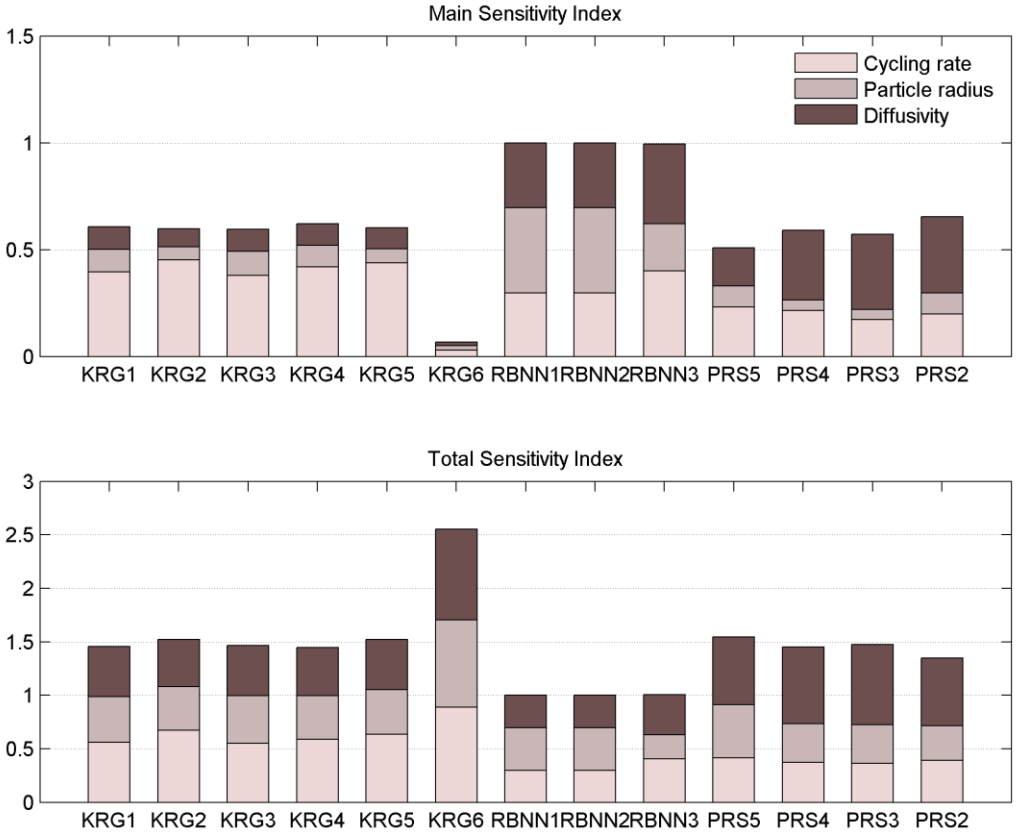

Figure 3-1: Main and total sensitivity indices for 13 surrogate models

In addition to performing GSA on the entire design space at once, it is also possible to compute local sensitivities by performing GSA on subsets of the data set. Figure 3-2 shows sensitivity indices computed on successively higher diffusivity ranges. It can be seen that the effect of diffusivity vanishes above a critical value of about $D_{s,crit}$ = 1.0×10^{-13} m^2/s. This is consistent with what may be expected from physica intution: as the diffusivity is increased, eventually a critical point would be reached where the allowable diffusion rate exceeds that required by the discharge process. Beyond this point, further increases to the diffusion coefficient would not affect the diffusion rate in the battery, as diffusion is no longer a limiting mechanism for the transport of lithium ions.

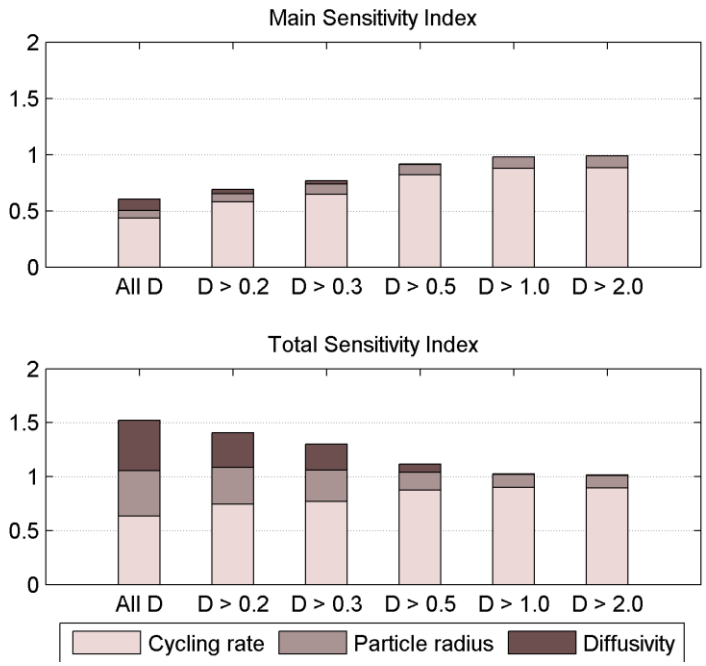

Figure 3-2: Main and total sensitivity indices for various diffusivity ranges

Since the effect of diffusivity is found to vanish beyond $D_{s,crit} = 1.0\times10^{-13}$ m^2/s, the design space can be partitioned into diffusion-independent ($D_s > D_{s,crit}$) and diffusion-dependent ($D_s \leq D_{s,crit}$) regions. Given the difficulty of accurately mapping the design space with a single global surrogate model, this partitioning of the design space is useful for better characterizing battery performance by reducing the number of variables and prediction error using multiple surrogates. For instance, it is clear that the diffusivity can be neglected as a design variable in the diffusion-independent operating regime, thus reducing the number of variables from 3 to 2.

Having identified one critical diffusivity value, it is natural to seek ways to further partition the design space. This can be accomplished by examining the dimensions/units in remaining design variables and applying dimensional analysis. Cycling rate has the same dimensions as frequency, or the inverse of time, while particle size is a measure of length. The diffusion coefficient includes both time and length, with dimensions of length squared divided by time. This suggests combining these quantities to obtain a physically meaningful dimensionless parameter. The diffusion coefficient $D_{s,p}$ appears in Eq. **Error! eference source not found.** of the cell model, whose corresponding length scale, as shown in Figure 1-2, is the particle radius $R_{s,p}$. These two variables can be combined to

yield a characteristic time scale for the diffusion equation:

$$t_{diffusion} = \frac{R_{s,p}^2}{D_{s,p}} \tag{75}$$

Physically, this quantity represents the approximate time it takes an ion to diffuse from the surface to the center of the spherical particle. Another important time scale is the time required to discharge the cell, which is estimated from the definition of cycling rate:

$$t_{discharge} = \frac{k}{C} \tag{76}$$

The constant k = 3600 seconds/hour ensures that the two length scales have consistent units. Eqs. (75) and (76) can thus be combined to define a dimensionless time parameter τ^* as the ratio of the two time scales:

$$\tau^* = \frac{t_{discharge}}{t_{diffusion}} = \frac{kD_{s,p}}{CR_{s,p}^2} \tag{77}$$

Physically, τ^* represents the relative speed of the diffusion and discharge processes. When the magnitude of τ^* is very large, ions travel much faster through the particle via diffusion than they are transferred across the cell. Conversely, when the magnitude of τ^* is very small, the cell utilization is limited by the diffusion rate. A plot of energy density against dimensionless time is shown in Figure 3-3, which only contains data points within the diffusion-dependent operating regime.

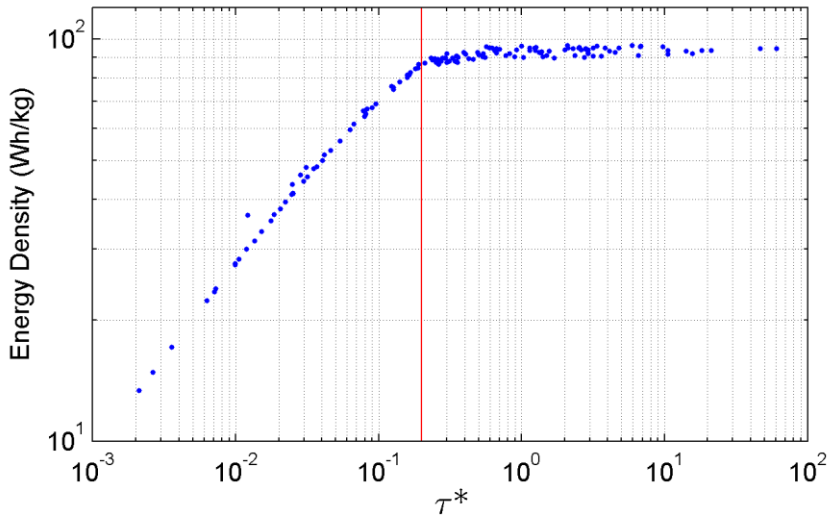

Figure 3-3: Energy density vs. dimensionless time for diffusion-dependent regime (D_s < 1.0×10^{-13} m^2/s)

Two distinct dimensionless time ranges can be identified in Figure 3-3. In the low τ^* range (left of the vertical line; $\tau^* \leq 0.2$), the specific energy increases monotonically with increasing τ^*; this can be considered a diffusion-limited region since the energy is limited by the allowable diffusion rate. In the high τ^* range ($\tau^* > 0.2$), the scatter in the energy values indicates that diffusion is no longer the sole determining factor, and that some interplay between variables is involved. This can be considered an intermediate region between the diffusion-limited and diffusion-independent regimes. Based on this observation, the diffusion-dependent region of the design space can be further partitioned into diffusion-limited and intermediate sub-regions. Figure 3-4 summarizes the final partitioning of the design space into three distinct operating regimes.

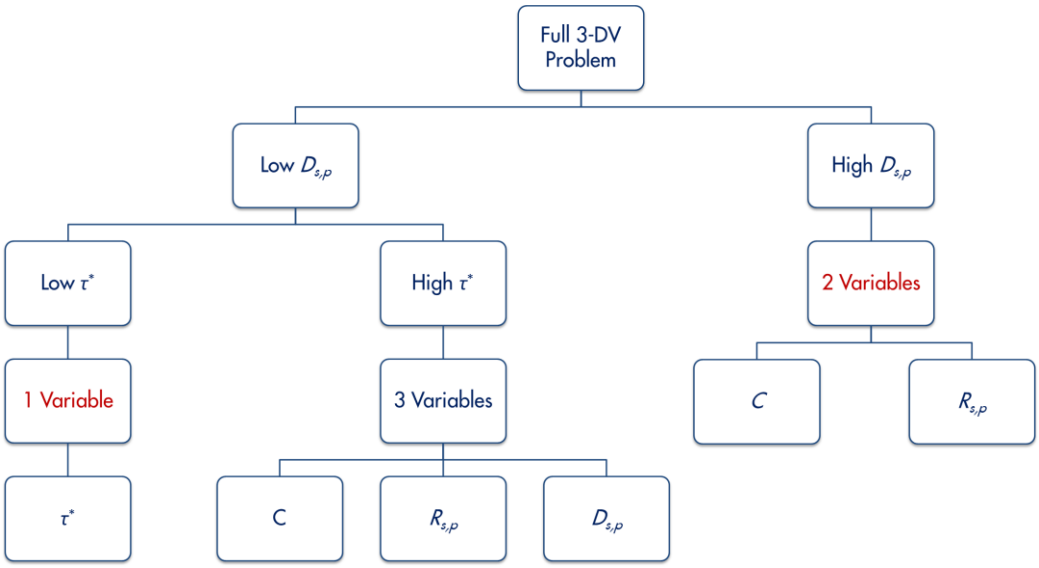

Figure 3-4: Overall process to split the original 3-design variable problem into three distinct regions using global sensitivity analysis and based on a critical value diffusivity value $D_{s,crit}$ = 1.0×10^{-13} m^2/s

In addition, note that two of the operating regimes have a reduced number of variables, facilitating the construction and error assessment of accurate surrogate models. And since the design space is split but not expanded, no new training data are required; the same design of experiments consisting of 315 training data points is sufficient to construct all three surrogate models.

The diffusion-limited region includes 42 training data points. As seen in Figure 3-5, a 4th-order PRS provides an excellent quality fit, with R^2 = 0.994.

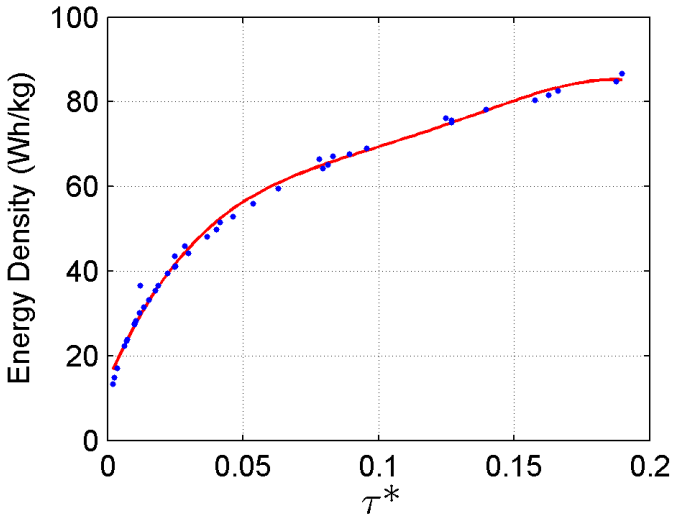

Figure 3-5: Polynomial regression fit for energy density with respect to dimensionless time parameter τ^* in the diffusion-limited region

Although the intermediate region retains full dimensionality, the ranges of the design variables are reduced, and model accuracy is improved considerably. As seen in the iso-surface plot in Figure 3-6, the energy density decreases considerably with increasing cycling rate and particle size, while the effect of diffusivity is reduced. The weaker effect of diffusivity can be expected since most of the global sensitivity with respect to this variable occurs in the diffusion-limited region. The kriging model has a PRESS value of 0.40%, and a mean test point prediction error of 0.30%, again indicating excellent accuracy.

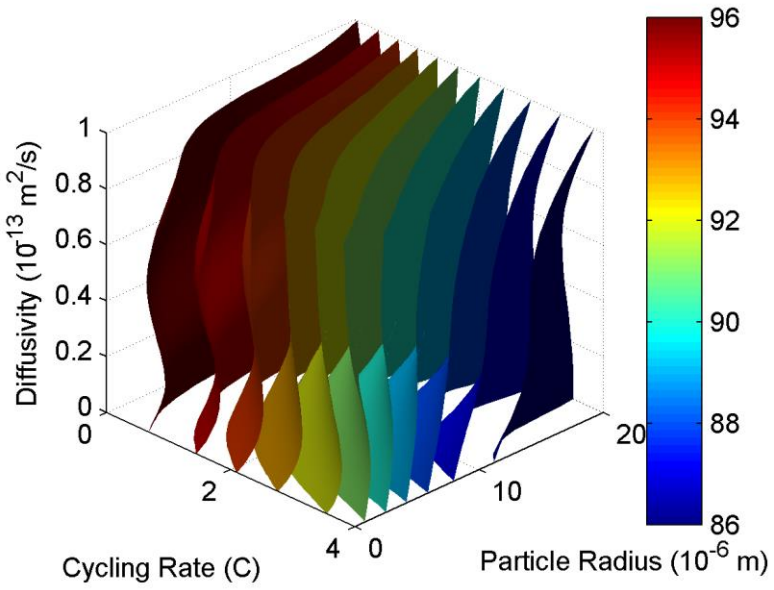

Figure 3-6: Iso-surfaces for energy density with respect to 3 design variables, based on kriging model in intermediate diffusion-dependent region

For the diffusion-independent regime, a reduced-order 2-variable surrogate model is constructed to fit the data in the range $D_s > 1.0\times10^{-13}$ m^2/s, with the response surface plotted in Figure 3-7. The PRESS value in this case is 1.4%.

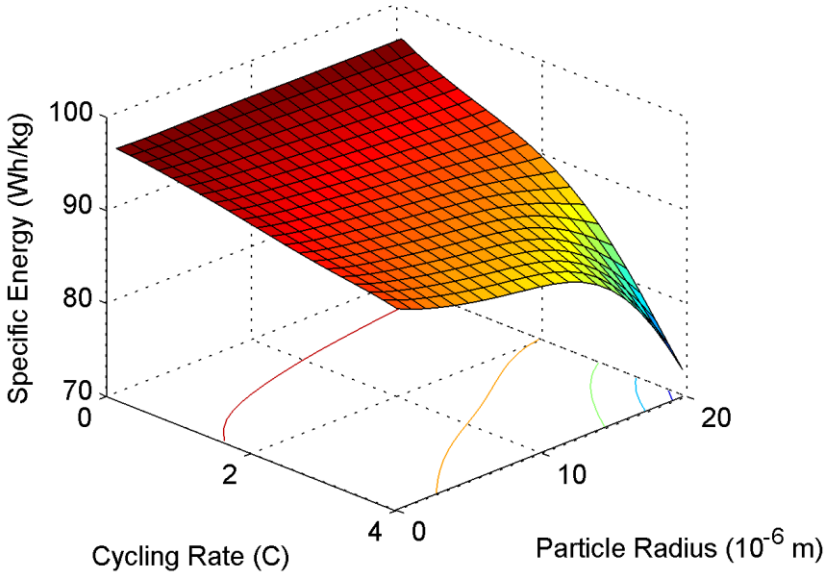

Figure 3-7: Response surface for energy density with respect to 2 design variables, based on kriging model in diffusion-independent regime

A summary of surrogate model quality based on PRESS is provided in Table 3-3.

It is clear that the design partitioning done in this study has greatly improved the quality of the surrogate model fit.

Table 3-3: Comparison of PRESS for full and partitioned design space

Surrogate Model	# of design variables	# of data points	PRESS
Unrefined	3	50	20%
Full (refined)	3	315	3.0%
D-limited	1	42	2.6%
Intermediate	3	81	0.57%
D-independent	2	32	0.40%

3.5 Tradeoffs Between Energy and Power

The results so far have focused exclusively on the energy density as the objective function, since as discussed that tends to be the most critical performance limitation in a variety of applications. However, power density can also be of great importance in applications such as electric automobiles and aircraft. Since the simulations thus far have been for a single discharge at constant current, the time-averaged power density is a good metric for characterizing power. Based on Eq. (68), which states that the power varies linearly with discharge current, the power can also be expected to have an approximately linear relationship with cycling rate since by definition the discharge current varies linearly with cycling rate. Given the previous results that energy density decreases with increasing cycling rate, power density and energy density thus form a pair of competing objectives in which a gain in one can only be achieved with a loss in the other. As discussed in Chapter 2.3.5, the tradeoff between these competing objectives can be analyzed using a Pareto front. Fortunately, Eq. (68) also provides an easy way to calculate power density from energy density, so no additional design of experiments or simulations are required.

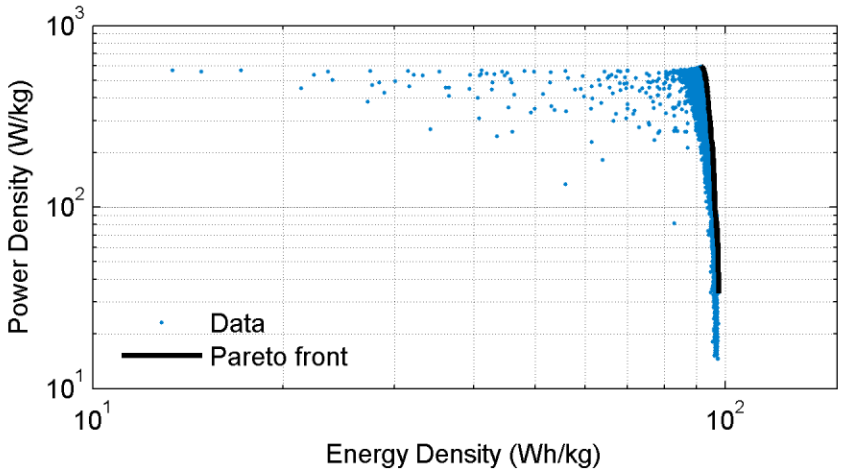

Figure 3-8: Pareto front for power-energy tradeoff

The Pareto front for quantifying tradeoffs between power and energy density is plotted in Figure 3-8. In order to properly populate the objective space, it is standard practice to use surrogate models as intermediate data generators for additional data samples. Approximately 6700 randomly sampled design points are used in this case. Specific energy data points are obtained using the surrogate models based on the split design space approach in Figure 3-4. Specific power data are generated using a separated surrogate model. A 4th-order PRS is found to have sufficient accuracy for this purpose, as its PRESS value is less than 0.4% and R^2 is over 0.9999. Since the specific power is expected to be linearly dependent on the cycling rate, the Pareto inefficiency for the majority of designs is expected to be due to the other design variables. This is verified by selecting three cases at a fixed cycling rate but at different particle sizes and diffusivities, which are highlighted with a different color in Figure 3-8. In the three cases, the power level is approximately the same, confirming the dependence of the specific power on only the cycling rate. The specific energy is also found to be lower for larger particle radius and lower diffusion coefficient, which is consistent with previous results.

The Pareto front shows stiffness in favor of high power, which can be achieved with relatively little sacrifice in energy. However, a greater amount of scatter in the specific energy data can also be observed as the specific power is increased, suggesting that the cell performance becomes increasingly sensitive to the other design variables as the cycling rate is increased, resulting in a greater penalty for large particle size or low diffusivity in the cathode. Furthermore, results for rates greater than 4C, shown in

Chapter 4.3, indicate that the relative sensitivity of power density and energy density to the cycling rate gradually decreases as the cycling rate is increased, and that at sufficiently high rates the Pareto front may become stiff in the other direction. This is consistent with typical Ragone plots for lithium-ion batteries [9], which plot the theoretical energy and power density of a battery or cell with fixed properties. The quantification of the shape of the Pareto front is important for designing battery systems for vehicles, as favorable tradeoffs between power and energy can be exploited via the configuration of individual cells within a battery pack (series for high voltage, parallel for high current). For example, if the power level required for the hybrid-electric configuration of the Cessna 172 in Chapter 1.3.4 is known, the Pareto front can be used to design the configuration of the battery back for maximizing energy density and aircraft range, for given constraints on the total weight.

3.6 Summary

In this chapter, the surrogate modeling framework presented in Chapter 2.3 is applied to the macroscopic homogeneous pseudo-2D porous electrode model, to study the effects of cycling rate, particle size, diffusivity, and conductivity on the energy and power density performance of a lithium-ion battery cell. The cell energy density is found to diminish with faster cycling rate, larger particles, and low diffusivity, which is consistent with experimental and numerical findings documented in the literature. A preliminary analysis based on FCCD sampling points is adequate for establishing that the electronic conductivity has a negligible influence on the cell performance within the 1-100 S/m range, allowing the number of design variables to be considered in subsequent analysis to be reduced. In addition to the initial design of experiments, two levels of refinement are required to properly distribute additional sampling points and achieve normalized PRESS and prediction errors of about 3%. The trends identified using the surrogate model suggest a link between the relative discharge and diffusion rate, and the utilization of the cell. This relationship is quantified in terms of the characteristic time scales.

GSA performed on subsets of the simulation data is able to identify a critical value for the diffusion coefficient of $D_s = 1.0\times10^{-13}$ m^2/s, above which the cell becomes

diffusion-independent. By defining a dimensionless time parameter τ^* as the ratio of characteristic time scales corresponding to the discharge and diffusion processes, the design space can be further partitioned to form three distinct operating regimes in which the principal mechanisms for limiting cell performance differ. In the diffusion-independent region, cycling rate and particle size are sufficient to characterize the cell performance. Meanwhile, in the diffusion-limited regime where τ^* takes on values much less than unity, the energy density can be accurately calculated from τ^* alone since diffusion becomes the bottleneck to the entire coupled multiphysics system. Although the number of design variables cannot be reduced in the intermediate region, a much more accurate surrogate model can be constructed in comparison to the global design space.

The improvement in surrogate model prediction accuracy in each of the design subregions illustrates the value of performing global sensitivity analysis and defining dimensionless parameters. This is especially apparent in the consideration of multiple objectives, as the accurate subregion surrogate models are used to construct a Pareto front to quantify the tradeoffs between energy and power density, from a much larger design of experiments. For this Pareto front, the power density shows a much greater sensitivity to cycling rate than the energy density, suggesting a favorable tradeoff in which significant gains in power density can be achieved with minimal sacrifice in energy density up to cycling rates of 4C. This is especially valuable for high power applications such as the takeoff phase for general aviation and the eclipse period for high-power satellites, since the Pareto front can be used to design the configuration of individual cells within a battery pack, for a given application's energy and power requirements.

Note that the energy density values (90-100 Wh/kg) obtained in this study are much lower than required by the systems discussed in Chapter 1 (200+ Wh/kg). This is due to the use of a limited SOC window for the simulations, and a lack of optimization for certain important properties such as porosity and thickness, or for anode properties. However, the surrogate model establishes a clear relationship between cycling rate, energy density, and power density, allowing simple sizing calculations to be made for the battery pack. For example, if the total required power for an aircraft or spacecraft is known, the minimum battery pack size required to achieve the appropriate cycling rate can be calculated from the definition of the dimensionless parameter τ^*. Chapter 4

extends the analysis presented in this chapter, to analyze and optimize the cathode porosity and thickness, two variables that have much more complicated interactions with the other variables which lead to non-monotonic trends in energy performance. The anode thickness is also varied to achieve capacity balance in the two electrodes. The surrogate modeling framework is then applied again to compare multiple candidate cathode materials, and additional dimensionless parameters are defined to better characterize cell performance for multiple materials.

Chapter 4.
Surrogate- and Gradient-Based Optimization of Multiple Cathode Materials

4.1 Introduction

In Chapter 3, it was found that energy density increases with lower cycling rate, smaller particle size, and higher diffusivity. Optimizing these variables would be a trivial task, as the optimized solution would converge to the bounds of the design space. These results are not surprising, as they make intuitive sense and have been established empirically. This does not mean that the results in that chapter are not meaningful; the error estimation and domain refinement for the surrogate models are non-obvious and useful results for understanding battery performance, as is the quantification of global sensitivities. Nonetheless, it would be useful to consider additional variables, especially those that are unlikely to converge to the bounds due to competing physical phenomena. The purpose of this chapter is to extend the analysis techniques from the previous chapter to obtain useful insights towards cell design.

In this chapter, the porosity and thickness of the cathode are added to the design space, and the bounds on the previously considered variables (cycling rate, diffusivity, and conductivity) are extended for a more comprehensive analysis. Two gradient-based approaches are used to find the optima: applying the optimizer directly to the cell model, and applying it to the surrogate function. A comparison of the accuracy and computational cost of the two approaches is made based on three test cases representing distinct operating scenarios. Finally, it is important to keep in mind that cell design also involves the selection of materials for the electrodes. Therefore, the chapter concludes with a comparison of several cathode materials based on the definition of dimensionless parameters using dimensional analysis. The approach and results presented in sections 4.1-4.3 and 4.4 of this chapter have been previously documented in references [98] and

[99], respectively.

4.2 Optimization of Electrode Porosity and Thickness

4.2.1 Problem Setup

Unlike the design variables considered in Chapter 3, the effects of electrode porosity and thickness on cell performance are not monotonic due to the presence of competing phenomena. Specifically, Eq. (21) shows that a higher porosity allows for a higher ion and electron transport rate, which as shown in Chapter 3, improves the energy performance of the cell. However, since porosity is defined as the volume fraction of electrolyte in the porous matrix, an increase in porosity also leads to a decrease in the amount of active solid material, and thus a reduction in the total capacity of the cell. Similarly, a thick electrode may be favored to increase the capacity of the cell, but at high cycling rates the diffusivity of the material may be insufficient to utilize the additional material, resulting in insufficient gains in total energy to compensate for the additional mass. These competing non-linear effects suggest a greater need to properly identify optima in the design space using the gradient-based optimizer.

To optimize electrode porosity and thickness, two different approaches are taken, although they make use of similar tools. As shown in Figure 4-1, a common gradient-based optimizer is applied in two ways: directly to the cell model, and to a surrogate model trained from simulations using the cell model. Also note that global sensitivity analysis forms a continuous loop with the surrogate model, as the surrogate model can be successively refined based on the GSA results.

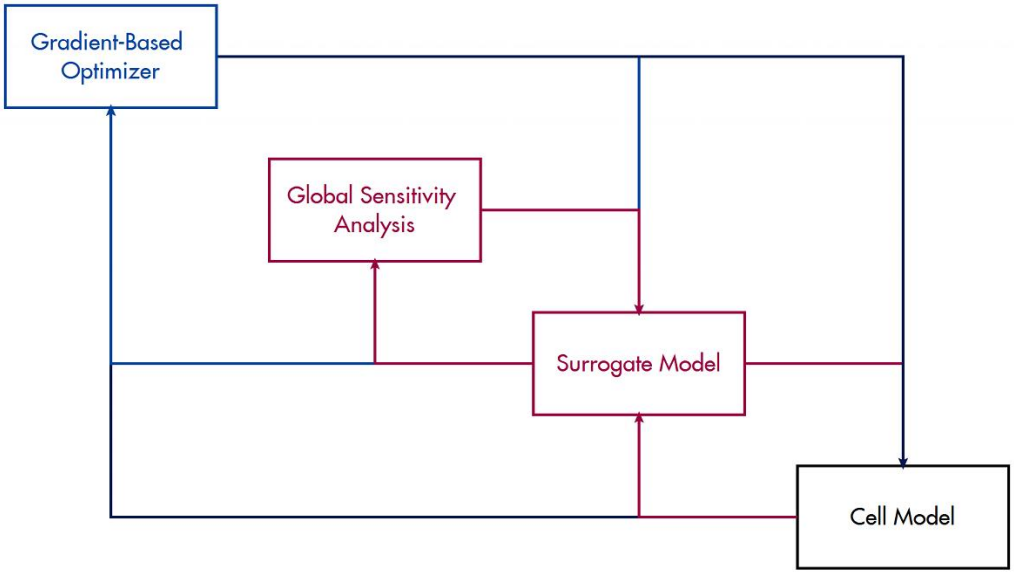

Figure 4-1: Process for combining analysis and optimization tools

The two approaches each have their own merits and can provide different information. When the optimizer uses output directly from the cell model instead of relying on a surrogate approximation of the objective function, the solution has one fewer source of error. This is especially critical in this case due to the "curse of dimensionality" as the number of variables is increased, making it difficult to fit an accurate global surrogate model. Consequently, the direct approach provides much more accurate solutions. The drawback, however, of using the cell model directly for optimization is that the computational cost of each function evaluation is several orders of magnitude greater ($O(10^{1}\text{-}10^{2})$ vs. $O(10^{-1})$ seconds). Additionally, in a design space with a large number of design variables each spanning a broad range of values, there are often multiple distinct physical situations of interest with unique constraints on the variables. A single surrogate model can be used for many such constrained design problems, further reducing the computational cost compared to repeatedly setting up a new constrained optimization problem using only the cell model. Therefore, an overall strategy of combining the two optimization approaches can be useful for taking advantage of the unique characteristics of the individual numerical tools, as well as providing a platform for comparing their accuracy and computational efficiency. Finally, combining the two approaches can improve the robustness of the optimization framework by identifying discontinuities and local optima in the design space that may cause the optimizer to

converge to the incorrect solution.

As in Chapter 3, the objective function of interest is the energy density, or mass-specific energy. The design variables and corresponding ranges considered in this study are summarized in Table 4-1. Note that compared to Table 3-1, the ranges for cycling rate and diffusivity have been significantly expanded and span two or more orders of magnitude. Therefore, they (along with particle radius) are normalized via a logarithmic transformation:

$$f(x) \rightarrow g(\log_{10} x) \tag{78}$$

This transformation allows the full range of magnitudes to be sampled and mapped. Also note that due to the homogenization assumptions in the cell model, porosity is defined as the volume fraction of liquid electrolyte in the cathode.

Table 4-1: Design variables and ranges for cathode porosity/thickness optimization

Design Variable	Minimum	Maximum
Cycling rate*	C/10	10C
Particle radius*	0.2 μm	20 μm
Diffusion coefficient*	1×10^{-16} m^2/s	1×10^{-11} m^2/s
Electronic conductivity	1 S/m	10 S/m
Electrode thickness	40 μm	150 μm
Porosity	0.2	0.4

* Design variables normalized via log-scale transformation

The fixed simulation parameters used in this study are listed in Table 4-2. It is important to point out the differences between this problem setup and that in Chapter 3. Varying the cathode porosity and thickness alters the capacity, and suggests a need to vary the anode properties accordingly to retain charge balance. This is achieved in this case by fixing the anode porosity but varying the anode thickness to balance the theoretical charge capacities of the two electrodes based on their material properties (see Table 4-7). The reference current value used to convert between discharge current and C-

rate is computed separately for each case based on the theoretical capacity of the solid electrode materials, solid volume fraction, and electrode thickness. A single constant-current discharge cycle is simulated for each case, and a cut-off voltage of 3.0 V is used as the termination criterion. Note that this higher cut-off voltage value is necessitated by numerical convergence difficulties due to stiffness in the radial diffusion equation when the diffusion coefficient is very low. Although the Crank-Nicolson finite-difference method [100] works well in most cases, terminating the simulations at 3.0 V instead of 2.0 V results in a significant reduction in computational time for the highly stiff cases while giving very similar results for the overall cell energy density.

Table 4-2: Fixed cell simulation parameter values for cathode porosity/thickness optimization

Parameter	Value
Initial stoichiometric parameter for anode (x in Li_xC_6)	0.6
Initial stoichiometric parameter for cathode (y in $Li_yMn_2O_4$)	0.2
Cut-off voltage	3.0 V
Separator thickness	25 μm
Positive current collector thickness	25 μm
Negative current collector thickness	25 μm
Initial salt concentration	1000 mol/m^3
Ambient temperature	298 K
Diffusion coefficient in anode (solid; bulk)	5.0×10^{-13} m^2/s
Electronic conductivity in anode (solid; bulk)	100 S/m
Particle radius in anode	10 μm
Volume fraction of inert filler in cathode	0.1
Volume fraction of inert filler in anode	0.05
Anode material (solid)	MCMB 2528 graphite
Electrolyte material	$LiPF_6$ in EC:DMC
Inert filler material	PVDF

4.2.2 Surrogate Model Refinement and Parameter Optimization

The initial design of experiments consists of 77 FCCD and 600 LHS points, for 677 total training data points. For error assessment, 21 design points are chosen for the independent testing data set such that the distance between test points and training data points in the design space is maximized. This is equal to 10% of the number of coefficients in a 4^{th}-order polynomial function in six design variables. The specific energy values range from a maximum of about 170 Wh/kg under ideal conditions (minimum cycling rate and particle size) to nearly zero for the opposite extreme (maximum cycling rate and minimum diffusivity). From among a total of 17 surrogate models (PRS, KRG, and RBNN), the kriging model with Gaussian correlation function has the best accuracy: normalized PRESS value of 8.81% and normalized RMS prediction error at the test points of 8.70%; these values are too high to conduct optimization and thus a refinement is needed. As in Chapter 3, GSA is performed to establish an effective strategy for refining the design of experiments.

Main and total indices are shown in Figure 4-2, along with those from Chapter 3 for comparison. Note that in both cases, the effect of conductivity is negligible, even though as shown in Table 4-1 the range for conductivity has been substantially expanded. Porosity is found to have a weak main effect, but strong higher-order effects. Based on these results, the conductivity is eliminated from consideration to reduce the problem dimensionality from six to five variables.

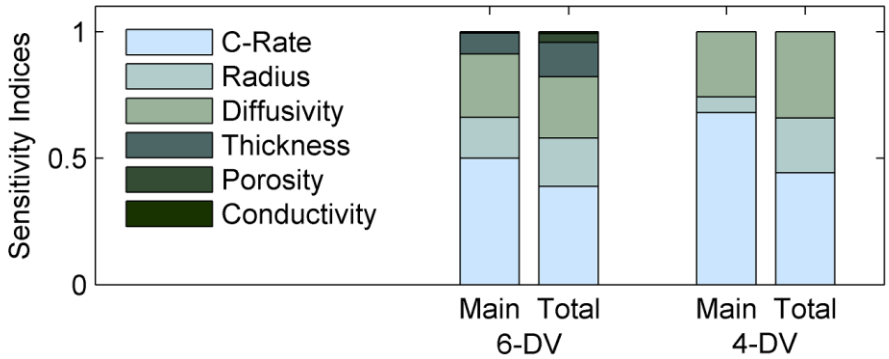

Figure 4-2: Normalized sensitivity indices for 6- and 4-variable designs of experiments

The error measures in Table 4-3 show that this simple problem reduction is able

to significantly able to improve the accuracy of the surrogate model, without the addition of any design points. For further refinement, an additional 381 points are added using a LHS filling strategy, to yield a total of 1024 training data points. Note that some of the FCCD points were removed due to redundancy resulting from the reduction in problem dimensionality. Due to the higher order of polynomials that can be fit with the refined design of experiments, another 81 independent test points are added, bringing the total to 102. This corresponds to 10% of the size of the design of experiments. Comparing the "refined" and "initial" kriging models in Table 4-3 shows that the problem reduction and design space refinement together roughly cut all measures in half.

Table 4-3: Error measures for kriging models based on different designs of experiments and refinement levels

Design of Experiments/Model	**Initial**	**Reduced**	**Refined**	**Optimized**
Number of design variables	6	5	5	5
Refinement level	Unrefined	Unrefined	Refined	Refined
Optimization	None	None	None	Optimized
Number of data points	677	643	1024	1024
PRESS (RMS)	0.0881	0.0655	0.0423	0.0375
RMS test prediction error	0.0870	0.0637	0.0364	0.0311
Maximum test prediction error	0.2002	0.1646	0.1057	0.0681

A final step to improve the surrogate model's predictive capability can be taken without requiring any additional training data, by optimizing the parameters within the surrogate model. The Gaussian correlation function can be written:

$$R(\mathbf{x}) = \prod_{j=1}^{n} \exp(-\theta_j d_j^2) \tag{79}$$

A constant value is typically used for the correlation coefficients θ_j:

$$\theta_j = N_p^{-\frac{1}{N_v}} \tag{80}$$

Although a routine exists within the MATLAB toolbox to automatically choose appropriate values of θ_j for each j [63], initial values must be specified by the user. It has been observed that the error measures are sensitive to these initial values, suggesting that improvements to model fit can be achieved by properly tuning them. To accomplish this, the MATLAB optimizer `fmincon`, which as explained in Chapter 2.4 is an implementation of the SQP method described in conjunction with the BFGS method for estimating the Hessian matrix [76], is applied to find optimal values for the coefficients by minimizing the following prediction error measure:

$$\text{Error}\left(\theta_1,\ldots,\theta_{N_v}\right) = \max\left(\varepsilon\right)\sqrt{\frac{1}{N_t}\sum_{i=1}^{N_t}\varepsilon_i^{\,2}} \tag{81}$$

Note that this is simply a product of the RMS and maximum prediction errors ε at the t independent test points. This measure is selected to reduce both the RMS and maximum prediction errors, as these are two of the best indicators for surrogate model accuracy. Table 4-3 shows a continuation of the reduction in all three error measures with each iteration of the surrogate model. With RMS error measures of about 3%, this surrogate model is sufficiently accurate to proceed with the optimization of cathode porosity and thickness.

4.3 Comparison of Surrogate- and Gradient-Based Methods

It has been previously established that energy density improves with lower cycling rate, smaller particle size, and greater diffusivity due to improved material utilization and reduced impedance. However, the effects of electrode thickness and porosity are more complicated, since they involve competing phenomena. In addition to finding the maximum energy density value, the surrogate model is also used to explore the dependence of optimal values of certain design variables with respect to other variables. For instance, of interest is not only the single optimal electrode porosity or thickness value for a given set of constraints, but also the dependence of this optimum on varying constraints.

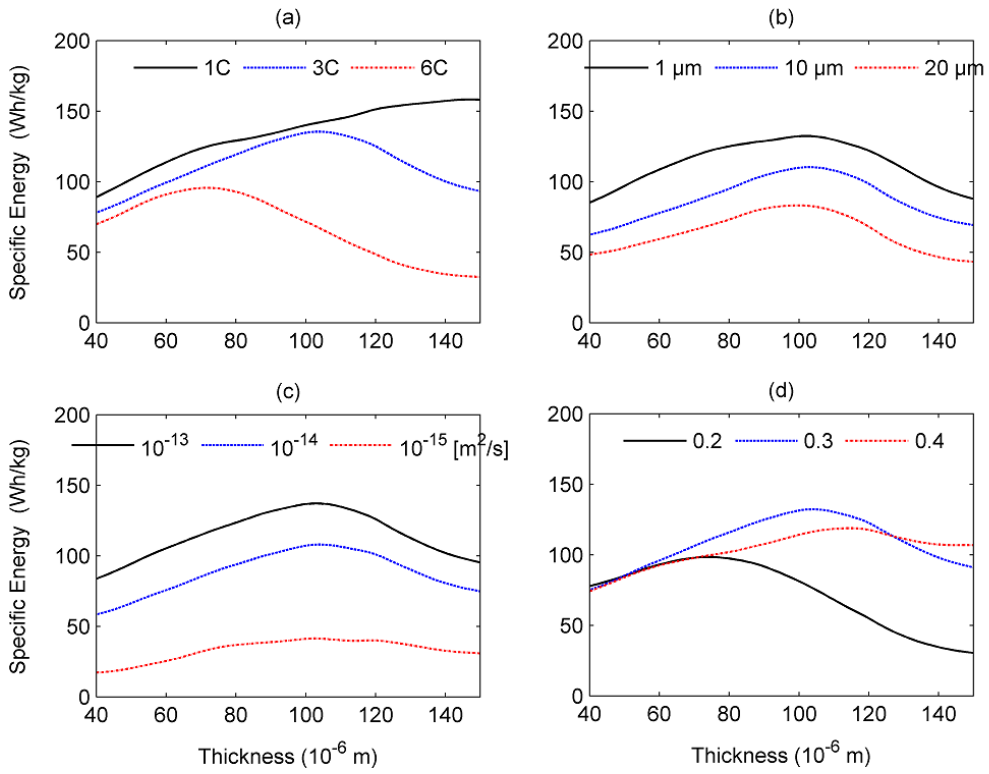

Figure 4-3: Dependence of optimal thickness on (a) cycling rate; (b) particle radius; (c) diffusion coefficient; (d) porosity

As an example, Figure 4-3 contains four examples of the objective function plotted over 1-D sweeps of the design space for three discrete values of each design variable, generated using the most refined surrogate model. Although these plots only represent a few examples of the much larger multidimensional design space, it is clear that optimization an electrode's thickness is difficult as the optimal thickness varies considerably with cycling rate. This means that, for example, a cell with a 150-μm cathode designed for maximum energy density at 1C operation would perform worse than one with a 100-μm cathode at higher cycling rates. As stated in section 4.2.1, this difficulty presents an excellent opportunity to demonstrate the benefits of combining available numerical tools, and to compare the relative merits of the two optimization approaches.

Therefore, to demonstrate this modeling framework, and to further examine the relationship between optimal thickness and porosity and the values of the other design variables, both the direct gradient-based (SNOPT applied to the `dualfoil` program) and the surrogate-based (`fmincon` applied to the surrogate model) approaches are

applied to the three optimization cases summarized in Table 4-4 are selected.

Table 4-4: Design conditions for optimization cases

Case Number	C-Rate	Particle Radius	Diffusion Coefficient
1	C/10	0.2 μm	1×10^{-12} m^2/s
2	2C	2 μm	1×10^{-14} m^2/s
3	10C	2 μm	1×10^{-14} m^2/s

These cases correspond to three significantly different design scenarios:

i. Case 1 is a situation in which the characteristic diffusion time scale, as defined in Eq. (75), is much smaller than the discharge time scale due to the small particle size and high diffusion coefficient, so the cell is not limited by the diffusion rate. Therefore, the cell is expected to have good utilization of a high electronic capacity.

ii. Case 2 models a high cycling rate corresponding to a high performance situation in an electric vehicle, and with a much lower diffusion coefficient and larger particles, diffusion is expected to become a limiting factor in the cell performance.

iii. Case 3 models the maximum discharge rate scenario, and capacity utilization is expected to be poor.

Contour plots of the objective function over the 2-D thickness-porosity design space for Cases 1-3 are shown in Figure 4-4-Figure 4-6, respectively. The locations of the optimal designs identified by the two optimization approaches are also shown, as well as contour plots of the relative difference between the actual cell data and predicted output from the surrogate model.

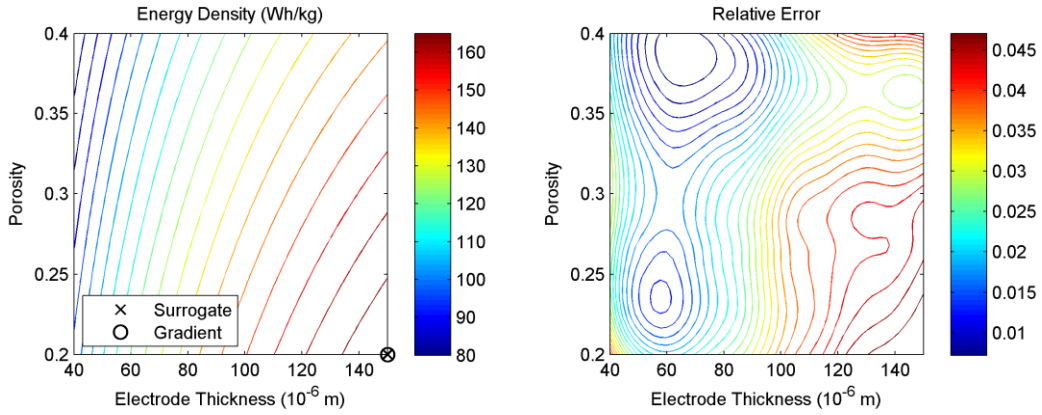

Figure 4-4: Contour plot of energy density (Wh/kg) against cathode thickness and porosity for Case 1 (high diffusion, low C-rate)

In Case 1, as shown in Figure 4-4, both optimization methods identify the optimum at the lower right corner. This indicates that the thickest electrode with minimum porosity (and thus maximum solid volume fraction) is preferred. Since the diffusion rate is not a limiting factor in this case, greater energy can be extracted by increasing the amount of active solid material in the electrode. However, it is important to note that although the two methods converge to the same solution in the design space, Figure 4-4 and Table 4-5 show that they yield objective function values that differ by a few percent. Case 1 demonstrates that even when the surrogate model can be used to predict the correct optimum, the function value still contains uncertainty due to prediction error in the surrogate model.

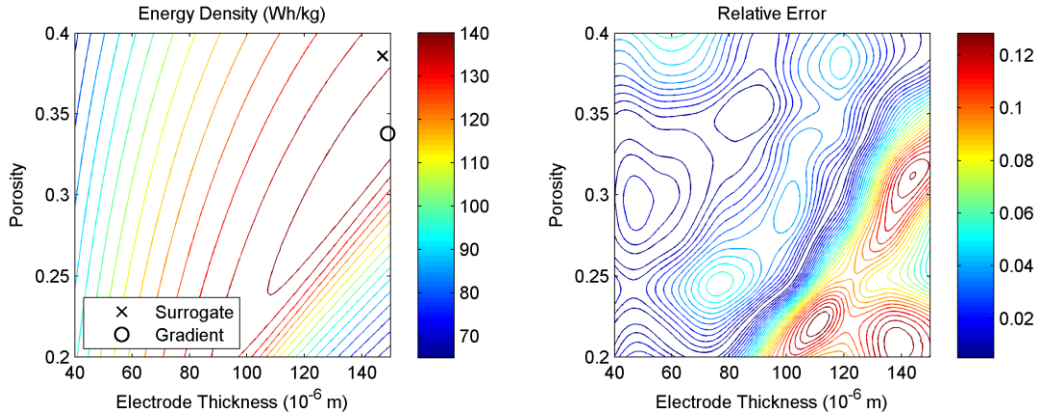

Figure 4-5: Contour plot of energy density (Wh/kg) against cathode thickness and porosity for Case 2 (low diffusion, high C-rate)

In contrast to Case 1, the diffusion rate is a limiting factor in Case 2. As shown in Figure 4-5, the lower-right corner, which was the optimal design region for Case 1,

shows poor performance in Case 2. In this scenario, the diffusion rate is insufficient to accommodate an electrode that is both thick and dense. Instead, the optimum is located in the upper-right region of the design space, where the electrode is thick but much more porous. Unlike in the previous case, the two methods converge to different solutions in the design space. However, despite this difference, Table 4-5 shows that the final energy density values again differ by only 2.5%, suggesting that the optimum lies in a flat region of the design space where the objective function is not sensitive to the design variables. This is supported by the distribution of contours in Figure 4-5, where a large region of the design space gives an energy density within about 10% of the maximum value of 143.2 Wh/kg. In fact, reasonable performance can be achieved with a much lower porosity, as long as the thickness is reduced to about 100 µm.

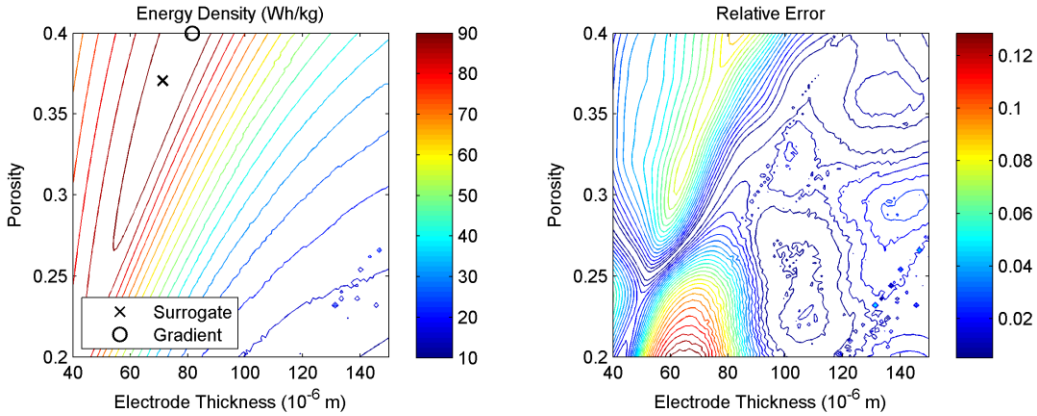

Figure 4-6: Contour plot of energy density (Wh/kg) against cathode thickness and porosity for Case 3 (low diffusion, maximum C-rate)

Finally, Case 3 shows that for very high cycling rates, a much thinner electrode is required, and that porosity may be a limiting factor. As seen in Figure 4-6, the gradient-based optimizer converges to the upper bound for porosity, suggesting even higher porosity levels for designing cells for high power applications. Note that the energy density values for Case 3 are much lower than in Case 2, which in turn are lower than in Case 1. This is consistent with the established understanding that energy performance diminishes with increasing discharge rate. Also note that in Figure 4-4-Figure 4-6, the contour lines are more vertical than horizontal. This is an indication that the objective function is more sensitive to thickness than to porosity, which is consistent with the global sensitivity analysis results in Figure 4-2.

Table 4-5: Comparison of optimal solutions obtained using surrogate- and gradient-based approaches

Case	Surrogate-Base Optimum			Gradient-Based Optimum			Normalized Difference
	δ (μm)	ε	E (Wh/kg)	δ (μm)	ε	E (Wh/kg)	
1	150.0	0.200	181.4	150.0	0.200	170.4	+6.4%
2	147.3	0.386	138.9	149.0	0.338	143.2	-2.5%
3	71.2	0.371	80.6	81.5	0.400	94.1	-7.9%

The accuracy of the surrogate model can be assessed by examining the relative error contours in Figure 4-4-Figure 4-6, as well as the optimal solutions tabulated in Table 1-1. Since the gradient-based approach uses the cell simulation directly, its optimization solution is considered the "exact" solution used to calculate errors. Generally, the surrogate model is able to provide solutions to within about 5%, although the error can exceed 10% in a few isolated pockets. The benefits of each method are thus demonstrated: the surrogate model provides computationally cheap approximations of the objective function, allowing for an efficient analysis of the full design space and a rough optimization. And although only three cases are shown, it is important to remember that the surrogate model maps the entire design space and is therefore able to optimize the porosity and thickness for arbitrary operating conditions. However, in cases where greater accuracy in the optimized solution is required, the gradient-based method must be used. In turn, a global mapping of the design space provided by the surrogate model complements the accuracy of the gradient-based optimizer to provide better insight into the physical phenomena being modeled. The optimization results are consistent with the established practice of using thick electrodes in high energy applications and thin electrodes in high power applications.

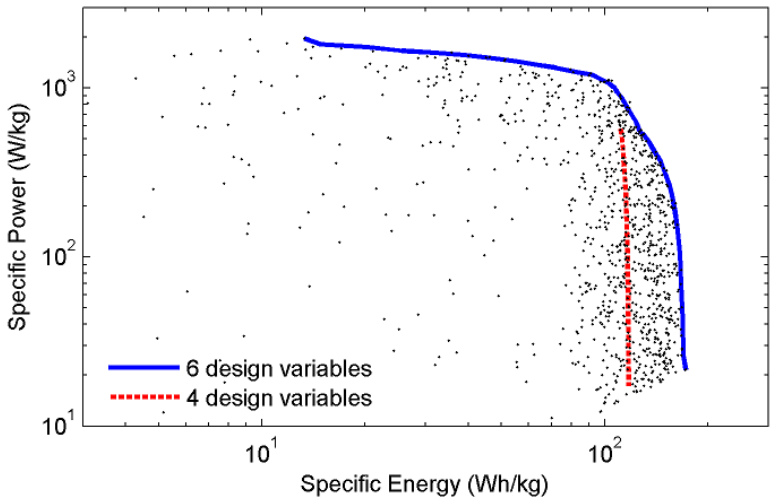

Figure 4-7: Power vs. energy Pareto fronts for 6 design variables (maximum cycling rate of 10C) and 4 design variables (4C)

The gains in energy density resulting from the optimization of electrode thickness and porosity can be quantified by constructing a Pareto front using the same method as in Chapter 3.5. The Pareto fronts plotted in Figure 4-7 show that for a given power level, the cell energy can be improved by up to 40% when the electrode thickness and porosity are optimized compared to when they are fixed as in the problem with 4 design variables. The energy density values for the 4 design variable cases are taken from Figure 3-8 but linearly scaled to account for differences in SOC window. The impact of these optimization results on the aerospace vehicles discussed in Chapter 1.3 can be summarized as follows. Recall that the doubling of energy density is a critical goal that must be met in several of the case studies, including Helios, Solar Impulse, and RQ-11 Raven. The 40% gain from adding just two additional design variables to the problem, with a simplified correction for anode properties based on matching total capacity, represents a significant step towards achieving this goal. Optimization results for an even greater number of design variables, including anode properties, have exhibited further improvements to energy density, up to 230 Wh/kg [78]. Figure 4-7 also shows that the tradeoff between energy and power no longer favors higher power at C-rates above 4C, with very sharp losses in energy density at power densities above about 1000 W/kg. The C-rate corresponding to this power level depends on the values of the electrode thickness and porosity, but is typically between 6C and 8C. The quantification of the relationship

between achievable power and energy is necessary for scaling the cell optimization to a pack-level optimization, as it provides guidelines for distributing the required current load among multiple cells.

4.4 Dimensional Analysis: Parameterization

Having performed a considerable amount of analysis and optimization for a battery cell with spinel lithium manganese oxide ($LiMn_2O_4$) as the cathode material, a logical next step would be to conduct a comparison of different candidate materials, as there are a large number of materials suitable for use in electrodes [101]. Previous studies comparing multiple electrode materials often focus on specific properties such as overcharge behavior [102] or thermal stability [103], and not on the overall cell performance. Rough (zeroth-order) assessments of the cell performance can be made by simply comparing the material properties (mass-specific capacity and electric potential, listed in Table 4-7) of the different materials, as Howard and Spotnitz have done [104], but this type of analysis does not consider the effects of transport coefficients and particle size. Doyle and Newman [105] have used dimensional analysis to derive analytical solutions to characterize battery performance based on operating parameters. Three solutions based on different limiting phenomena were obtained, but a single global analysis without simplified physics is still missing.

Recall that in Chapter 3, a dimensionless time ratio τ^* was introduced to partition the design space. Dimensional analysis entails modeling the output as a function of dimensionless parameters that combine multiple physical variables, and is a widely used technique in fields such as fluid mechanics and heat transfer for characterization and scaling analysis [106], and is especially well suited for problems with similar physical features but widely varying parameter values. In this section, dimensional analysis is extended to define additional dimensionless parameters to characterize the cell performance for multiple cathode materials. In addition to $LiMn_2O_4$, the following cathode materials are considered: lithium iron phosphate ($LiFePO_4$), lithium cobalt oxide ($LiCoO_2$), lithium vanadium oxide (LiV_6O_{13}), and lithium titanium sulfide ($LiTiS_2$). The approach for comparing the materials is as follows:

i. Select a common design of experiments in normalized, dimensionless variables;

ii. Convert the dimensionless design variables to physical variables based on cathode material property ranges obtained from the literature;

iii. Conduct the simulations and define dimensionless parameters to characterize the cell performance.

Table 4-6: Design variable ranges for five cathode materials

Variable	Minimum	Maximum	References
Cycling rate	C/10	10C	
$LiMn_2O_4$			
Particle size	5.0 μm	15 μm	[92]
Diffusivity	1.0×10^{-15} m^2/s	1.0×10^{-12} m^2/s	[107, 108, 109]
Conductivity	1.0×10^{-6} S/m	10 S/m	[110, 95]
$LiFePO_4$			
Particle size	0.02 μm	8.0 μm	[111]
Diffusivity	1.0×10^{-14} m^2/s	1.0×10^{-11} m^2/s	[112, 113]
Conductivity	1.0×10^{-5} S/m	10 S/m	[112, 114]
$LiCoO_2$			
Particle size	0.03 μm	6.0 μm	[115]
Diffusivity	1.6×10^{-17} m^2/s	1.0×10^{-11} m^2/s	[116, 117, 118]
Conductivity	20 S/m	5.0×10^{4} S/m	[119]
LiV_6O_{13}			
Particle size	1.0 μm	25 μm	[120, 121]
Diffusivity	5.0×10^{-13} m^2/s	3.5×10^{-12} m^2/s	[122]
Conductivity	1.0×10^{-3} S/m	1.0×10^{-2} S/m	[122]
$LiTiS_2$			
Particle size	0.1 μm	10 μm	
Diffusivity	4.0×10^{-17} m^2/s	5.6×10^{-13} m^2/s	[123]
Conductivity	5.0 S/m	33.3 S/m	[123, 124]

Table 4-6 lists the particle size, diffusivity, and conductivity ranges considered for each material, along with corresponding references. No literature on the size of $LiTiS_2$ particles is available, so bounds are selected to capture a wide range. Since the variable ranges again span several orders of magnitude in many cases, the logarithmic transformation in Eq. (78) is again applied to convert between the dimensionless variables in the design of experiments and the physical variables. Due to the number of materials considered, constant values for porosity and thickness are used, to simplify the analysis. Since the focus of this work is on comparing cathode materials, the electrolyte (1 M $LiPF_6$ in EC:DMC) and anode material (MCMB graphite) remain the same for each set of analysis. In all cases the inert filler is PVDF, with a density of 1800 kg/m^3. Additional electrode material properties, namely the mass density, specific capacity, and cut-off voltage for the simulations, are listed in Table 4-7. For a consistent comparison among materials, the same SOC window is used: the stoichiometric parameter x in Li_xC_6 ranges between 0.8 and 0.0, while the parameter y in $Li_yMn_2O_4$, etc. range between 0.1 and 1.0.

Table 4-7: Electrode material properties

Material	Density (kg/m^3)	Specific capacity (mAh/g)	Cut-off voltage (V)
$LiMn_2O_4$	4280	148	3.0
$LiFePO_4$	3580	170	3.0
$LiCoO_2$	5010	274	3.0
LiV_6O_{13}	3900	417	1.8
$LiTiS_2$	2285	225	1.6
LiC_6	2260	372	-

A single design of experiments in normalized, dimensionless variables consisting of 1296 points in a LHS arrangement is used for all five cathode materials. As a preliminary step before proceeding directly to dimensional analysis, it is useful to again calculate the global sensitivity indices to check if any critical diffusivity and conductivity values can be identified, since the computational cost of performing the surrogate-based analysis and GSA is negligible compared to conducting the 1296 simulations. A similar

process for identifying these critical values as in Chapter 3.4 is used: the simulation results are sorted according to diffusivity magnitude, and a succession of data sub-sets are compiled for an increasingly narrower diffusivity range by increasing the lower bound. Independent surrogate models are constructed at each stage, and used to compute global sensitivity indices. In this manner, the critical value can be identified when the impact of diffusivity vanishes for a given lower bound. Figure 4-8 shows that for all materials besides lithium titanium sulfide, the effect of diffusivity is dwarfed by either conductivity or cycling rate. For lithium titanium sulfide, however, the effect of diffusivity is significant over the full range, and gradually decreases until becoming negligible at about 2.4×10^{-15} m^2/s. Since diffusivity can be determined as a function of lithium ion concentration [125] and voltage [126], quantifying this critical value establishes a benchmark to aim for when designing or processing materials with similar chemistry. The GSA results also demonstrate that in most cases, adequate cell energy performance can be achieved so long as conditions independent of the diffusivity are satisfied.

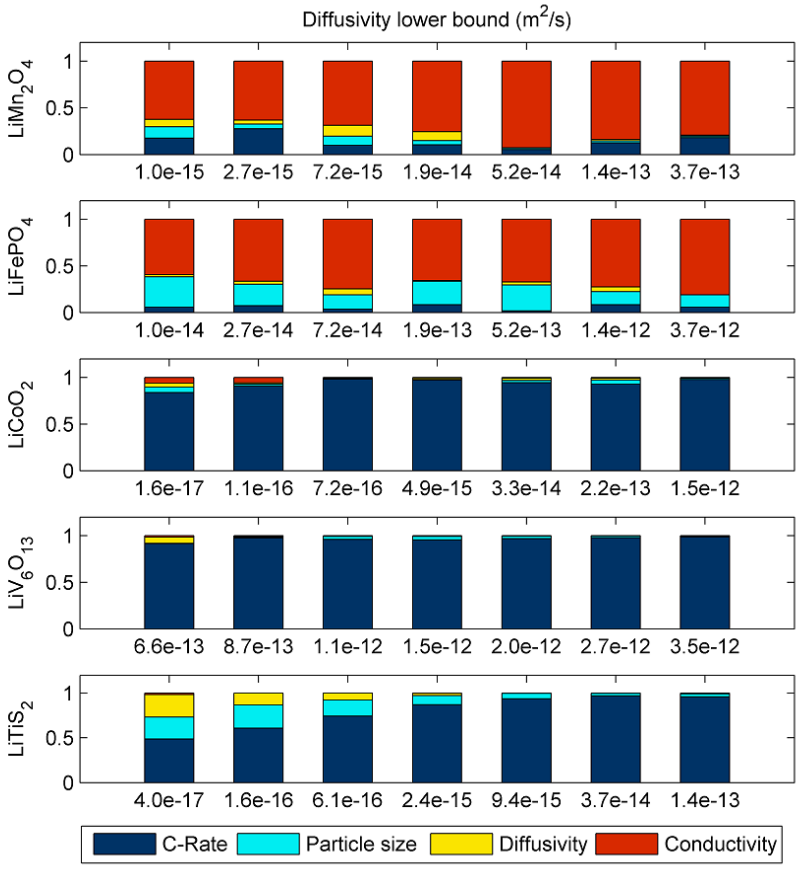

Figure 4-8: Main sensitivity indices for various cathode diffusivity ranges

A similar analysis is performed for conductivity and the results are plotted in Figure 4-9. In the case of lithium cobalt oxide, lithium vanadium oxide, and lithium titanium sulfide, the lower bound for conductivity is sufficiently high to not significantly affect the cell performance. However, for lithium manganese oxide and lithium iron phosphate, conductivity is found to have a strong effect on performance, and critical values of about 0.01 S/m and 0.2 S/m are identified, respectively. Again, quantification of these values can provide guidelines for processing and manufacturing. For instance, these results, in conjunction with recent progress in modeling the influence of additives on conductivity [127], can be used to optimize the amount of conductive additive to introduce to the undoped cathode material.

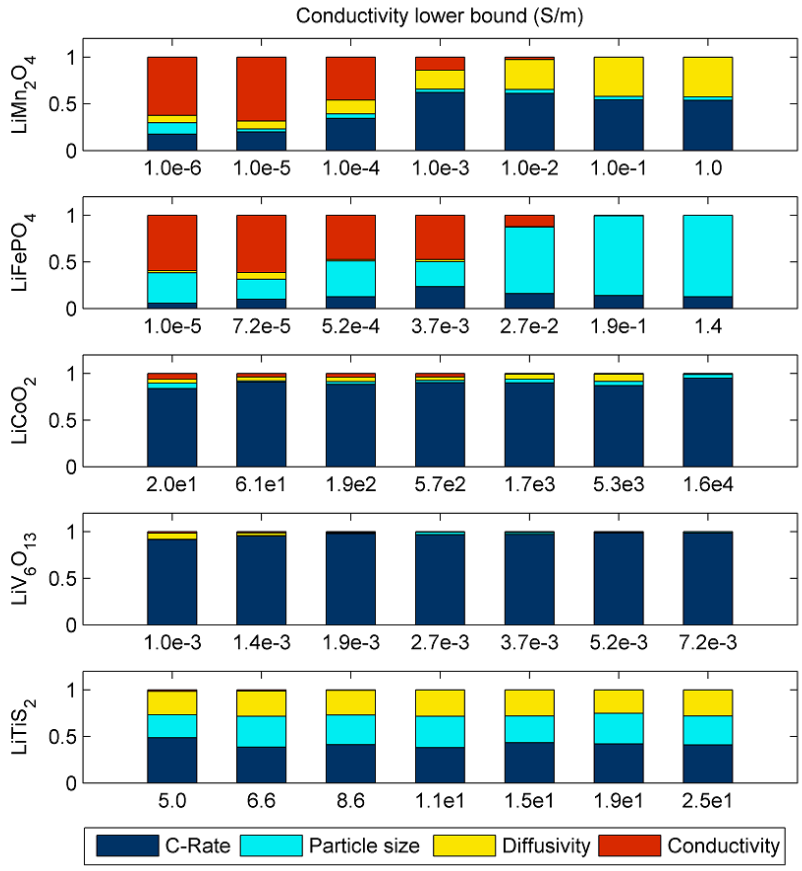

Figure 4-9: Main sensitivity indices for various cathode conductivity ranges

The quantification of critical diffusivity and conductivity values can be further analyzed in the context of dimensionless parameters. For convenience, the dimensionless time parameter τ^* defined in Eq. (77) is presented again:

$$\tau^* = \frac{t_{discharge}}{t_{diffusion}} = \frac{kD_{s,p}}{CR_{s,p}^2} \tag{82}$$

Recall that physically, τ^* represents the relative speed of the diffusion and discharge processes. When the magnitude of τ^* is very large, ions travel much faster through the particle via diffusion than they are transferred across the cell. Conversely, when the magnitude of τ^* is very small, the cell utilization is limited by the diffusion rate. Alternatively, it can be interpreted as a non-dimensionalized version of the solid-phase diffusion coefficient, and will be referred to as "dimensionless diffusivity". Applying this parameter definition to the present problem, a log-scale plot of the computed specific energy against τ^* is shown in Figure 4-10.

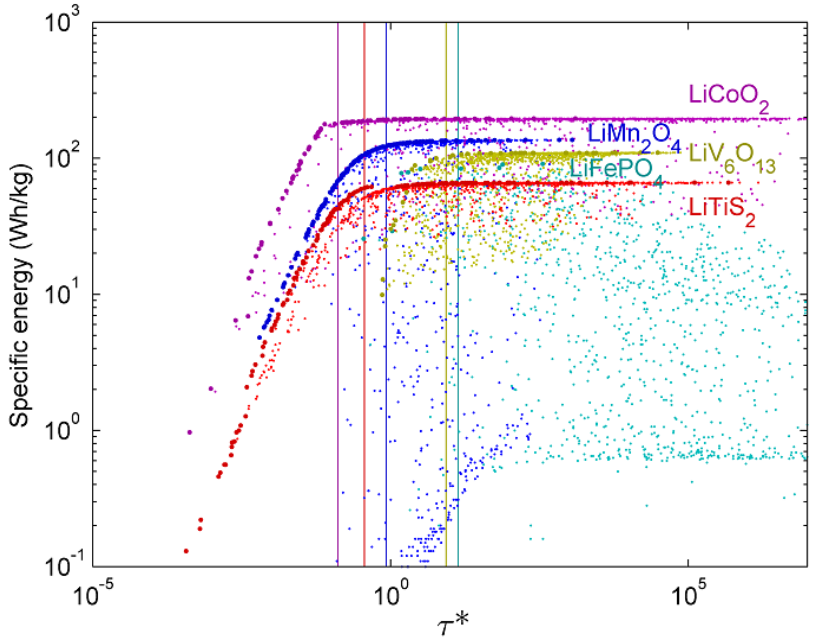

Figure 4-10: Separation of operating regimes based on dimensionless diffusivity

Aside from significant scatter in the data, two distinct regions can be identified: the maximum achievable energy increases monotonically in the low-τ^* range up to some critical point, beyond which it remains roughly constant. Performance in the low-τ^* region is limited by poor ion transport via diffusion causing a depletion of salt in the electrolyte. This can be observed for three of the materials ($LiMn_2O_4$, $LiCoO_2$, and $LiTiS_2$), although the maximum energy levels differ. The boundary between these two operating regimes can be considered a critical point that must be satisfied when conducting cell design. In order to quantify this critical point, consider the Pareto front for each material, formed by defining the following two objectives: maximizing energy and minimizing τ^*. While the majority of the data points, which form the scatter seen in Figure 4-10, are clearly dominated, there remain a set of data points representing the maximum achievable energy density for the corresponding value of τ^*. The critical point can be defined as the minimum value of τ^* such that the (log-scale) slope of the Pareto front becomes less than some tolerance δ:

$$\tau^*_{crit} = \min\left(\tau^*\right) \left| \frac{dy}{dx_1} < \delta \right. \tag{83}$$

$$y \equiv \log_{10} E_{cell} \tag{84}$$

$$x_1 \equiv \log_{10} \tau^* \tag{85}$$

Using the definitions for transforming the specific energy e and the dimensionless time parameter τ^* in Eqs. (84) and (85), respectively, the slope of the Pareto front is estimated using the central-difference scheme:

$$\left.\frac{dy}{dx_1}\right|_{x_{1,n}} \approx \frac{y_{n+1} - y_{n-1}}{x_{1,n+1} - x_{1,n-1}} \tag{86}$$

The critical values of τ^* calculated using these equations are plotted as vertical lines in Figure 4-10. A tolerance value of $\delta = 0.1$ is used for all materials. Recall again that four variables are considered in this study: cycling rate, particle size, diffusivity, and conductivity. The dimensionless diffusivity combines three of these, but note that in Figure 4-10, two materials (LiV_6O_{13} and $LiFePO_4$) do not demonstrate a clear separation of operating regimes based on τ^*. Note that the conductivity has so far been excluded from consideration. Fortunately, it is possible to define a second dimensionless parameter based on conductivity. Since conductivity is the inverse of resistivity, by Ohm's law it has dimensions of electrical current per unit voltage, per unit length. The dimensionless conductivity parameter σ^* can thus be defined as follows:

$$\sigma^* = \frac{\sigma V_{co}}{I_0 L_+} \tag{87}$$

where the reference voltage V_{co} is the cell potential at the end of discharge, the reference current I_0 is the discharge current, and the characteristic length scale L_+ is the electrode thickness. This dimensionless conductivity can be interpreted as a ratio of the material's conductivity to the required conductivity for transporting electrons at the rate dictated by the discharge current. When the magnitude of this ratio is very small, the cell performance can be expected to be limited by conductivity. A plot of specific energy with respect to σ^* in Figure 4-11 shows that two distinct operating regimes can again be identified for some materials, including LiV_6O_{13} and $LiFePO_4$. Referring to the variable bounds listed in Table 4-6, it is easy to note that the lower bounds for these two materials are much higher than for the others. This suggests that within the selected parameter

space, the performance of LiV_6O_{13} and $LiFePO_4$ is limited by conduction but not diffusion. Similarly, Figure 4-11 shows that the relatively high conductivity range for $LiCoO_2$ and $LiTiS_2$ results in little variation in cell performance as σ^* is varied.

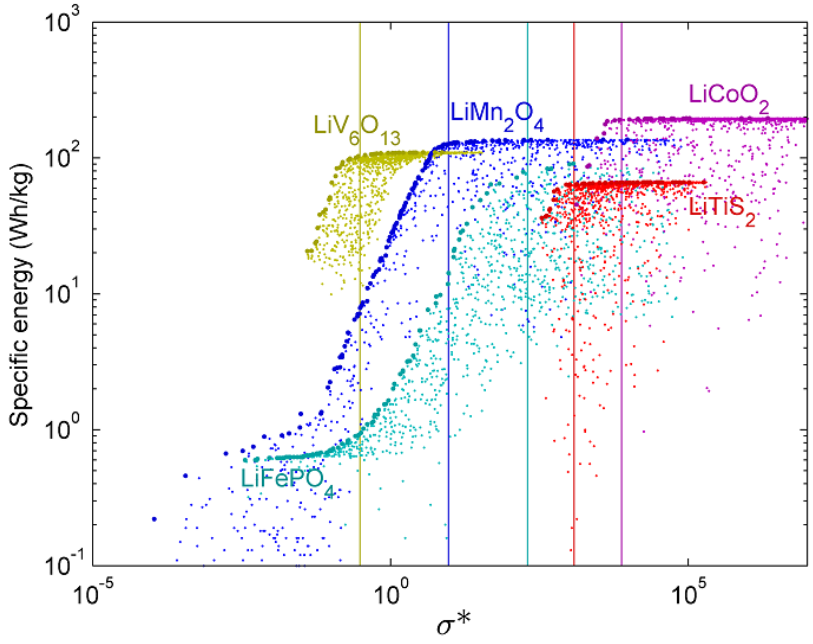

Figure 4-11: Separation of operating regimes based on dimensionless conductivity

As with τ^*, critical values for σ^* are plotted as vertical lines in Figure 4-11, based on a similar definition applied to the set of points in the Pareto front:

$$\sigma^*_{crit} = \min\left(\sigma^*\right) | \frac{dy}{dx_2} < \delta \tag{88}$$

$$x_2 \equiv \log_{10} \sigma^* \tag{89}$$

The same central-difference scheme is used to estimate the derivative, and the same tolerance of $\delta = 0.1$ is used:

$$\left.\frac{dy}{dx_2}\right|_{x_{2,n}} \approx \frac{y_{n+1} - y_{n-1}}{x_{2,n+1} - x_{2,n-1}} \tag{90}$$

4.5 Dimensional Analysis: Energy Function

Having identified two dimensionless parameters that characterize the conditions under which cell performance is limited by diffusivity and conductivity, it is logical to combine them in a way that accounts for the limiting effects of both processes. A simple way to do this is to define a new parameter x^* as base-10 logarithm the lesser of the two dimensionless parameters for each data point:

$$x^* \equiv \log_{10}\left(\min\left[\sigma^*, \tau^*\right]\right) \tag{91}$$

Physically, this can be interpreted as the numerical value corresponding to the most limiting dimensionless transport parameter. Next, consider the Pareto front discussed in section 4.4, which represents the maximum achievable energy performance of a cell for the dimensionless diffusivity and conductivity range. A distinctive shape for the Pareto front has been noted in Figure 4-10 and Figure 4-11, so it is logical to attempt to define this shape using a mathematical curve fit. First, it is a standard practice in dimensional analysis to use entirely dimensionless units, so the energy density is non-dimensionalized:

$$\varepsilon^* = \frac{E_{cell} m_{cell}}{Q V_0 m_{active}} \tag{92}$$

In this case, the energy density of the cell is normalized by the limiting capacity Q, initial cell voltage V_0, and the mass ratio of active to total materials in the cell. Revisiting the notation used in Eqs. (69)-(71), the active mass is equal to the mass of active solid in the cathode and anode:

$$m_{active} = m_{s,+} + m_{s,-} = L_+ \varepsilon_{s,+} \rho_{s,+} + L_- \varepsilon_{s,-} \rho_{s,-} \tag{93}$$

The limiting capacity is defined as the lesser of the two electrode capacities based on the electrode thicknesses and values listed in Table 4-7:

$$Q = \min\left(L_+ \varepsilon_{s,+} \rho_{s,+} q_{s,+}, L_- \varepsilon_{s,-} \rho_{s,-} q_{s,-}\right) \tag{94}$$

A curve fit for characterizing the dimensionless energy function ε^* with respect to the parameter x^* can be obtained using the surrogate modeling techniques described in

Chapter 2.3, but in this case the Pareto fronts exhibit an "S-curve" shape that is better modeled using a class of functions called sigmoid functions, which have asymptotic bounds at their infinite limits. One useful instance of a sigmoid function is the generalized logistic function:

$$\hat{\varepsilon}^* = \frac{k_1}{1 + k_2 e^{-k_3 x^*}} + k_4 \tag{95}$$

This class of functions has been used in growth modeling [128], as its constants govern the shape of the curve in easily identifiable ways. It is readily applicable here as the energy curves shown in Figure 4-10 and Figure 4-11 share similar characteristics. In the limit as x^* approaches negative infinity, the exponential term in the denominator becomes unbounded, and thus the lower asymptote is equal to k_4. In the present battery modeling problem, this corresponds to the limit of zero diffusivity and zero conductivity, in which case no ions or electrons could be transported, and thus no energy could be extracted. Therefore, physical consistency requires that $k_4 = 0$, yielding a simplified form of the generalized logistic function with three constants:

$$\hat{\varepsilon}^* = \frac{k_1}{1 + k_2 e^{-k_3 x^*}} \tag{96}$$

In the infinite limit in the opposite direction, the exponential term vanishes and the function value reaches the upper limit value k_1. The remaining constants k_2 and k_3 govern the growth rate and location of growth, respectively. The three constants are determined by minimizing the curve fit prediction error, defined as the sum of the differences between the exact and approximate dimensionless energy function values given in Eqs. (92) and (96), respectively:

$$\text{error} = \sum_{i=1}^{x_p^*} \left| \varepsilon_i^* - \hat{\varepsilon}_i^* \right| \tag{97}$$

This is implemented using the MATLAB function minimizer `fminunc`, the unconstrained analogue to `fmincon`. Plots of the fitted generalized logistic functions along with the Pareto front for each material are shown in Figure 4-12, and the constants governing their shapes are given in Table 4-8, along with mean prediction errors.

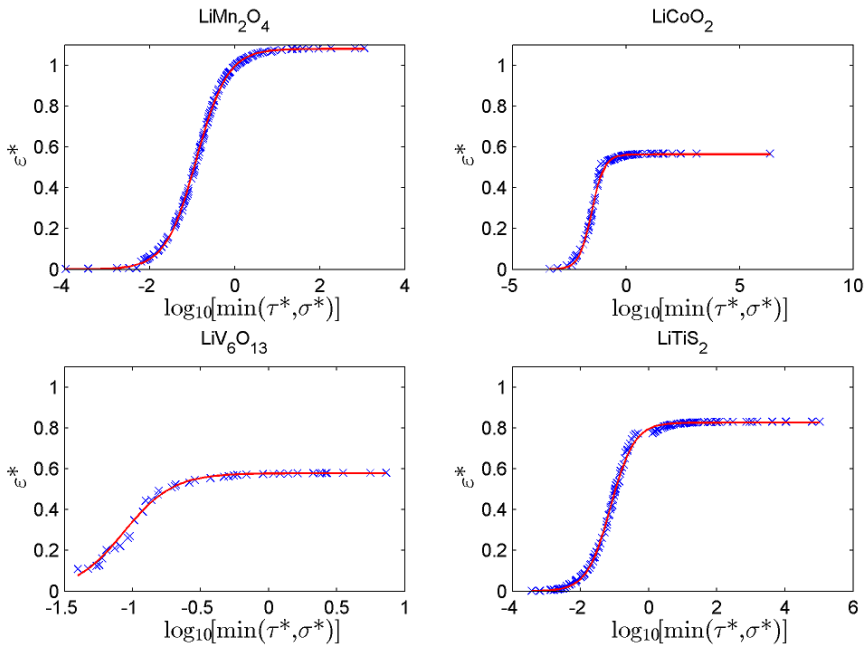

Figure 4-12: Generalized logistic functions fitted for the dimensionless Pareto front of each material

Note that $LiFePO_4$ is not considered in this analysis, as its Pareto front contains an insufficient number of points to conduct a meaningful curve fit or error analysis. However, it is useful to note that for the remaining materials, the generalized logistic function provides an excellent description of the maximum achievable energy performance, with mean prediction errors typically about 1% of the normalized function value or less.

Table 4-8: Mean prediction errors of generalized logistic functions

	$LiMn_2O_4$	$LiCoO_2$	LiV_6O_{13}	$LiTiS_2$
k_1	1.080	0.563	0.578	0.826
k_2	0.0864	0.0045	0.0028	0.0398
k_3	2.737	3.585	5.535	2.887
Mean error	0.0056	0.0084	0.0107	0.0081

The value of this type of analysis can be demonstrated in Figure 4-13, where the maximum energy curve is fit using *n* randomly selected points from the Pareto front for $LiMn_2O_4$, where *n* can be 4, 10, or 24. For each value of *n*, 50 randomly combinations of

data points are selected. When only 4 points are chosen, the curves tend to deviate significantly from the remaining data. However, it is observed that when the number of sampling points is increased to 24, the original curve can be reliably obtained, with all 50 curves closely matching the cell simulation data. These results demonstrate that dimensional analysis can be utilized to significantly reduce the number of total simulations needed to characterize the energy density of the cell. Whereas 1296 simulations were selected in the original DOE, only 24 are needed when proper knowledge of the relationships among dimensionless parameters is established.

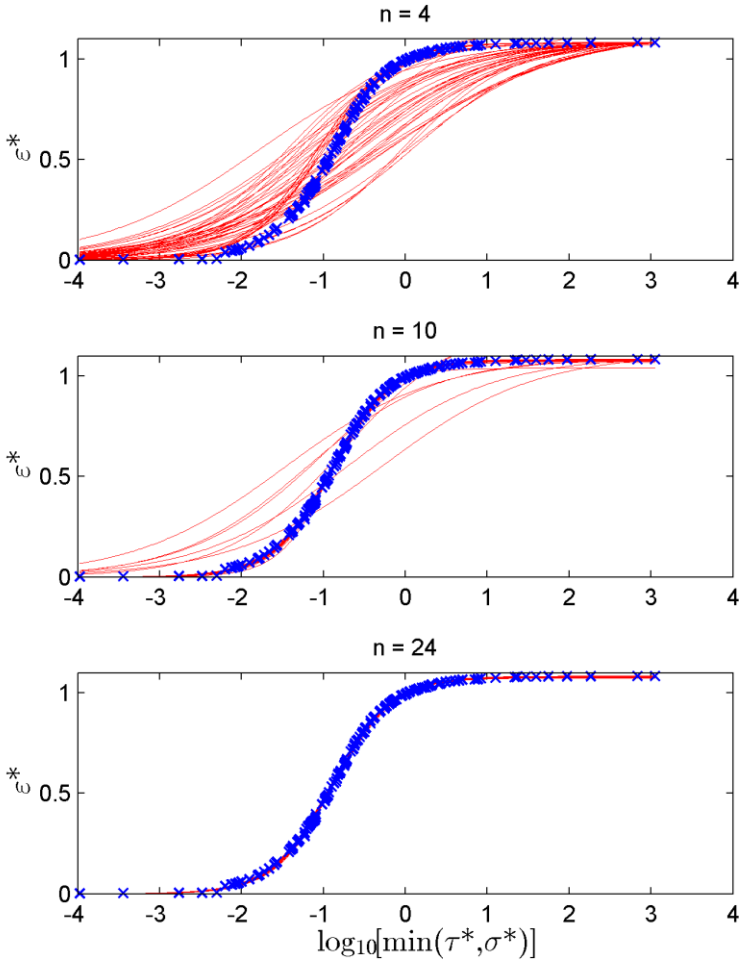

Figure 4-13: Maximum energy curves fitted for 4, 10, and 24 randomly selected points on Pareto front for $LiMn_2O_4$

Finally, it is useful to convert the maximum dimensionless energy (i.e., the k_1 value for each material) to physical quantities to compare these results with theoretical

predictions and experimental measurements. As in Chapters 3.5 and 4.3, the energy density values obtained here are generally lower than reported in the literature; for example, the values of 195.6 Wh/kg for $LiCoO_2$ and 136.3 Wh/kg for $LiMn_2O_4$ are much lower than the respective theoretical limits of 272.1 Wh/kg and 223.2 Wh/kg for jellyroll format batteries [104]. Similarly, the maximum value of 109.8 Wh/kg for LiV_6O_{13} is much lower than the 200-300 Wh/kg estimate for a thin film battery reported by Munshi and Owens [129]. For $LiTiS_2$, the energy density value of 66.2 Wh/kg is within 11% of the 73 Wh/kg reported by Brandt [130]. Again, these discrepancies are due to the use of a limited SOC window and fixed anode properties. Despite these simplifications the relative cell-level energy density values are found to be consistent with the materials' electric potential capacity, given in Table 4-7.

4.6 Summary

The analysis in this chapter provides two significant conceptual contributions: cell design via optimization of configuration and composition (thickness and porosity, respectively) for a given choice of material, and material choice via characterization of material properties using dimensionless diffusivity and conductivity parameters. Generally, the specific energy decreases with higher cycling rates, larger particle size, and lower diffusivity as was found in Chapter 3. The effect of electrode thickness is much more complicated, with an optimal thickness that varies greatly depending on the values of the other design variables. The porosity is found to have a lesser but non-negligible influence on the energy density, and its optimal value also strongly depends on the values of the other parameters. These complicated interactions between design variables illustrate the difficulty of cell optimization, and can help explain why even optimized cells may perform poorly under different operating conditions. The electrode thickness and porosity are optimized simultaneously using a gradient-based optimization method for three distinct physical situations, and the optimal thickness decreases substantially as the diffusivity is decreased and the cycling rate is increased. The proper quantification of the optima also eliminates the need to conduct cell design using overly simplified ad-hoc rules. However, these results also highlight the need to fully understand the system for

which the battery is designed. It is necessary to understand the full range of operating conditions that can be expected for the battery, so that a high-energy cell is not subject to repeated high power rates that will cause not only poor capacity utilization and energy performance, but also significant degradation that will render it unsuitable for automotive and space applications.

A comparison between the optimization results obtained using surrogate-based and gradient-based methods shows that optimizing a surrogate function in lieu of the true objective function yields optimization solutions to within a 5% error margin. Although this is insufficient for many design problems, the ability to perform approximate optimization for a large number of design cases and multiple objectives, as well as constrain the design space via global sensitivity analysis, makes the surrogate method a valuable intermediate step between problem formulation and the final design optimization. Once the most important design cases have been identified, the gradient-based optimizer can be applied directly to the physical model to obtain a much more accurate solution by using exact function and gradient information at each iteration, bypassing surrogate model prediction errors. Within the current modeling framework, the two optimization methods are complementary and can provide accurate optimized solutions for multiple distinct physical scenarios for a reasonable computational cost. The benefits of optimizing the two additional design variables are made clear when the Pareto front for the corresponding optimization problem is compared directly to that from Chapter 3. An increase in energy density is observed at all power density levels, with the greatest gains of 40% in energy density occurring at low power levels. In the context of the aerospace vehicles and systems discussed in Chapter 1.3, this represents a very significant step towards achieving the doubling in energy density required by solar flyers, UAV, and hybrid-electric general aviation aircraft. Further research involving the development of modeling and optimization frameworks for additional design variables such as anode properties and microstructure geometry, coupled with appropriate manufacturing capabilities, are necessary to fully bridge this gap between existing battery performance and the requirements of aerial vehicles.

Despite significant differences in capacity and transport properties, the five cathode materials subject to dimensional analysis exhibit a similar performance

dependence on the two dimensionless parameters defined. Since these two parameters can be interpreted as ratios of transport rates (diffusivity and conductivity) to cell operating conditions (cycling rate and discharge current), these results suggest that regardless of material, ion transport via diffusion and electron transport via conduction are the two most critical limitations to cell performance. The critical points where cell performance becomes independent of the dimensionless parameters are also quantified, and found to be close to unity for all materials. This is again consistent with the physical interpretation that unity represents the point at which all transport rates are balanced with the cell operation. By combining the two dimensionless transport parameters into a single quantity, and non-dimensionalizing the energy density as well, a generalized logistic function is shown to describe the Pareto front well for all materials except $LiFePO_4$, which displays excessive scatter and has an insufficient number of data points in the Pareto front. The generalized logistic function obtained in this study can be considered a type of reduced-order model, in which the maximum energy performance of a cell can be readily estimated with an analytical equation based on the material properties and composition of the electrodes, and the operational parameters of the cell. The methodology documented in this chapter can be readily utilized to analyze the performance of other types of cathode materials, and thus significantly improve the efficiency of the battery design process when multiple choices of materials must be considered. The understanding of relationships between dimensionless variables and energy performance that has been gained can also be used to significantly reduce the number of cell simulations required to properly characterize the performance of a selected electrode material.

For both numerical and practical reasons, limited SOC windows are again considered in both the optimization of the $LiMn_2O_4$ cathode cell and the dimensional analysis of the other cells. As a result, the maximum energy density values reported in this analysis is typically lower than is observed in practical applications. Good data for the open circuit potential are generally not available at very high and very low SOC ranges, and a consistent SOC window is necessary to ensure a consistent comparison between optimization methods and between multiple materials. Despite the generally lower energy density values, the relative performance among different cathode materials

is consistent with their relative voltage and capacity. Additionally, since they are valid for all of the materials considered, the dimensionless relationships established provide useful guidelines for designing new materials with tunable properties. For example, insight into the effect of diffusivity under a wide range of cycling rates established in this study can provide guidelines for material processing to achieve the desired particle size distribution. Similarly, the quantification of critical conductivity levels can help determine the optimal amount of conductive additives to introduce in the manufacturing process [127].

There is also a good practical reason for using a limited SOC range, as well as a higher termination voltage of 3.0 V compared to the 2.0 V in Chapter 3. It is known that cell degradation is greater for a higher depth of discharge (DOD) [38], and the optimization results in this chapter reflect the energy density of batteries designed for long cycle life, such as those found in LEO satellites. The dimensional analysis results are applicable to the vehicles in which poor energy density under non-ideal conditions is of critical concern, like HALE and Solar Impulse, as the configuration of cells within the battery pack can be calculated based on the predicted average and instantaneous power demands of the vehicles, and the known properties contained in the dimensionless parameter definitions.

Chapter 5.
Multi-Scale Modeling of Effective Transport and Electrochemical Kinetics Properties

5.1 Introduction

The physical phenomena in a battery cell occur at very different length scales. These range from mechanical stress and volume expansion at battery module/pack scale, to phase transition, ion dissolution, and fracture at the molecular scale. Even the macroscopic homogeneous model, which ignores molecular-level and pack-level effects, models processes at different length scales such as concentration and potential gradients driving ion transport (electrode/cell scale, $O(10^{-4}$ m)), diffusion and conduction within the microstructure (multi-particle cluster scale, $O(10^{-5}$ m)), and electrochemical reaction kinetics at the solid-liquid interface (single-particle scale, $O(10^{-6}$ m)). Furthermore, while a typical battery cell has thickness of $O(10^{-4}$ m), it can be hundreds or thousands times this size in the other dimensions, and is thus often modeled as an infinite plate. In addition to uncertainty in morphology, a battery is also an inherently multi-physics system, involving electrochemistry, thermodynamics, heat and mass transfer, and structural mechanics. It is clear, therefore, that a high-fidelity simulation of the entire cell is impossible due to geometric and physical complexity.

In this dissertation, a multi-scale modeling approach is used, in which different physical phenomena are modeled at their appropriate length scales and the separate models are then linked to improve upon single-scale models. The macroscopic cell model based on homogenization of the microscopic scale material properties has already been discussed extensively. This chapter documents the development of the microscopic models, as well as the results that are used to build the multi-scale model. A discussion of the relevant numerical issues and the final implementation are also included. The

effective transport and interfacial reaction kinetics results have been presented at the 221st and 222nd Meetings of the Electrochemical Society, respectively [131, 132].

5.2 Microscopic Modeling of Effective Transport Properties

It has been well documented that mass transport via diffusion and conduction through porous media differs from diffusion in a single medium. Much research has attempted to quantify the effective transport properties in porous media using both experimental [79] and analytical/computational approaches [80, 133]. As discussed in Chapter 2.2, the existing macroscopic cell model uses a homogenization approach using Bruggeman's equation, which is based on empirical measurements on simple porous materials such as sand [134]. Although porous in nature, these materials differ from the active electrode matrix, and thus a more accurate model for ion and electron transport within a battery electrode is required. The objective of this section is to apply the physics-based modeling methodology outlined in Chapter 2.5.1 to derive equations for calculating the effective diffusivity and conductivity as a function of porosity.

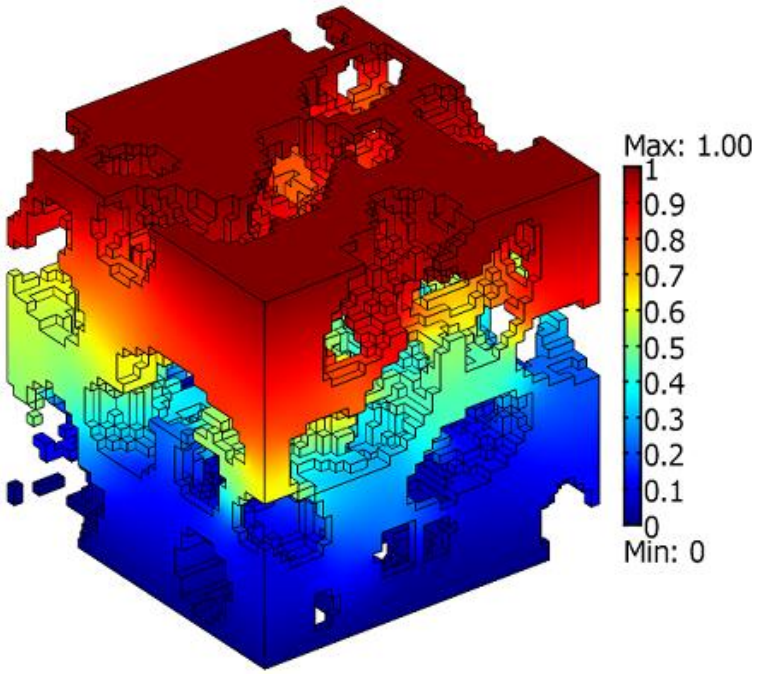

Figure 5-1: Sample ion concentration distribution for 80-particle case; REV dimensions are 20×20×20 µm and mesh resolution is 0.5 µm

The computational cost scales super-linearly with the size of the REV (and thus the number of particles), although the exact scaling relationship is dependent on the choice of solver and preconditioner. For most iterative solvers such as the generalized minimum residual (GMRES) [135], conjugate gradient (CG), and symmetric successive over-relaxation (SSOR) [136] methods, the computational cost scales with $O(n^2)\times O(n^3) = O(n^5)$ for 3-D problems, where n is a one-dimensional length scale such as the REV dimension for a fixed mesh resolution. Meanwhile, the number of particles scales linearly with the number of mesh elements, i.e., $O(n^3)$. Thus, the computational cost is expected to scale approximately by $O(n^{5/3})$ with the number of particles, although within the COMSOL environment it is closer to $O(n^{5/4})$ due to overhead. Various solvers exhibit similar performance, so the conjugate gradient method is used as it is well suited for sparse systems of symmetric, linear equations [137]. An algebraic multigrid method [138] is also used for preconditioning.

Using the automated simulation procedure outlined in Figure 2-3, a total of 2462 REV realization cases are simulated, which includes 2300 with 10 particles (10 μm), 130 with 80 particles (20 μm), and 32 with 640 particles (40 μm). This number of realizations is selected to balance the available computational resources with the need for a large number of realizations to ensure statistically significant averaging of the computed results. To compare the results to the Bruggeman equation used in the macro-homogeneous model, as well as experimental results in the literature, the tortuosity τ is also calculated based on the effective diffusivity and porosity ε:

$$\frac{1}{D^*} = \frac{D^{bulk}}{D^{eff}} = \frac{\tau}{\varepsilon} \tag{98}$$

This equation is commonly used to characterize and analyze battery electrodes, in both experimental and numerical studies [139]. Figure 5-2 compares the porosity-tortuosity relationship in the computed results with the Bruggeman equation, as well as two sets of experimental results by Kehrwald *et al.* [79] and Yu and Carter [140].

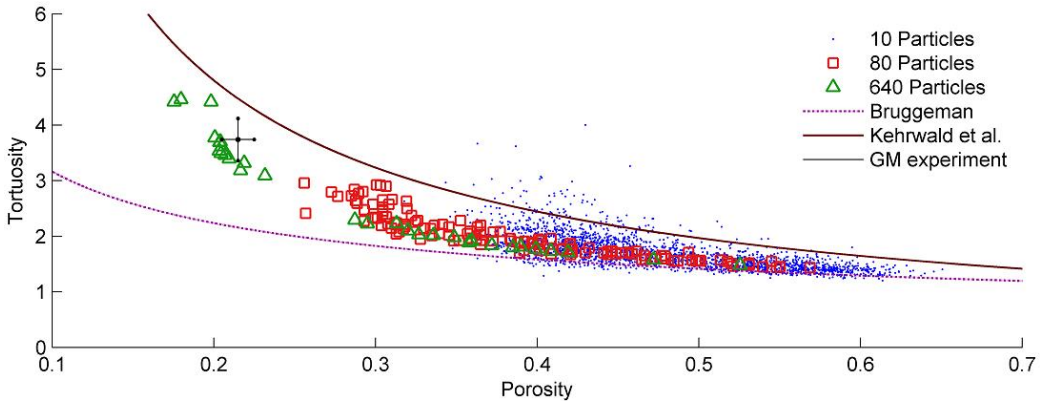

Figure 5-2: Comparison of porosity-tortuosity results for 2462 REV realizations with experiments

Generally, the Bruggeman equation underpredicts the tortuosity, and thus overpredicts the effective diffusivity. The difference between the microstructural simulation results and the Bruggeman equation also becomes greater at low porosity, when the effective transport is most limited. This confirms that the Bruggeman equation tends to overpredict the cell performance when applied to the macro-homogeneous model. The majority of the particle realizations fall in a higher porosity range than the experimental samples, but good agreement in tortuosity is found between simulations and experiments at common porosity levels. There is also good agreement in the porosity-tortuosity relationship between the 80 particle and 640 particle cases, suggesting domain size independence. The simulations tend to predict lower tortuosity than the curve fit proposed Kehrwald *et al.*, which contains significant uncertainty as it is based on only a few measurement samples.

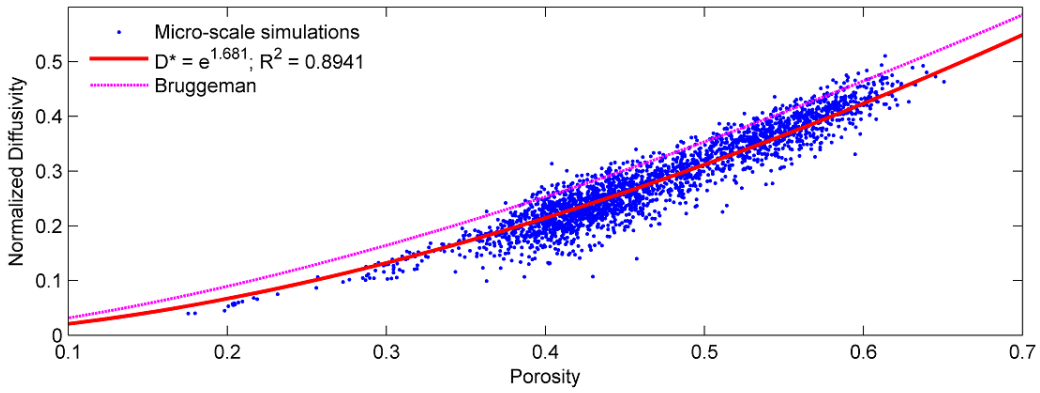

Figure 5-3: Diffusivity-porosity results for 2462 REV realizations, with proposed transport model and Bruggeman equation

The simulation results are plotted in the diffusivity-porosity axes in Figure 5-3, and a proposed value of α = 1.681 is shown to be able to model the effective diffusivity with a coefficient of determination of R^2 = 0.8941. Although this value is lower than for the surrogate modeling studies presented in Chapters 3.3 and 4.2, significant scatter can be expected due to uncertainty stemming from the random nature of the microstructure generation. Note that a power of the same form as the Bruggeman equation is selected rather than any other class of function, as it satisfies two important boundary conditions:

$$D^{eff}\Big|_{\varepsilon=1} = D^{bulk} \tag{99}$$

$$D^{eff}\Big|_{\varepsilon=0} = 0 \tag{100}$$

These two boundary conditions ensure that the effective diffusivity for a single-phase material matches the bulk diffusivity of the material, and that no transport occurs when there is no material available. This modified Bruggeman-type equation presents a significant step towards improving upon the macro-homogeneous model.

5.3 Graph Analysis of Microstructure

The previous section summarizes results obtained from a large number of steady-state FEM diffusion simulations. For each case, the effective diffusivity is computed using a mesh structure depicting the microstructure generated via ellipsoidal packing. As discussed in Chapter 2.5.5, this microstructural information can be readily applied to graph analysis using algorithms based on graph and network theory to relate effective diffusivity to path length parameters in addition to porosity. This is important because in spite of the correction to the Bruggeman model shown in Figure 5-3, significant scatter in the computed diffusivity can be observed for all porosity levels, suggesting a strong dependence on other parameters related to the orientation and alignment of the particles. A proper consideration of these additional factors is necessary to ensure accurate modeling of battery physics during the design process. The first problem to consider is the minimum path problem, which is the identification of the shortest path between two nodes, and the quantification of the length of this path. For a given REV realization, this

problem can be solved by assembling the adjacency matrix corresponding to the voxel mesh structure, and successively computing increasing powers of the matrix until the element of interest becomes non-zero. In this problem, the two nodes can be any combination of nodes in which one node is on the top surface and the other is on the bottom surface (the two opposite ends where the Dirichlet boundary conditions are applied for the diffusion problem). For each additional power of the adjacency matrix that is computed, all matrix elements corresponding to combinations of these nodes are examined, and the computation continues until a non-zero value is found. As discussed in Chapter 2.5.5, computational costs limit the analysis to 10-particle REV realizations, with a graph size of 20×20×20 = 8000 nodes. The following non-dimensional path length parameters are used to normalize the path length L by the REV height δ, which in this case is 10 μm:

$$L^* = \frac{L}{\delta} \tag{101}$$

$$L^*_{\min} = \frac{\min(L)}{\delta} \tag{102}$$

For a perfectly straight diffusion path, this quantity is equal to unity.

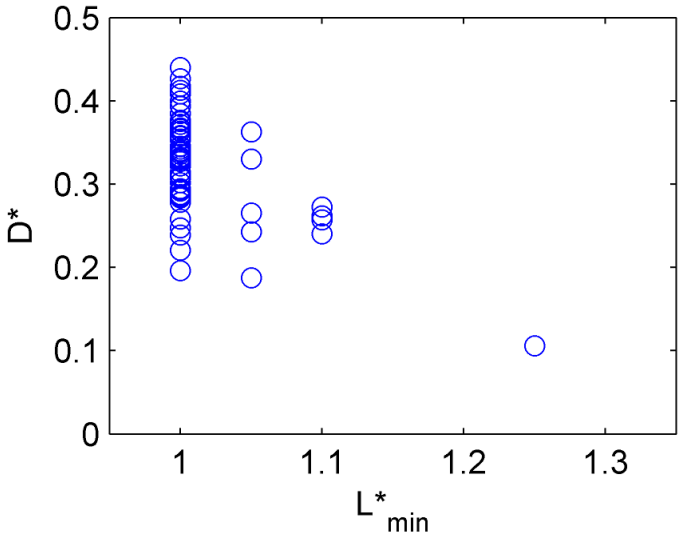

Figure 5-4: Non-dimensional effective diffusivity and path length for 72 REV realizations

Results for 72 randomly selected 10-particle realizations are shown in Figure 5-4. Although a clear trend in which diffusivity decreases with increasing minimum path

length can be observed, a significant amount of scatter is also seen. Note that since the total number of steps in the path length L must be an integer, the non-dimensional path length can also only reflect discrete values. Additionally, the majority of the cases have a unity value, indicating that there exists at least a single diffusion path in most cases that is perfectly straight. As a result, the minimum path problem does not provide a good indicator of the effective transport properties of a given microstructure.

An alternative problem to consider is the quantification of the total number of diffusion paths available. The physical reasoning for this is that a greater number of available paths for the ions allows for a greater diffusion flux across any cross-section in the normal plane, and thus a greater overall diffusion rate. To do this, a non-dimensional path number parameter N^* is defined by normalizing the number of path lengths N by the number of top-bottom node combinations:

$$N^* = \frac{N}{m^4} \tag{103}$$

For an REV realization with m voxel cells in each spatial dimension, there are m^2 nodes in each of the bottom and top surfaces, and thus $m^2 \times m^2$ in total. For the cases presented, $m = 20$. A separate value of N^* can be determined for each path length value L, by computing the matrix A^L and summing the matrix entries corresponding to all top-bottom node combinations. This process is then continued for successively higher powers of the adjacency matrix until the matrix entries corresponding to all top-bottom node combinations are non-zero. This allows every possible pathway for an ion to travel across the microstructure to be counted.

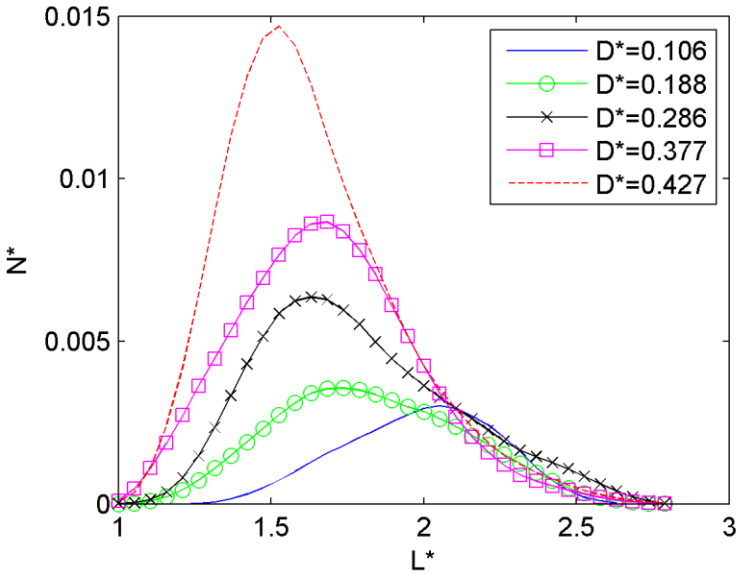

Figure 5-5: Distribution of path lengths for five sample REV realizations

Figure 5-5 contains a plot of N^* against L^*, showing the distribution of path lengths for five realizations with significantly different diffusivity values. It is immediately clear that, as would be expected by physical intuition, diffusivity increases with both a shorter mean path length (L^*), and a greater number of total paths available (N^*). The area under each distribution curve gives the total number of diffusion paths for each case, and this correlates slightly stronger to the effective diffusivity than the porosity does (ρ = 0.602 based on 72 cases, compared to ρ = 0.576 for porosity). However, the area under each curve only accounts for the number of paths, and essentially ignores the path length data exactly. Make use of both the number and length data, a different type of distribution can be plotted, which includes only the shortest path originating from each node in the top layer of the graph. This is accomplished by again computing successively higher powers of the adjacency matrix, and storing the lowest power for which the matrix entry for each top-bottom node pair becomes non-zero. Four realizations are selected to demonstrate the resulting distribution of minimum path lengths, plotted in Figure 5-6.

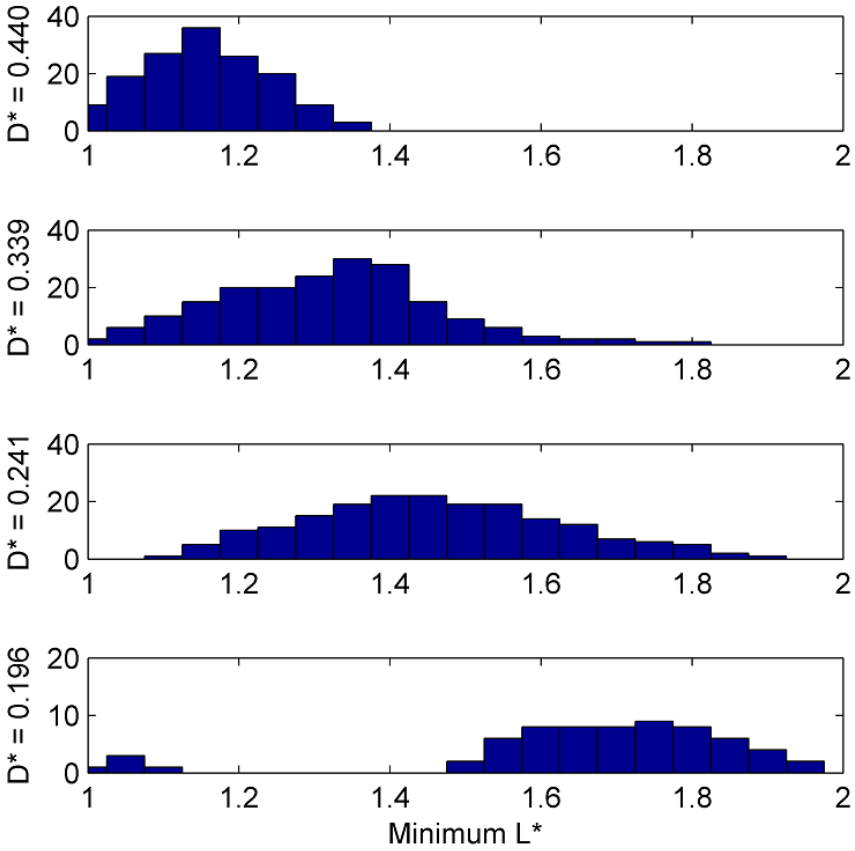

Figure 5-6: Distribution of minimum top-down path lengths for four sample REV realizations

Once again, a clear trend can be observed that the mean value of the minimum path length distribution reduces the overall diffusivity of the microstructure. However, the this mean value is only a slightly stronger correlate than the area underneath the N^*-L^* curve (ρ = -0.654 based on 85 cases). While this parameter is better correlated to effective diffusivity than the porosity is, it is also more difficult to measure experimentally, and to incorporate into the multi-scale model. It is possible to model effective diffusivity as a function of multiple parameters, but this would also introduce an additional layer of uncertainty, and a quadratic regression fit is only able to yield a coefficient of determination of R^2 = 0.444. Therefore, the multi-scale model documented in the following sections does not make use of the parameters defined using graph analysis.

Although none of the path length parameters defined in this section is a sufficiently strong predictor of effective diffusivity to be worth incorporating into the

multi-scale model, they nonetheless provide valuable insight into the physical mechanism of ion transport within the electrode microstructure. Graph analysis can also be a useful technique for better characterizing materials whose microstructures can be visualized and digitalized from experimental samples using techniques such as scanning electron microscopy (SEM) [141]. Recall Chapter 4.4 establishes that diffusion and conduction are the two most limiting physical processes for cell energy density. Therefore, the graph analysis methodology and results presented here can be used to design new high-diffusivity, high-conductivity porous materials with tunable morphology, which may be able to enable the necessary gains in energy density required by electric flyers and UAV.

5.4 Microscopic Modeling of Electrochemical Kinetics at the Interface

As mentioned in Chapter 2.5.2, values for the local ion concentration and electric potential, and their spatial derivatives, are required as boundary conditions for the microscopic simulations. In order to properly map the output of the microscopic simulations (the reaction current density) to the macroscopic state variables, the surrogate modeling framework is again used, with the local ion concentration and electrical potential, and their derivatives, as the "design variables". A design of experiments which models these state variables as independent variables is necessary to ensure that all possible scenarios that may be experienced within the electrode during cell operation are adequately modeled. The corresponding ranges used in the design of experiments are summarized in Table 5-1.

Table 5-1: Ranges of variables used in design of experiments for surrogate modeling of reaction current density

Variable	Symbol	Minimum	Maximum
SOC	c_1	0.2	0.9
Electrolyte Li^+ concentration	c_2	600 mol/m^3	1000 mol/m^3
Solid potential	φ_1	3.0 V	4.15 V
Electrolyte potential	φ_2	-1.0 V	0

SOC gradient	$\frac{\partial c_1}{\partial x}$	-3500 m^{-1}	0
Electrolyte Li^+ concentration gradient	$\frac{\partial c_2}{\partial x}$	-6.5×10^6 mol/m^4	0
Solid potential gradient	$\frac{\partial \varphi_1}{\partial x}$	-40 V/m	0
Electrolyte potential gradient	$\frac{\partial \varphi_2}{\partial x}$	-550 V/m	0

As in Chapter 3, this space is populated with a combined FCCD and LHS sampling approach. However, an additional constraint on the overpotential is applied as a filter:

$$-0.1 \leq \eta \leq 0 \tag{104}$$

This constraint is necessary, to ensure that the exponential terms in the Butler-Volmer equation do not become unbounded. As shown in Figure 5-7, this constraint is not particularly restrictive as it significantly exceeds the operating space within the cathode for a sample discharge, but also serves a secondary purpose of reducing the number of samples required to train the surrogate model, and concentrating more data points within the relevant part of the design space.

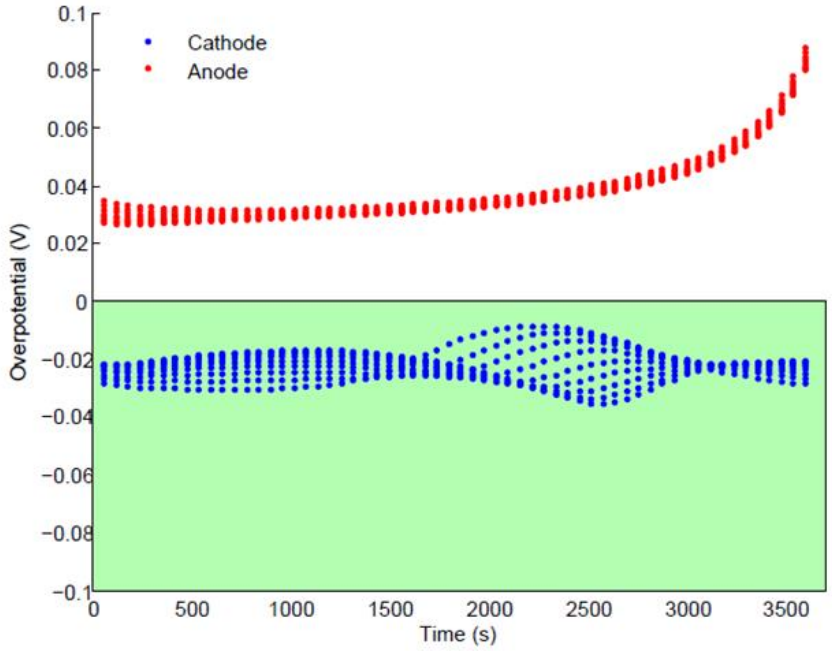

Figure 5-7: Overpotential distribution within anode and cathode during a sample 16 A/m^2 cell discharge, with the constraint space highlighted

The FCCD and LHS sampling of the space within the bounds in Table 5-1, combined with the constraint in Eq. (104), yield a design of experiments of 635 points. This is the set of simulations that are conducted for each REV realization. As in the effective transport simulations, differences in microstructure can cause significant scatter in the results, so an averaging of a statistically meaningful number of realizations is necessary. However, since 635 simulations must be conducted for each realization, a much smaller number of REV can be considered. The computational cost of each simulation is also much greater since a set of four steady-state transport equations must be solved, in addition to a fifth equation at the interface. The results presented in this section are based on the averaging of 18 REV realizations with a solid volume fraction between 0.5995 and 0.6005. Although a general multi-scale model would ideally consider a range of porosity values, realizations with fixed volume fractions are considered here to retain computational feasibility. A sample result for one of the data points from the design of experiments, for one of the REV realizations, is shown in Figure 5-8. Note that, as described in Chapter 2.5.2, the interfacial reaction rate distribution is calculated using Eqs. (58) to (61), applied to the quasi-steady solution of the lithium ion concentration and electric potential in the two phases.

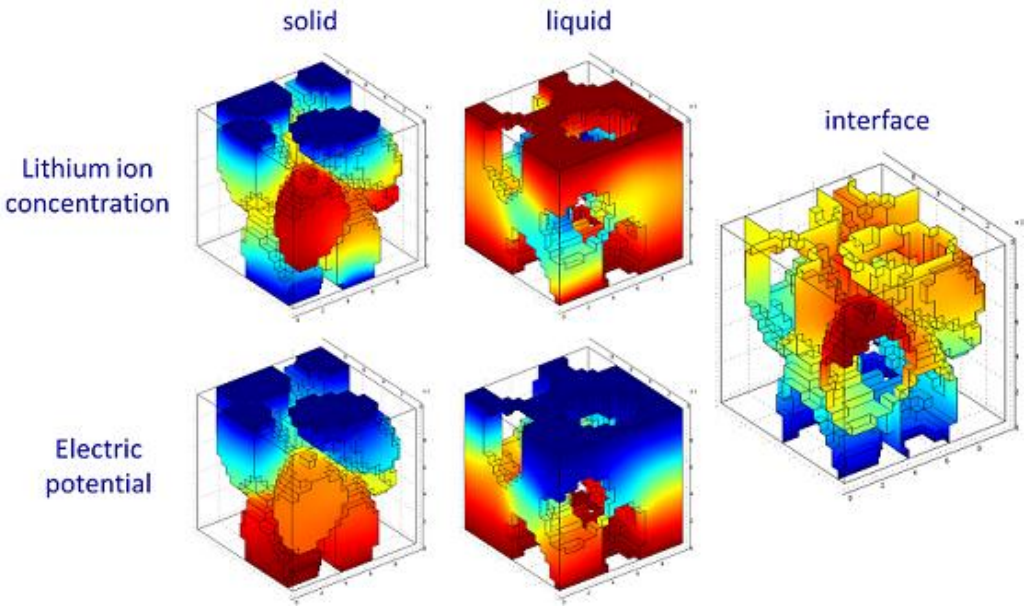

Figure 5-8: Sample interfacial reaction current density simulation result for 10-particle case; REV dimensions are 10×10×10 µm and mesh resolution is 0.5 µm

It is important to note that the 18 realizations have a solid volume fraction centered about 0.6, or a porosity value of 0.4. This is a result of the specific packing density in the MD model, and the overlap factor used in the meshing process. Of course, it would be preferable to build a multi-scale model that spans a wide range of volume fractions, but this would introduce an additional variable to a problem that already has non-trivial computational constraints due to the number of simulations required to populate the large design space, and the number of realizations that must be averaged to account for variation in microstructure. Preliminary results based on a small number of realizations centered at solid volume fraction levels of 0.435, 0.535, and 0.635 suggest little difference in the global sensitivity indices (discussed in the following chapter). In this chapter, a fixed solid volume fraction of 0.6 is used in both the macroscopic and multi-scale cell simulations.

5.5 Comparison of Microscopic and Homogenized Material Properties

A procedure for comparing microscopic simulation results with the homogenized Butler-Volmer reaction kinetics is illustrated in Figure 5-9.

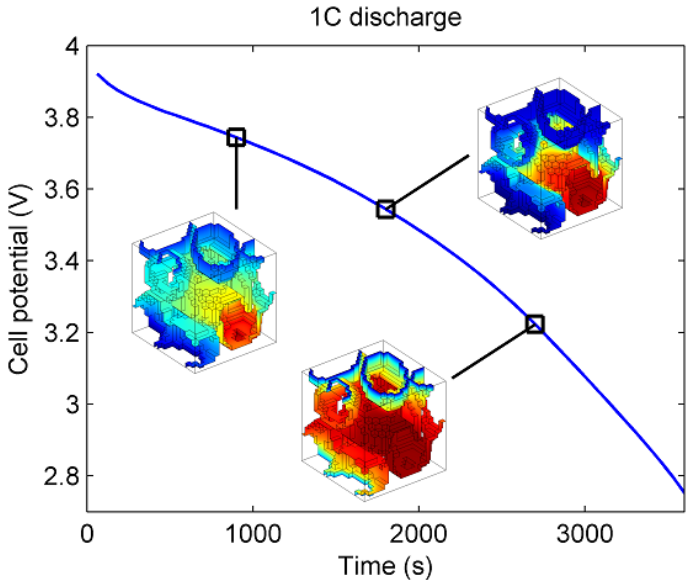

Figure 5-9: Schematic for comparing results from two length scales

A single cell discharge (in this case, at 1C which corresponds to a discharge current density of 16 A/m^2) is performed, and the reaction current density distribution within the cathode is computed at specified time steps. The initial stoichiometric parameters of (x = 0.495, y = 0.2) are used. The solution for all other relevant state variables such as local ion concentration and electric potential in both phases, as well as their spatial derivatives, are also stored. A set of microscopic simulations are then conducted on the same 18 REV realizations from the previous section using the macroscopic state variables as boundary conditions, and the interfacial reaction current density is computed at each sample in time and space. Figure 5-10 compares the averaged results from the 18 realizations with those from the homogenized macroscopic model, at three locations within the cathode for every 60 seconds in a 3600-second cell discharge.

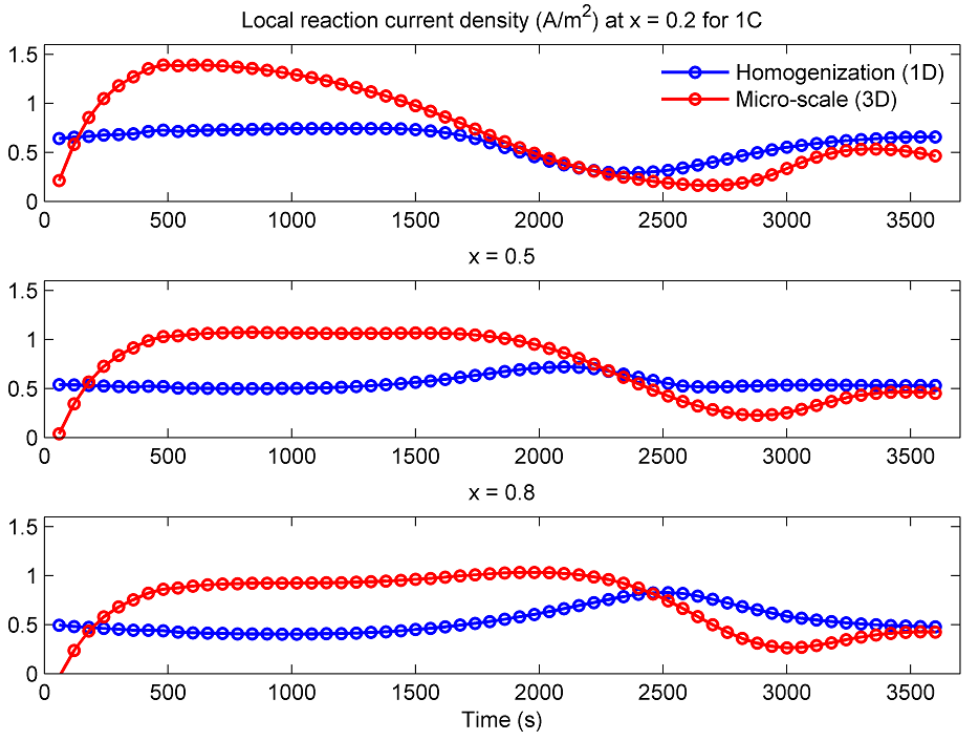

Figure 5-10: Comparison of local reaction kinetics computed using homogenized Butler-Volmer equation and microscopic simulations

A clear difference can be observed between the results from the two length scales, with the microscopic simulations generally exhibiting greater variation than the homogenized equation. Note that the total reaction current integrated over space and time are not equal, because the microscopic simulations are conducted independently of one another and the coupling with the cell model is unidirectional. The surface area is also different, as the macroscopic results are normalized using Eq. (28) while the microscopic results are normalized using the surface area of the interface, based on the meshed geometry. As a result, it appears that the total charge in the electrode is not conserved; however this apparent problem is resolved when the bidirectional coupling of length scales is completed in the multi-scale model.

Since the surrogate modeling framework is used to couple the length scales in the multi-scale model, it is important to assess the performance of the surrogate model. A kriging surrogate is found to have the lowest normalized PRESS value of 7.5%. Previous experience (from Chapters 3.3 and 4.2) indicates that this value is high enough that uncertainty in the surrogate is likely to undo the benefits of the microscopic models. It is

reasonable, then, to again perform global sensitivity analysis to reduce the dimensionality of the surrogate.

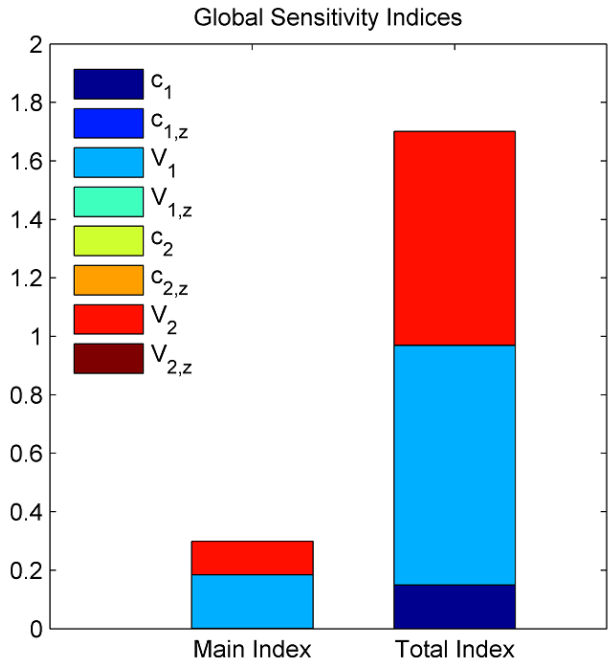

Figure 5-11: Main and total sensitivities for reaction current density surrogate model (8 variables)

Main and total sensitivity indices for the kriging model are plotted in Figure 5-11. It is immediately apparent that the variation in reaction current density is dominated by the magnitude of the two-phase electric potentials φ_1 and φ_2 (or, as denoted in Figure 5-11, V_1 and V_2, respectively), and of the state of charge (c_1). These results are consistent with the findings of Gupta *et al.* [57], who used a similar approach but with different surrogates, and a different design of experiments and choice of REV realizations. The dominant effect of the electric potentials can perhaps be explained by the functional form of the Butler-Volmer equation, in which the overpotential is embedded in the exponential terms while the ion concentration appears in the polynomial terms. Note that all four gradient terms are found to have negligible impact, a result that can be explained by the bounds in Table 5-1, and by the application of boundary conditions shown in Eqs. (56) and (57). The magnitude of the difference between the boundary conditions tends to be much less than the mean value within the REV, which has dimension $L = 10\times10^{-6} = 10^{-5}$ m. For example, the SOC variation across the REV due to the spatial gradient is at most $3500\times10^{-5} = 0.035$ V, which is 5% of the SOC range being modeled in the design of

experiments. The results in Figure 5-11 allow the surrogate model to be reduced from 8 to 3 design variables, and as in Chapter 4.2.2, the reduction in the number of independent variables also improves the accuracy of the surrogate model in this case, reducing the PRESS value from 7.5% to 3.9%. To assess its accuracy, the surrogate model is used to evaluate the reaction current density at the same points as in Figure 5-10, and the results are plotted in Figure 5-12 with the averaged microscopic values.

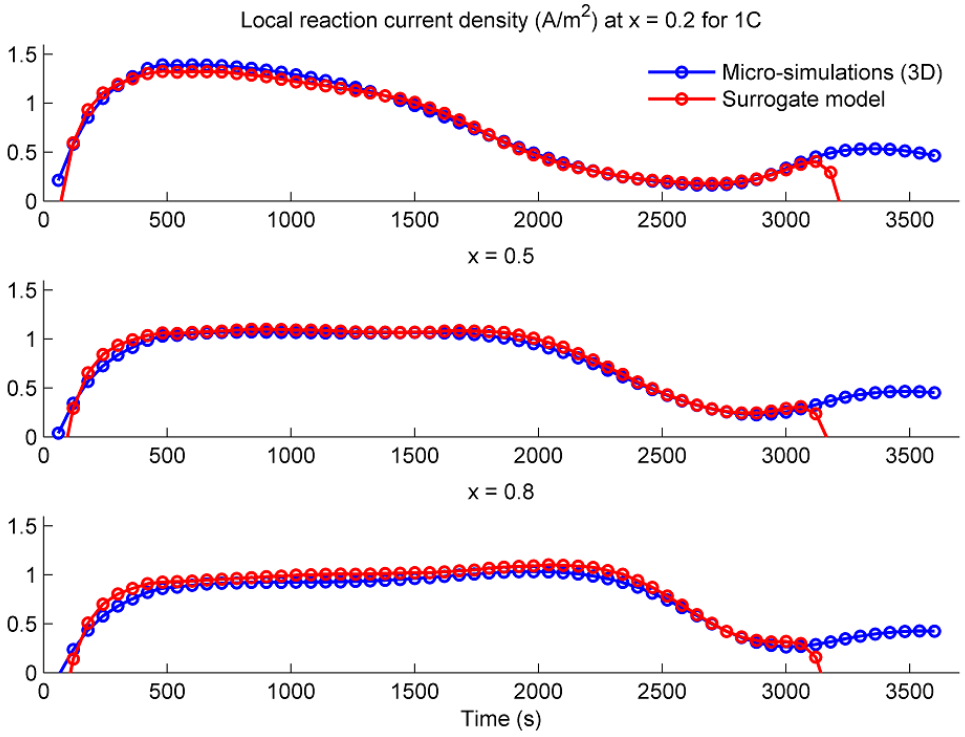

Figure 5-12: Local reaction kinetics computed for using microscopic simulations, and predicted by kriging surrogate with 3 variables

The surrogate model matches the microscopic simulations very well until about t = 3100 seconds. It is unclear why the surrogate model suddenly deviates at this point, as the overpotential constraint in Eq. (104) is not violated. Regardless, the accuracy of the surrogate model in the first 3100 seconds is sufficient to proceed with coupling the length scales to complete the multi-scale model.

5.6 Multi-Scale Modeling with Surrogate-Based Coupling

It has been established that a high-fidelity simulation of the entire cell is

impossible due to physical and geometric complexity, and that a multi-scale modeling approach is needed. Multi-scale modeling refers to a class of modeling techniques that involve coupling the features of individual models from different length scales, and comprises a variety of different conceptual strategies and implementations. Several multi-scale models have been developed to analyze battery and cell performance with respect to various physical phenomena. For example, Golmon *et al.* [142] have coupled the `dualfoil` macroscopic model with the electrochemical-mechanical stress model of Zhang *et al.* [39], using homogenization based on Mori-Tanaka effective field theory [143]. A subsequent study combined this multi-scale model with adjoint sensitivity analysis to optimize the porosity and particle size distribution within electrodes [144]. Another multi-scale model, developed by Xiao *et al.*, has been used to study intercalation-induced and mechanical stress on separators, using a fixed 2-D representative volume element [145]. Various other approaches have been used in the multi-scale modeling of batteries [146, 147], as well as other engineering systems such as composite materials [148]. Recently, Franco has compiled a comprehensive review of advances in the multi-scale modeling of lithium ion batteries [149].

The approach adopted in this dissertation is to use create surrogate models based on the pre-computed 3-D simulations summarized in Chapters 5.2 and 5.4, which are then used to bridge the gap in the macroscopic homogeneous model. This approach differs from other multi-scale models in that the state variables are not explicitly coupled, but rather implicitly coupled via the surrogate presented in Chapter 5.5. The advantage of this method is that the computational cost of evaluating the surrogate function is negligible compared to the cost of conducting full 3-D simulations, and thus the computational cost of conducting a multi-scale cell simulation can be almost equal to that of the macro-homogeneous model. However, the disadvantages of this approach include quantifying the error due to uncertainty in fitting the surrogate model, as well as some numerical issues related to the robustness of the surrogate bridge. Robustness is an especially important consideration in models used for design, as they must be capable of handling large perturbations to a large number of design variables. The following sections examine these numerical issues for the multi-scale model.

5.6.1 Numerical Issues: Derivative Definition and Robustness

The open circuit voltage in Eq. (29) differs from that used in the COMSOL implementation of the cell model, which uses COMSOL's own interpolation functions to generate a cubic curve fit on 42 discrete sampling points. In Figure 5-13, the two OCV curves follow a similar shape and have very similar magnitude, suggesting little difference in their influence on the electrode state variables and cell performance. However, this difference in fact leads to some interesting mathematical properties.

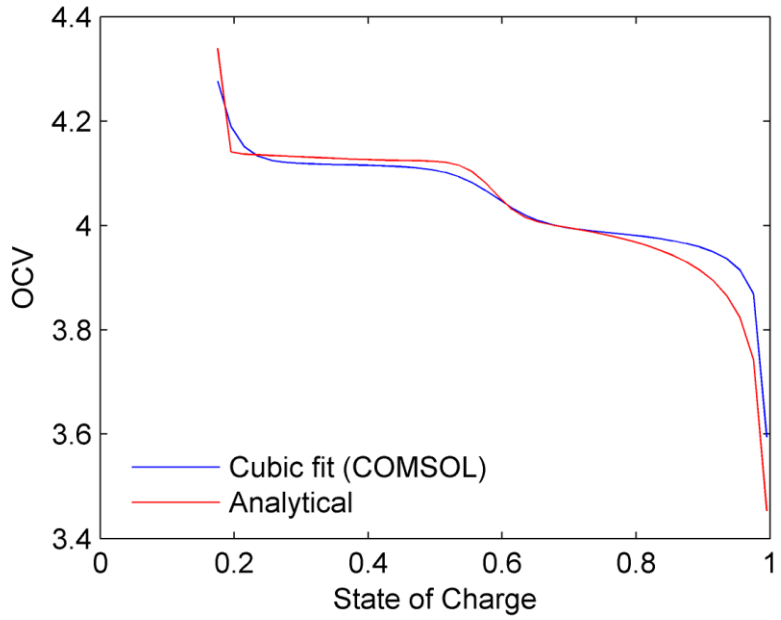

Figure 5-13: $LiMn_2O_4$ open circuit voltage curves for analytical equation (dualfoil) and cubic curve fit (COMSOL)

The Butler-Volmer equation used to model the interfacial electrochemical reaction kinetics originally shown in Eq. (26), is presented again for convenience:

$$j_{flux} = \frac{J}{a_{s,p}} = i_0 \left[\exp(k\eta) - \exp(-k\eta) \right] \tag{105}$$

$$k = \frac{\alpha F}{RT} \tag{106}$$

Note that the normalized reaction current density j_{flux} does not depend explicitly on the state of charge or the open circuit voltage, but rather the overpotential. The overpotential supplies the necessary energy to overcome the thermodynamic barrier to

allow the electrochemical reaction to occur, and as shown in Eq. (28), is defined in terms of a potential difference between the cell and the open circuit voltage. During the discharge of the cell, the values of the electric potentials φ_1 and φ_2 are typically such that the overpotential is close to zero. This can also be seen in the design of experiments constraint in Eq. (104). Consequently, the small difference in OCV observed in Figure 5-13 actually leads to significant differences in the overpotential, and thus reaction current density distributions within the electrode.

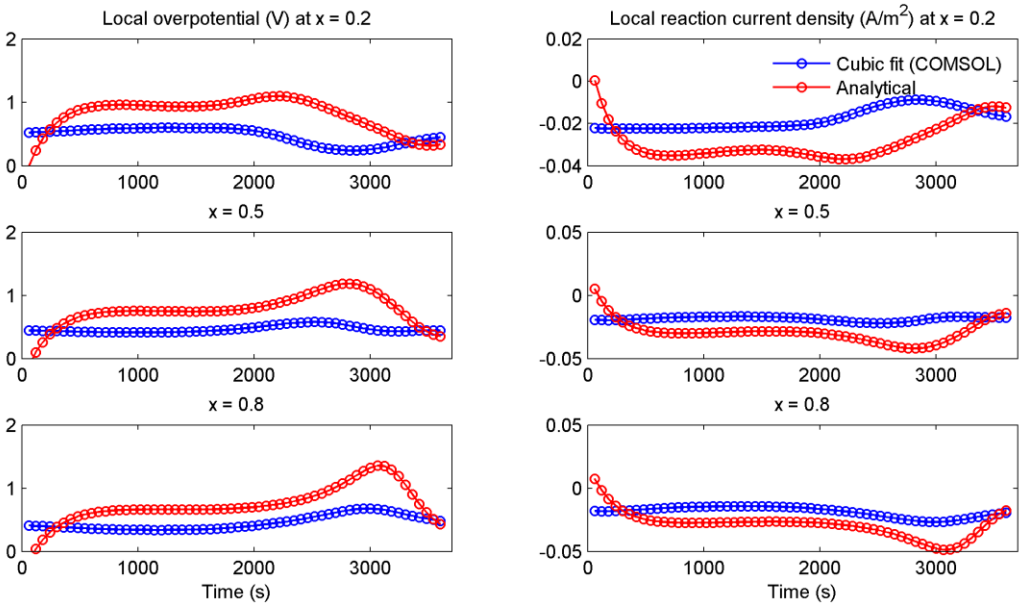

Figure 5-14: Local overpotential (left) and reaction current density (right) at three locations within the cathode, based on analytical (dualfoil) and cubic fit (COMSOL) open circuit voltage curves

This can be seen in Figure 5-14, which plots the overpotential and reaction current density within the electrode for a single cell discharge simulation. The cubic curve fit implemented in COMSOL has a slightly smaller potential difference between the two open circuit plateaus, and thus less overall variation in the cell state variables. It is interesting to note then, that despite the differences in reaction current density distribution and overpotential, Figure 5-15 shows very little difference in the discharge curve, and thus the total energy density. One explanation for this cell voltage insensitivity is that when the system of equations is closed, the total amount of charge being transferred at the interface (the local reaction current density integrated over the entire electrode) balances the discharge current of the cell. The total amount of charge being

transferred has a greater effect on the cell performance than the distribution of this charge within the electrode.

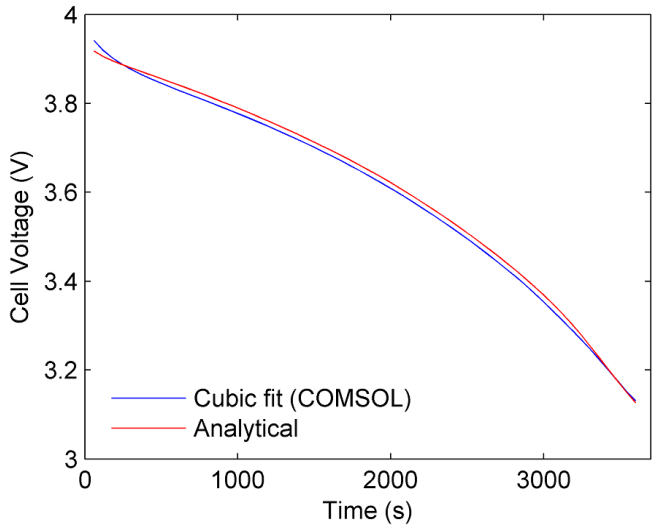

Figure 5-15: Cell voltage for analytical equation (dualfoil) and cubic curve fit (COMSOL)

For consistency with the macroscopic model, the analytically defined open circuit voltage in Eq. (29) is used in the multi-scale model implementation. An additional benefit is that its derivatives can be calculated exactly and do not require numerical approximations. This problem is prominently observed when attempting to build a multi-scale model using non-smooth functions to couple the length scales. Specifically, although COMSOL is capable of handling the analytical Butler-Volmer function, the surrogate- or interpolation-based functions are problematic due to the derivative definition. As a test, a random perturbation is introduced:

$$\hat{j}_{flux} = (1 + Ab) i_0 \left[\exp(k\eta) - \exp(-k\eta) \right] \tag{107}$$

A full cell simulation is then conducted to check for numerical instability or divergence. Note that the analytic gradients based on the standard Butler-Volmer equation (106) is still used by the numerical solver. In Eq. (107), A is the perturbation amplitude, fixed at a constant value for the simulation, and b is a random number in the range [-0.5,0.5] generated each time the function is called. This ensures an unbiased perturbation with each iteration and time step. Figure 5-16 plots the reaction current density time history at a fixed location x = 0.5 for a single discharge simulation. It can be

seen that while the analytical gradient might be sufficient when the perturbation amplitude is small (A = 0.3), for large perturbations the reaction current function becomes highly discontinuous and convergence problems can be expected.

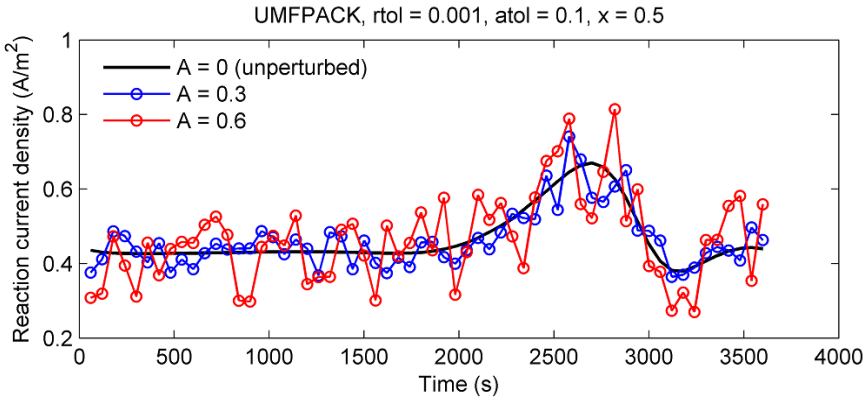

Figure 5-16: Reaction current density based on perturbed Butler-Volmer function

This can be confirmed by examining the effect of perturbation amplitude on the CPU time required to conduct a single cell discharge simulation. It can be observed in Figure 5-17 that the computational cost can increase significantly with larger perturbations, regardless of the numerical solver used. Note that other solvers such as symmetric successive over-relaxation (SSOR) and conjugate gradient (CG) are ill-suited for this problem, and thus not considered.

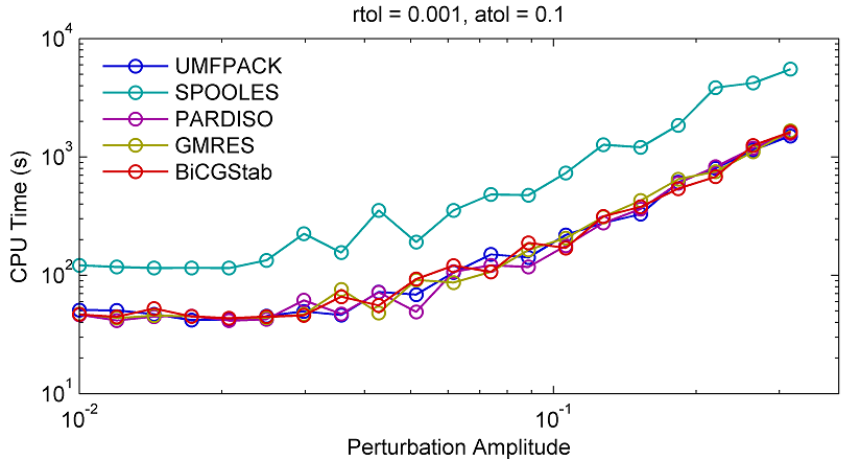

Figure 5-17: Computational time for a single cell simulation using perturbed Butler-Volmer reaction model, for direct and iterative solvers

Thus, it is established that the definition of the gradient is of critical importance to the robustness and efficiency of the multi-scale model. This restricts the classes of

functions that can be used to couple the macroscopic and microscopic models: the MATLAB and COMSOL native interpolation functions lack explicitly defined gradients, and finite-difference approximations are insufficient due to their limited robustness. Although the classes of surrogate models discussed in Chapters 2.3 and 3.3 are smooth, it is difficult and tedious to extract their exact gradients. The logical choice, therefore, is a PRS surrogate, which has an explicitly defined, smooth gradient.

5.6.2 Surrogate-Based Coupling of Length Scales

A 4th-order PRS with two input variables (SOC and overpotential) of the following form yields a coefficient of determination of $R^2 = 0.9486$:

$$\begin{aligned}\hat{j}_{flux} &= k_1 + k_2 c_1 + k_3 \eta + k_4 c_1^2 + k_5 c_1 \eta + k_6 \eta^2 \\ &+ k_7 c_1^3 + k_8 c_1^2 \eta + k_9 c_1 \eta^2 + k_{10} \eta^3 + k_{11} c_1^4 \\ &+ k_{12} c_1^3 \eta + k_{13} c_1^2 \eta^2 + k_{14} c_1 \eta^3 + k_{15} \eta^4\end{aligned} \tag{108}$$

The coefficients $k_1 \ldots k_{15}$ are contained in Table 5-2.

Table 5-2: Polynomial coefficients of reaction current density surrogate

k_1	10.39	k_6	14.90	k_{11}	138.7
k_2	-87.43	k_7	-316.2	k_{12}	270.6
k_3	89.41	k_8	478.5	k_{13}	580.5
k_4	257.0	k_9	678.9	k_{14}	363.6
k_5	-298.4	k_{10}	28656	k_{15}	16256

Although there are a sufficient number of data points to fit higher order PRS functions with higher coefficients of determination (5th-order gives $R^2 = 0.9590$, 6th-order $R^2 = 0.9742$), the number of polynomial terms increases dramatically, making the definition of analytical derivatives a very tedious process. Therefore, the multi-scale model in subsequent analysis uses the 4th-order PRS. An assessment of the surrogate model accuracy can be made by comparing the local reaction current density profiles predicted by the PRS and the 3-D microscopic simulations.

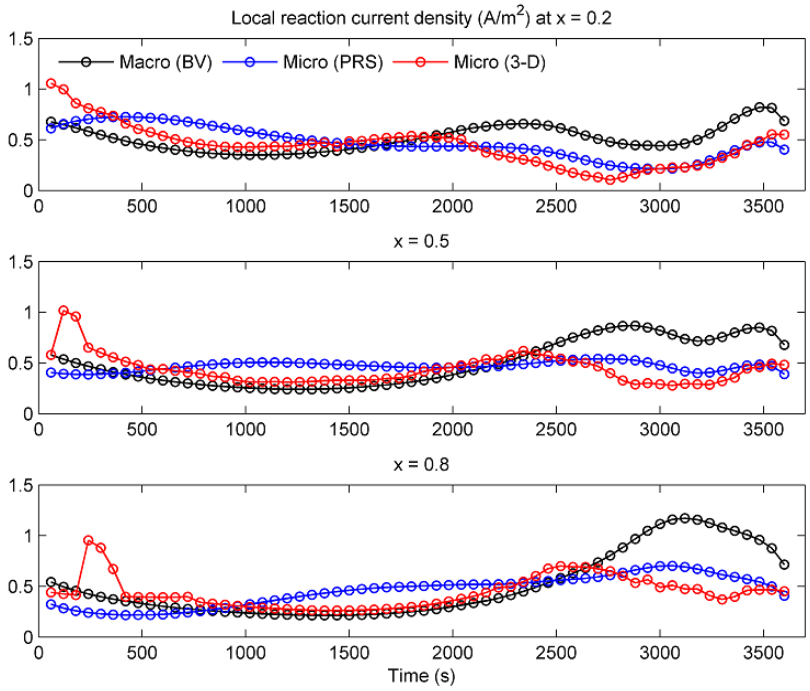

Figure 5-18: Local reaction kinetics predicted at three locations by the Butler-Volmer equation, linear interpolation of microstructural simulations, and PRS surrogate

As shown in Figure 5-18, the surrogate follows a similar profile to the microscopic simulations, but some differences can be observed. Moreover, it has already been observed in Figure 5-12 that a kriging model is able to match the microscopic simulations much better than the PRS. This suggests a need to further refine the surrogate model, which, given the computational cost of conducting the 3-D simulations, would require additional computational resources. In the meantime, the PRS is used to successfully bridge the scale gap to complete the multi-scale model.

5.6.3 Multi-Scale Analysis of Cell Performance

A comparison of the discharge curves obtained using the multi-scale and macroscopic models is shown in Figure 5-19.

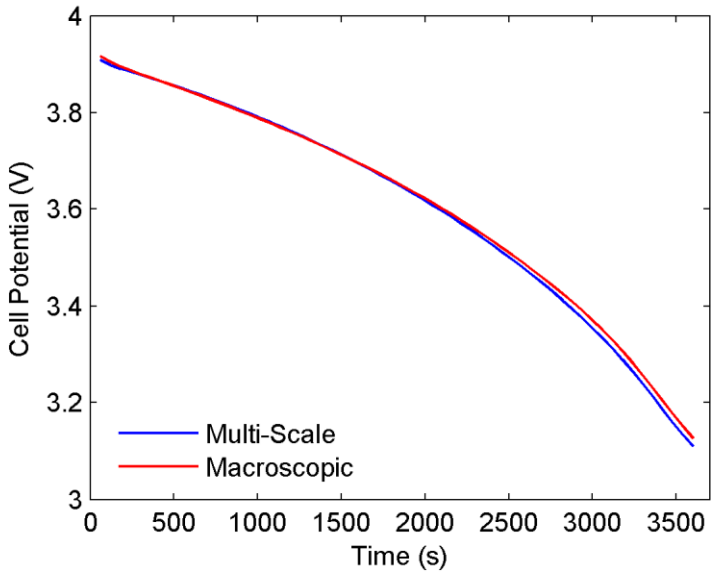

Figure 5-19: Comparison of multi-scale and macroscopic simulation results for a single discharge

The cell performance is not very sensitive to the electrochemical kinetic profile, as a similar discharge curve is obtained despite noticeable differences observed between the macroscopic and multi-scale models. This suggests that the electrochemical reaction rate performs much like diffusion and conduction, in that it limits overall cell performance at low levels, but has little influence beyond some critical threshold value. The effect of low electrochemical reaction rate being an important performance barrier has been documented, for example by Yonemura *et al.* as a reason for $LiMnPO_4$ being an unsuitable cathode material [150]. To confirm this similarity to diffusion and conduction, it is necessary to examine the operating regime for these cases, as was done in Chapter 4.4. To do this, the Butler-Volmer equation can be scaled by a constant factor *k*:

$$\hat{j}_{flux} = ki_0\left[\exp(k\eta) - \exp(-k\eta)\right] \tag{109}$$

By artificially tuning *k*, the influence of electrochemical reaction kinetics on the cell performance can be modeled. Note that the macroscopic Butler-Volmer equation is used here as it is much more robust over a wide range of *k* values, but similar results can be obtained using the multi-scale surrogate equation. The influence of *k* on the cell voltage and reaction current density at a fixed point (x = 0.2) within the cathode are shown in Figure 5-20.

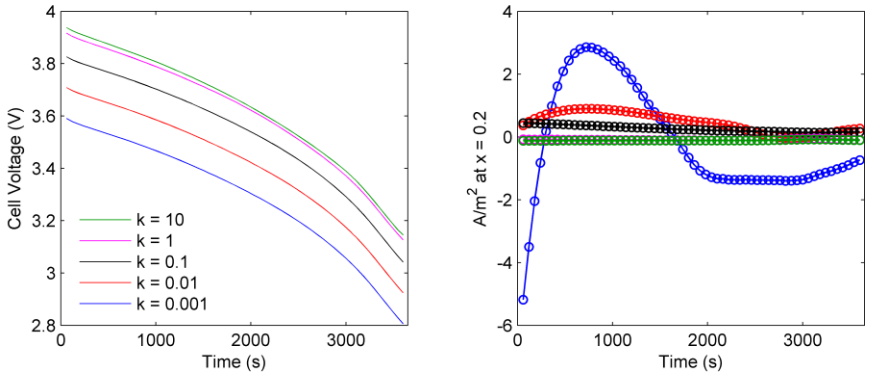

Figure 5-20: Cell voltage and reaction current density for perturbed Butler-Volmer interfacial kinetics

As *k* is decreased by orders of magnitude, the cell voltage noticeably drops due to greater internal resistance within the cell. This results in a loss in both power and energy based on Eqs. (1) and (2), as well as a further loss in energy since the cutoff voltage is reached sooner, leading to premature termination of the discharge. Large oscillations in the local reaction current density are also observed for low *k*, another highly undesirable effect as this would lead to increased heat generation and stress, which accelerate the degradation of the cell. However, a comparison of the $k = 1$ and $k = 10$ curves shows very little difference in both cell voltage and local reaction current density, indicating that in the $k = 1$ case, which corresponds to the cell under standard operating conditions, the electrochemical reaction at the interface proceeds is sufficiently quick to act as a buffer against small perturbations. The lowest value $k = 0.001$ plotted in Figure 5-20 is close to the minimum possible value of *k*, as the equations become too stiff below this threshold and the numerical solver is unable to converge.

It may appear that the insensitivity of the overall cell performance to the electrochemical reaction model used at the interface should call into question the value of developing the multi-scale model. After all, if the Butler-Volmer equation used in the macro-homogeneous model is able to deliver almost the same cell performance prediction as the multi-scale model, it may seem that the multi-scale model provides very limited additional value. However, it is important to note that prior to obtaining these results, this insensitivity had not been previously established. Meanwhile, it had been established that the reaction current density distribution is very sensitive to several design and state variables. Therefore, the documentation of the comparison between the

macroscopic, microscopic, and multi-scale models, the exploration of numerical issues such as robustness and convergence rate, and the quantification of the sensitivity of the cell performance to perturbations in the Butler-Volmer equation, are all very meaningful contributions enabled by the multi-scale model.

5.7 Summary

This chapter documents the establishment of a multi-scale model for analyzing cell performance, which combines the computational efficiency of the macro-homogeneous models employed in previous chapters with detailed physics-based microscopic models for important material properties. Namely, the material properties modeled using microscopic models are the effective transport coefficients in the diffusion and electric potential equations in the axial dimension of the macro-homogeneous model, and the volumetric electrochemical reaction term that couples the axial and radial length scales. Effective transport coefficient results obtained from 2462 REV realization cases are presented show that the Bruggeman equation used in the homogenized models consistently underpredicts the tortuosity in the porous medium, and thus overpredicts the diffusivity and conductivity. This can pose an important problem for batteries designed using simplified models, in which the overpredictions in diffusivity and conductivity lead to overpredictions in both energy and power performance. The battery pack may then have insufficient energy to meet the required range of the UAV, or insufficient power for the hybrid-electric aircraft to meet its rate of climb requirement.

The microscopic simulation results match well with experimental data obtained using two different measurement techniques, and domain size independence is achieved due to good agreement between the 80 particle and 640 particle cases. A proposed adjustment to the Bruggeman equation by changing the power value to $\alpha = 1.681$ is shown to match the simulation results with an R^2 value of about 0.89. In the graph analysis, three parameters based on the path length data within the microstructure are defined, and two are shown to be more strongly correlated with the computed effective transport coefficient than the porosity is. While these parameters are not included in the multi-scale model due to numerical complexity and a lack of experimental validation,

they do contribute important understanding of the underlying physics of the ion transport process in a porous medium, and provide guidelines for the manufacturing of tailored electrode materials. These results also suggest future research on the optimization of electrode microstructures using nanotechnology and nanomanufacturing capabilities, which may sufficiently improve the diffusivity and conductivity of high-voltage, high-capacity electrode materials to make them suitable for use in practical batteries. Such advances may allow significant gains in the effective transport coefficients, which as discussed in Chapter 4.5 are the fundamental mechanisms that govern battery performance. They are also a necessary supplement to cell-level optimization methods towards realizing the energy density values of 300-400 Wh/kg required to meet the performance goals documented in Chapter 1.3.5 of HALE flyers, hybrid-electric flyers, and UAV/MUAV/MAV, as well as reduce the weight and launch cost of LEO and GEO satellites.

As discussed previously, the surrogate modeling framework is applied to study the electrochemical reaction kinetics at the solid-liquid interface. A constraint on the overpotential is applied to the 8-variable design of experiments, and the resulting constraint space is found to be sufficiently broad to accommodate a large number of operating scenarios to be modeled. 18 REV realizations are selected, for which the simulation results are averaged to construct surrogate models to bridge the gap between the macroscopic and microscopic length scales. The use of a fixed solid volume fraction of 0.6 is a limitation in the approach, although results on a smaller number of cases show little influence of volume fraction on the relative sensitivities to the individual state variables. GSA performed using the surrogate model shows that of the 8 variables in the DOE, only 3 have a non-negligible influence on the interfacial reaction rate, namely the two-phase electric potentials and the SOC (or solid-phase ion concentration). The elimination of the other variables not only simplifies the problem, but is also able to effective filter noise in the simulation data, thus reducing the PRESS value of the kriging surrogate model by roughly half.

The chapter concludes with a demonstration of the completed multi-scale model and investigation of critical numerical issues. Due to numerical reasons related to the gradient definition, a PRS surrogate is used instead of the kriging model used to compute

the global sensitivity indices, although it is observed that the kriging model matches the microscopic simulations more closely. The reaction current density distribution within the electrodes is shown to be highly sensitive to the choice of open circuit voltage function due to the definition of the overpotential. However, this difference is shown to have little effect on the overall cell performance, as the total amount of charge within the electrode is conserved when the multi-scale model is completed (two-way coupling between the length scales). To further examine this effect, the Butler-Volmer equation is scaled by a constant factor k, with unity being the baseline case in the macro-homogeneous model. It is found that cell performance is reduced as k is decreased, but that very little is gained by increasing k by an order of magnitude. This suggests the existence of an electrochemical analogue to the critical diffusivity and conductivity values documented in previous chapters, and that its value is close to that for the material properties of $LiMn_2O_4$. The numerical robustness of the model implementation is also investigated by introducing a random perturbation to the Butler-Volmer equation. The computational time required to converge to a solution is found to increase substantially for both iterative and direct solvers, and divergence occurs at a perturbation amplitude of about $A = 0.6$.

Chapter 6.
Conclusions and Future Perspectives

This chapter summarizes the main conclusions drawn in the preceding chapters, and discusses the contributions of this dissertation. Several future directions for continuing battery research are also proposed.

6.1 Summary and Conclusions

In this dissertation, macro-homogeneous models, microscopic models, surrogate-based analysis, and gradient-based optimizers are applied towards meeting the objectives outlined in Chapter 1.4: to better understand the physical phenomena governing battery and cell performance by studying the relationship between battery operation, morphology, material properties, and energy density. In particular, this understanding is motivated by the performance requirements of several classes of aerospace systems such as hybrid-electric aircraft, UAV/MUAV/MAV, and satellites/spacecraft. In each of these systems, the energy density (specific energy) of existing batteries is shown to be a crucial limitation to the performance of the vehicle, and case studies using simplified and subsystem-level analysis are used to demonstrate the following:

i. A doubling of the energy density of the batteries from 200 to 400 Wh/kg would allow Helios to fly continuously without relying on hydrogen fuel cells, Solar Impulse to accommodate a second pilot for long-endurance missions, and the RQ-11 MUAV to carry a second payload device;

ii. Significant launch cost savings (order of millions of dollars) can be achieved due to weight reduction resulting from the higher energy density of existing lithium-ion batteries over Ni-H_2, but sufficient cycle life needs

to be proven;

iii. A hybrid-electric general aviation aircraft based on the Cessna 172 can achieve greater rates of climb than the conventional configuration (reaching cruise altitude in 30% less time) due to the additional power provided by the battery, but very little fuel is saved due to limitations to the controller model used in the analysis.

With the need for higher energy batteries for such aerospace systems established, and keeping in mind other design objectives such as power density and cycling life which may serve as constraints, the dissertation proceeds to address the objectives defined in Chapter 1.4 using surrogate modeling, optimization, and dimensional analysis tools. The key findings in Chapter 3 and Chapter 4 regarding battery physics are summarized here:

iv. Between the values 1 S/m and 100 S/m, the electronic conductivity of the $LiMn_2O_4$ particles is shown to have negligible influence on the energy density of the cell, regardless of which other design variables are considered;

v. The cell energy density becomes independent of the solid-phase diffusion coefficient in $LiMn_2O_4$ particles at a value of $D_{s,p} = 1.0\times10^{-13}$ m^2/s, allowing the design space to be split and the diffusion-independent region to be accurately modeled by fewer variables;

vi. Dimensionless parameters defined based on the solid-phase diffusivity and conductivity are able to characterize the maximum achievable energy density of multiple cathode materials ($LiMn_2O_4$, $LiFePO_4$, $LiCoO_2$, LiV_6O_{13}, and $LiTiS_2$) using an analytic generalized logistic function, allowing the easy calculation of maximum cycling rate and discharge current to retain good cell performance, for a given electrode material;

vii. The Pareto front quantifying the tradeoff between specific energy and specific power shows that power is much more sensitive to varying cycling rates than energy is, for cycling rates up to 4C (thus, moderately

high power can be achieved with little loss in energy) – however, at high cycling rates above 6C the trend is reversed, with incremental gains in power density accompanied by significant unavoidable losses in energy density;

viii. The addition of cathode thickness and porosity as design variables increases the maximum achievable energy density at all power density levels, with gains of 40% in energy density at high power levels – the inclusion of additional design variables are needed to enable the doubling in energy density required by solar flyers, electric flyers, and UAV;

ix. Global sensitivity analysis shows that from among the design variables considered, the cell energy density is most sensitive to the cycling rate, particle size and diffusivity, while porosity and thickness have a lesser but nonetheless still important effect;

x. Optimization results using gradient-based and surrogate-based methods show that the optimal values for electrode thickness and porosity depend on the values of other parameters such as cycling rate, particle size, and diffusivity – as the ratio of discharge to diffusion speeds increases, a thinner and more porous electrode is required to achieve optimal cell energy density.

These results provide contributions to several key steps of the design process of battery systems for aerospace vehicles, including the establishment and demonstration of systematic methods of comparing multiple electrode materials, quantifying the tradeoffs between multiple objectives such as energy and power, mapping the design space to determine the relationship between objective functions and design variables, and comparing the relative importance of multiple design variables on the objective function. However, for the objectives of this dissertation, these methods are limited by the homogenization simplifications in the existing macroscopic cell model, so Chapter 5 documents the development of a multi-scale model and its microscopic sub-models. The main findings related to battery physics obtained using the multi-scale model can be

summarized as follows:

xi. Microscopic simulation results from 2462 REV realizations of multiple domain sizes give consistent porosity-tortuosity relationships with two sets of experimental measurements, while showing that the Bruggeman equation used in the macro-homogeneous model consistently underpredicts tortuosity and thus overpredicts effective diffusivity/conductivity in the porous electrode;

xii. Significant scatter can be observed in the porosity-tortuosity data, suggesting that other factors besides mean porosity, such as particle orientation and alignment which can be calculated using algorithms based on graph theory, play a significant role in determining the transport properties within porous media;

xiii. A correction to the Bruggeman equation using a power α = 1.681 is proposed, which matches the data quite well (R^2 = 0.8941) for the amount of scatter resulting from the different microstructures obtained by randomly packing ellipsoidal particles;

xiv. Using GSA, the spatial gradients of the local state variables (ion concentration and electric potential in solid and liquid phases) have much less effect on the local electrochemical reaction current density at the solid-liquid interface, and thus a surrogate model with only 3 out of the 8 variables can be used to couple the microscopic and macroscopic models;

xv. Small differences in open circuit voltage lead to much larger differences in overpotential and local reaction current density, but the overall cell voltage is insensitive to these variations;

xvi. The cell voltage (and thus energy and power density) is also insensitive to small perturbations in the Butler-Volmer equation, suggesting the existence of a critical value for the interfacial electrochemical reaction rate, although cell voltage does drop as the magnitude of the kinetics

equation is reduced by orders of magnitude.

Throughout the processes of investigating the battery physics using surrogate-based and optimization tools, and of developing the multi-scale model, useful insights into numerical issues are also obtained. The most of these include the following:

xvii. Local refinement of a global surrogate model can merely shift model fidelity from one region to another, and for a large design space multiple local surrogates can provide much better accuracy than a single global surrogate;

xviii. Surrogate model accuracy can be significantly improved with multiple strategies, including reduction in the number of variables to reduce noise in the data, refinement of the design space by introducing additional sampling data, and optimizing the coefficients within the surrogate function to minimize some error function;

xix. The surrogate model is able to provide a computationally cheaper optimization solution than the gradient-based optimizer as it does not require conducting a cell simulation for each function evaluation, but its solution is only accurate to about 5-10% error;

xx. Due to the need for estimating gradients, several solvers are found to have significant difficulty converging when a random perturbation is introduced to the Butler-Volmer equation;

xxi. A kriging model is able to fit the microscopic simulation data for reaction current density with excellent accuracy but limited robustness, while a less accurate 4^{th}-order PRS model is selected to complete the multi-scale model due to its smoothness and robustness.

Ultimately, the most important contributions of this dissertation are the improved understanding of the physical phenomena that govern battery performance such as ion diffusion, electron conduction, electrochemical kinetics, and thermodynamics; and the

establishment and demonstration of frameworks for the efficient application of numerical tools to achieving further understanding of battery physics and improving battery design. It should be noted that these numerical frameworks are general and may be applied to other classes of batteries and battery materials, which may have higher capacity, higher voltage, or lower weight. One notable example is the lithium-metal battery in which the anode consists of a lithium metal foil, which has lower electric potential and weight than the graphite anode. Therefore, while the 750 Wh/kg energy density required by the NASA N+3 and SUGAR Volt programs is beyond the theoretical limits of the $LiMn_2O_4$ and LiC_6 electrodes, the insights obtained in this dissertation nonetheless represent an important step towards the complex process of achieving the necessary advances to meet the performance objectives for a range of aerospace vehicles and systems.

6.2 Future Work

The bulk of this dissertation focuses on improving the energy density of lithium-ion battery cells. However, as mentioned in Chapter 1.3, there are many other design objectives that must be satisfied in practical applications, such as safety, stability in the presence of varying environmental conditions, and cycle life. Two notable shortcomings that remain in the current battery modeling efforts are cell degradation and uncertainty quantification. Although models for predicting cell degradation and cycle life have been recently developed [151], they are generally based on empirical estimations from test data rather than on physics-based first principles. Recent developments into the modeling of specific mechanisms of cell degradation such as electro-thermal capacity fade [152] and solid-electrolyte interface (SEI) growth [153] hold significant promise, although they too are derived from a large amount of experimental data. A proper degradation model should also be sufficiently flexible to handle arbitrary cycling conditions. This is because degradation is a complex phenomenon caused by a multitude of concurrent mechanisms such as undesired secondary electrochemical reactions and internal cell resistance increases due to mechanical and thermal stress. As a result, battery systems in real world applications must undergo extensive characterization and life cycle testing due to the limitations in current modeling capabilities. Improvements to the cycle life of lithium-ion

batteries would also make them feasible for long life applications such as in satellites and spacecraft, which are currently forced to use batteries with lower energy and power capability. The accurate modeling of cell degradation is also required in order to properly analyze the tradeoffs between design variables and constraints. A promising path towards realizing this goal is to develop physics-based models for various degradation mechanisms, and to combine them with the existing multi-scale model using surrogate-based approaches. Such a model would allow numerical optimization methods to provide a much better starting design, thus substantially reducing the amount of testing required and improving the efficiency of the design process.

In addition to cell degradation, there exists considerable uncertainty in the quantification of certain material properties required by battery models, with experimental measurements for ion diffusivity and electron conductivity often differing by several orders of magnitude [94, 96]. While the approach used in this dissertation of simply ignoring this uncertainty and considering a wide range of values in the surrogate-based analysis can be used to efficiently identify a single optimum design, it provides limited information about how the battery would perform under non-ideal conditions. A probabilistic model that produces a range of expected performance outcomes based on uncertainty quantification of the input and design variables would provide a significant supplement to the existing tools in the design process. Improvements to the microstructure generation methodology would also be a valuable addition to the existing multi-cell model. Although the quasi-steady FEM simulations can be justified based on the relative magnitude of the relevant time scales for diffusion, conduction, and reaction, the present model does not account for the evolution of the microstructure which can result from mechanisms such as SEI growth and particle fracture as the battery is repeatedly cycled. This limitation would most likely also be best addressed using a probabilistic approach, in which a range of effective transport properties and morphology parameters are modeled.

Finally, the microscopic modeling efforts in this dissertation aim to generate realistic microstructures without any attempt to tailor the microstructure to aid in diffusion or interfacial reaction. Recent advances in the design of piezoelectric ceramic microstructures hold significant promise if similar techniques can be extended to battery

electrode materials [154]. The potential gains are especially significant if supplemented with advances in nanotechnology and manufacturing capabilities, and in fact it is widely believed that lithium-ion batteries based on nanomaterials will be the next step towards achieving the necessary performance improvements in the next generation of batteries [2]. The development of accurate modeling capabilities for arbitrary classes of microstructures (including those with polydisperse or non-ellipsoidal particles) would represent a critical step towards designing new high-capacity materials capable of achieving the necessary energy densities for future vehicle applications.

Appendix A.
Aircraft Kinematics and Flight Dynamics

A.1 Aerodynamic Forces

This appendix summarizes the aircraft kinematics and flight dynamics equations used to model the conventional and hybrid Cessna 172 configurations in Chapter 1.3.4. These equations are taken from McCormick [22] and Anderson [155], who have also provided a more detailed derivation of these equations and discussions of their relevance. The lift force L is related to the lift coefficient C_L by Eq. (A1).

$$L = \frac{1}{2}\rho V^2 S C_L \tag{A1}$$

The quantity $\frac{1}{2}\rho V^2$ is known as the dynamic pressure (where ρ is the air density and V is the aircraft velocity), and S is the reference area, which for an aircraft is typically the area of the wing. The lift coefficient has a linear dependence on the aircraft angle of attack α:

$$C_L = C_{L_0} + C_{L_\alpha}\alpha \tag{A2}$$

C_{L0} is the lift coefficient at zero angle of attack. A similar equation to (A1) can be written for the drag D:

$$D = \frac{1}{2}\rho V^2 S C_D \tag{A3}$$

Drag on an aircraft comes from two sources: parasitic drag due to skin friction and pressure, and induced drag due to lift. Hence the drag coefficient can be approximated by Eq. (A4).

$$C_D = C_{D_0} + KC_L^2 \tag{A4}$$

The constant K is determined empirically. For a Cessna 172, the values C_{D0} = 0.03 and K = 0.0373 are used.

A.2 Equations of Motion for Steady Flight

An aircraft can be described as a rigid body, and in this analysis the steady flight is considered such that the aircraft remains in a fixed vertical plane (steady longitudinal flight). There are four forces acting on an aircraft in steady longitudinal flight: lift, drag, thrust, and weight. The angle of attack α is defined as the angle between the thrust vector and the velocity vector, and the angle between the velocity vector and the horizontal axis (parallel to the ground) is the flight path angle γ. Assuming steady flight conditions, the sum of the forces along the velocity vector and parallel to the velocity vector must be zero, yielding Eqs. (A5) and (A6).

$$T\cos(\alpha) - D - mg\sin(\gamma) = 0 \tag{A5}$$

$$T\sin(\alpha) + L - mg\cos(\gamma) = 0 \tag{A6}$$

A.3 Steady Cruise

Under steady cruise conditions, the flight path angle is zero, and thus the above equations simplify to (A7) and (A8).

$$D = T \tag{A7}$$

$$L = mg \tag{A8}$$

Eqs. (A4) and (A8) can be combined to express the drag coefficient as a function of the aircraft weight:

$$C_D = C_{D_0} + \frac{4K(mg)^2}{\rho^2 V^4 S^2} \tag{A9}$$

From Eq. (A7), the power required to maintain steady level flight can also be obtained:

$$P = \frac{1}{2}\rho V^3 S C_{D_0} + \frac{2K(mg)^2}{\rho V S} \tag{A10}$$

Note that both terms in Eq. (A10) include the velocity *V*, suggesting a minimum power requirement with respect to *V*. By taking the derivative of (A10), the minimum power required, and the velocity for which this occurs, can be found:

$$P_{\min} = \frac{4}{3}\sqrt{\frac{2(mg)^3}{\rho S}}\sqrt{3K^3 C_{D_0}} \tag{A11}$$

$$V = \sqrt{\frac{2mg}{\rho S}}\sqrt{\frac{K}{3C_{D_0}}} \tag{A12}$$

Maximum range occurs when the ratio of lift to drag is maximized. By taking the derivative of Eq. (A4) with respect to C_L and setting to zero, the cruise condition in terms of C_L is obtained:

$$C_L = \sqrt{\frac{C_{D_0}}{K}} \tag{A13}$$

Finally, the velocity and corresponding power at cruise conditions are given by Eqs. (A14) and (A15).

$$V^* = \sqrt{\frac{2mg}{\rho S}}\sqrt{\frac{K}{C_{D_0}}} \tag{A14}$$

$$P = 4\sqrt{\frac{2(mg)^3}{3\rho S}}\sqrt{K^3 C_{D_0}} \tag{A15}$$

A.4 Steady Climb

In order to achieve the maximum rate of climb, the engine must be able to produce power in excess of the amount necessary to overcome drag. Therefore, it follows

that the maximum climb rate occurs when the maximum amount of power is provided by the engine, and the power required to overcome drag is minimized. From the analysis in the previous section, the power required to overcome drag is minimized at the velocity given in (A12). The maximum rate of climb is thus given by the excess power divided by the weight of the aircraft:

$$V_{climb,\max} = \frac{P_{\max} - \frac{4}{3}\sqrt{\frac{2(mg)^3}{\rho S}\sqrt{3K^3 C_{D_0}}}}{mg} \tag{A16}$$

Bibliography

[1] J. M. Tarascon and M. Armand, "Issues and challenges facing rechargeable lithium batteries," *Nature,* vol. 414, pp. 359-367, 2001.

[2] M. Armand and J. M. Tarascon, "Building better batteries," *Nature,* vol. 451, pp. 652-657, 2008.

[3] J. R. Owen, "Rechargeable lithium batteries," *Chemical Society Review,* vol. 26, pp. 259-267, 1997.

[4] N. A. Owen, O. R. Inderwildi and D. A. King, "The status of conventional world oil reserves--Hype or cause for concern," *Energy Policy,* vol. 38, pp. 4743-4749, 2010.

[5] "Research and Innovative Technology Administration," Bureau of Transportation Statistics, [Online]. Available: http://www.transtats.bts.gov/fuel.asp. [Accessed 19 March 2013].

[6] X. Olsthoom, "Carbon dioxide emissions from international aviation: 1950-2050," *Journal of Air Transport Management,* vol. 7, pp. 87-93, 2001.

[7] K. Mayor and R. S. J. Tol, "Scenarios of carbon dioxide emissions from aviation," *Global Environmental Change,* vol. 20, pp. 65-73, 2010.

[8] S. Chu and A. Majumdar, "Opportunities and challenges for a sustainable energy future," *Nature,* vol. 488, pp. 294-303, 2012.

[9] D. Linden and T. B. Reddy, Handbook of Batteries, New York: McGraw-Hill, 2002.

[10] P. C. Howlett, D. R. MacFarlane and A. F. Hollenkamp, "High lithium metal cycling efficiency in a room-temperature ionic liquid," *Electrochemical and Solid-State Letters,* vol. 7, pp. A97-A101, 2004.

[11] B. Scrosati and J. Garche, "Lithium batteries: status, prospects and future," *Journal of Power Sources,* vol. 195, pp. 2419-2430, 2010.

[12] G. M. Stone, S. A. Mullin, A. A. Teran, D. R. Hallinan, A. M. Minor, A. Hexemer and N. P. Balsara, "Resolution of the modulus versus adhesion dilemma in solid polymer electrolytes for rechargeable lithium metal batteries," *Journal of the Electrochemical Society,* vol. 159, pp. A222-A227, 2012.

[13] R. R. Mitchell, B. M. Gallant, C. V. Thompson and Y. Shao-Horn, "All-carbon-nanofiber electrodes for high-energy rechargeable Li-O2 batteries," *Energy & Environmental Science,* vol. 4, pp. 2952-2958, 2011.

[14] G. Girishkumar, B. McCloskey, A. C. Luntz, S. Swanson and W. Wilcke, "Lithium-ion battery: Promise and challenges," *The Journal of Physical Chemistry Letters,* vol. 1, pp. 2193-2203, 2010.

[15] J. P. Thomas and M. A. Qidwai, "The design and application of multifunctional structure-battery materials systems," *JOM Journal of the Minerals, Metals and Materials Society,* vol. 3, pp. 18-24, 2005.

[16] M. Sinnett, "787 no-bleed systems: saving fuel and enhancing operational efficiencies," Boeing, [Online]. Available: http://www.boeing.com/commercial/aeromagazine/articles/qtr_4_07/AERO_Q407_article2.pdf. [Accessed 16 May 2013].

[17] "Dreamliner: Boeing 787 planes grounded on safety fears," BBC Business News, 17 January 2013. [Online]. Available: http://www.bbc.co.uk/news/business-21054089. [Accessed 16 May 2013].

[18] C. H. Henry, "Limiting efficiencies of ideal single and multiple energy gap terrestrial solar cells," *Journal of Applied Physics,* vol. 51, pp. 4494-4500, 1980.

[19] "Helios Prototype Fact Sheet," NASA Dryden, [Online]. Available: http://www.nasa.gov/centers/dryden/news/FactSheets/FS-068-DFRC.html. [Accessed 5 May 2013].

[20] W. Shyy, Aerodynamics of low Reynolds number flyers, Cambridge University Press, 2008.

[21] "Technical Specifications, Raven RQ-11B," AeroVironment Inc., [Online]. Available: http://www.avinc.com/downloads/AV_RAVEN-DOM_V10109.pdf. [Accessed 5 May 2013].

[22] B. W. McCormick, Aerodynamics, aeronautics, and flight mechanics, New York: Wiley, 1995.

[23] J. P. Fellner, G. J. Loeber, S. P. Vukson and C. A. Riepenhoff, "Lithium ion testing for spacecraft applications," *Journal of Power Sources,* vol. 119, pp. 911-

913, 2003.

[24] "Hubble Essentials: Quick Facts," Hubble Site, [Online]. Available: http://hubblesite.org/the_telescope/hubble_essentials/quick_facts.php. [Accessed 6 May 2013].

[25] W. J. Larson and J. R. Wertz, Space mission analysis and design, Torrance: Microcosm, Inc., 1992.

[26] D. E. Koelle, "Specific transportation costs to GEO - past, present and future," *Acta Astronautica,* vol. 53, pp. 797-803, 2003.

[27] "Boeing 702HP Fleet," Boeing, [Online]. Available: http://www.boeing.com/boeing/defense-space/space/bss/factsheets/702/702fleet.page. [Accessed 6 May 2013].

[28] S. Asif, Evolutionary computation based multi-objective design search and optimization of spacecraft electrical power subsystems (Doctoral dissertation), University of Glasgow, 2008.

[29] D. Yaakov, Y. Gofer, D. Aurbach and I. C. Halalay, "On the study of electrolyte solutions for Li-ion batteries that can work over a wide temperature range," *Journal of the Electrochemical Society,* vol. 157, pp. A1383-A1391, 2010.

[30] C. Li, L. Gu, S. Tsukimoto, P. A. van Aken and J. Maier, "Low-temperature ionic-liquid-based synthesis of nanostructured iron-based fluoride cathodes for lithium batteries," *Advanced Materials,* vol. 22, pp. 3650-3654, 2010.

[31] "Skyhawk," Cessna, [Online]. Available: http://www.cessna.com/single-engine/skyhawk. [Accessed 9 March 2011].

[32] M. Bradley, C. Droney, D. Paisley, B. Roth, S. Gowda and M. Kirby, "NASA N+3 subsonic ultra green aircraft research SUGAR final review," Boeing Research and Technology Presentation, 2010.

[33] B. Haran, B. N. Popov and R. E. White, "Determination of the hydrogen diffusion coefficient in metal hydrides by impedance spectroscopy," *Journal of Power Sources,* vol. 75, pp. 56-63, 1998.

[34] S. Santhanagopalan, Q. Guo and R. E. White, "Parameter estimation and model discrimination for a lithium-ion cell," *Journal of the Electrochemical Society,* vol. 154, pp. A198-A206, 2007.

[35] W. Luo, C. Lyu, L. Wang and L. Zhang, "A new extension of physics-based single particle model for higher charge-discharge rates," *Journal of Power Sources,* vol.

241, pp. 295-310, 2013.

[36] M. W. Verbrugge and R. S. Conell, "Electrochemical and thermal characterization of battery modules commensurate with electric vehicle integration," *Journal of the Electrochemical Society,* vol. 149, pp. A45-A53, 2002.

[37] B. Y. Liaw, G. Nagasubramanian, R. G. Jungst and D. H. Doughty, "Modeling of lithium ion cells--a simple equivalent-circuit model approach," *Solid State Ionics,* vol. 175, pp. 835-839, 2004.

[38] P. Ramadass, B. Haran, R. E. White and B. N. Popov, "Mathematical modeling of the capacity fade of Li-ion cells," *Journal of Power Sources,* vol. 123, pp. 230-240, 2003.

[39] X. Zhang, W. Shyy and A. M. Sastry, "Numerical simulation of intercalation-induced stress in Li-ion battery electrode particles," *Journal of the Electrochemical Society,* vol. 154, pp. A910-A916, 2007.

[40] X. Zhang, A. M. Sastry and W. Shyy, "Intercalation-induced stress and heat generation within single lithium-ion battery electrode particles," *Journal of the Electrochemical Society,* vol. 155, pp. A542-A552, 2008.

[41] C. W. Wang and A. M. Sastry, "Mesoscale modeling of a Li-ion polymer cell," *Journal of the Electrochemical Society,* vol. 154, pp. A1035-A1047, 2007.

[42] V. Ramadesigan, V. Boovaragavan, J. C. Pirkle and V. R. Subramanian, "Efficient reformulation of solid-phase diffusion in physics-based lithium-ion battery models," *Journal of the Electrochemical Society,* vol. 157, pp. A854-A860, 2010.

[43] P. W. C. Northrop, V. Ramadesigan, S. De and V. R. Subramanian, "Coordinate transformation, orthogonal collocation, model reformulation and simulation of electrochemical-thermal behavior of lithium-ion battery stacks," *Journal of the Electrochemical Society,* vol. 158, pp. A1461-A1477, 2011.

[44] M. Doyle, T. F. Fuller and J. Newman, "Modeling of galvanostatic charge and discharge of the lithium/polymer/insertion cell," *Journal of the Electrochemical Society,* vol. 140, pp. 1526-1533, 1993.

[45] T. F. Fuller, M. Doyle and J. Newman, "Simulation and optimization of the dual lithium ion insertion cell," *Journal of the Electrochemical Society,* vol. 141, pp. 1-10, 1994.

[46] M. Doyle, J. Newman, A. S. Gozdz, C. N. Schmutz and J. M. Tarascon, "Comparison of modeling predictions with experimental data from plastic lithium

ion cells," *Journal of the Electrochemical Society,* vol. 143, pp. 1890-1903, 1996.

[47] W. Du, A. Gupta, X. Zhang, A. M. Sastry and W. Shyy, "Effect of cycling rate, particle size and transport properties on lithium-ion cathode performance," *International Journal of Heat and Mass Transfer*, vol. 53, pp. 3552-3561, 2010.

[48] S. Yu, Y. Chung, M. S. Song, J. H. Nam and W. I. Cho, "Investigation of design parameter effects on high current performance of lithium-ion cells with LiFePO4/graphite electrodes," *Journal of Applied Electrochemistry,* vol. 42, pp. 443-453, 2012.

[49] C. C. Tseng and W. Shyy, "Modeling for isothermal and cryogenic cavitation," *International Journal of Heat and Mass Transfer,* vol. 53, pp. 513-525, 2010.

[50] T. Goel, D. J. Dorney, R. T. Haftka and W. Shyy, "Improving the hydrodynamic performance of diffuser vanes via shape optimization," *Computers and Fluids,* vol. 37, pp. 705-723, 2008.

[51] R. P. Liem, G. K. W. Kenway and J. R. R. A. Martins, "Multi-point, multi-mission, high-fidelity aerostructural optimization of a long-range aircraft configuration," in *14th AIAA/ISSMO Multidisciplinary Analysis and Optimization Conference*, Indianapolis, 2012.

[52] W. Shyy, Y. C. Cho, W. Du, A. Gupta, C. C. Tseng and A. M. Sastry, "Surrogate-based modeling and dimension reduction techniques for multi-scale mechanics problems," *Acta Mechanica Sinica,* vol. 27, pp. 845-865, 2011.

[53] Y. C. Cho, W. Du, A. Gupta, W. Shyy, A. M. Sastry and C. C. Tseng, "Surrogate-based modeling and multi-objective optimization techniques for thermo-fluid & energy systems," in *Second International Conference on Computational Methods for Thermal Problems,* Dalian, China, 2011.

[54] N. Papila, W. Shyy, L. Griffin and D. J. Dorney, "Shape optimization of supersonic turbines using global approximation methods," *Journal of Propulsion and Power,* vol. 18, pp. 509-518, 2002.

[55] W. Shyy, N. Papila, R. Vaidyanathan and P. K. Tucker, "Global design optimization for aerodynamics and rocket propulsion components," *Progress in Aerospace Sciences,* vol. 37, pp. 59-118, 2001.

[56] D. W. Kim and J. Lee, "An improvement of kriging based sequential approximate optimization method via extended use of design experiments," *Engineering Optimization*, vol. 42, pp. 1133-1149, 2010.

[57] A. Gupta, J. H. Seo, X. Zhang, W. Du, A. M. Sastry and W. Shyy, "Effective transport properties of LiMn2O4 electrode via particle-scale modeling," *Journal of the Electrochemical Society,* vol. 158, pp. A487-A497, 2011.

[58] M. D. McKay, R. J. Beckman and W. J. Conover, "A comparison of three methods of selecting values of input variables in the analysis of output from a computer code," *Technometrics,* vol. 21, pp. 239-245, 1979.

[59] R. H. Myers and D. C. Montgomery, Response Surface Methodology: Process and Product in Optimization Using Designed Experiments, New York: Wiley and Sons Inc., 1995.

[60] L. Kuipers and H. Niederreiter, Uniform Distribution of Sequences, Courier Dover Publications, 2006.

[61] D. R. Zones, "A taxonomy of global optimization methods based on response surfaces," *Journal of Global Optimization,* vol. 21, pp. 345-383, 2001.

[62] J. Sacks, W. J. Welch, T. J. Mitchell and H. P. Wynn, "Design and analysis of computer experiments," *Statistical Science,* vol. 4, pp. 409-435, 1989.

[63] S. N. Lophaven, H. B. Nielsen and J. Sondergaard, "DACE - A Matlab kriging toolbox. Version 2.0," Technical University of Denmark, Denmark, 2002.

[64] T. Goel, R. T. Haftka, W. Shyy and N. V. Queipo, "Ensemble of surrogates," *Structural and Multidisciplinary Optimization,* vol. 33, pp. 199-216, 2007.

[65] T. Goel, R. T. Haftka and W. Shyy, "Comparing error estimation measures for polynomial and kriging approximation of noise-free functions," *Structural and Multidisciplinary Optimization,* vol. 38, pp. 429-442, 2009.

[66] M. Meckesheimer, A. J. Booker, R. R. Barton and T. W. Simpson, "Computationally inexpensive metamodel assessment strategies," *AIAA Journal,* vol. 40, pp. 2053-2060, 2002.

[67] I. Sobol, "Sensitivity estimates for non-linear mathematical models," *Mathematical Modelling and Computational Experiments,* vol. 4, pp. 407-414, 1993.

[68] A. Saltelli, S. Tarantola and K. P. S. Chan, "A quantitative model-independent method for global sensitivity analysis of model output," *Technometrics,* vol. 41, pp. 39-56, 1999.

[69] Y. Mack, T. Goel, W. Shyy and R. Haftka, "Surrogate model-based optimization framework: a case study in aerospace design," in *Evolutionary Computation in*

Dynamic and Uncertain Environments, Berlin Heidelberg, Springer, 2007, pp. 323-342.

[70] H. W. Kuhn and A. W. Tucker, "Nonlinear programming," in *Proceedings of the Second Berkeley Symposium on Mathematical Statistics and Probability*, 1951.

[71] J. A. Nelder and R. Mead, "A simplex method for function minimization," *The Computer Journal*, vol. 7, pp. 308-313, 1965.

[72] J. Kennedy and R. C. Eberhart, "Particle swarm optimization," *Proceedings, IEEE International Conference on Neural Networks*, vol. 4, pp. 1942-1948, 1995.

[73] D. W. Zingg, M. Nemec and T. H. Pulliam, "A comparative evaluation of genetic and gradient-based algorithms applied to aerodynamic optimization," *European Journal of Computational Mechanics*, vol. 17, pp. 103-126, 2008.

[74] R. Fletcher and M. J. D. Powell, "A rapidly convergent descent method for minimization," *The Computer Journal*, vol. 6, pp. 163-168, 1963.

[75] P. E. Gill, W. Murray and M. A. Saunders, "SNOPT: an SQP algorithm for large-scale constrained optimization," *SIAM Journal on Optimization*, vol. 12, pp. 979-1006, 2002.

[76] M. J. D. Powell, "A fast algorithm for nonlinearly constrained optimization calculations," in *Lecture Notes in Mathematics (Numerical Analysis)*, Berlin Heidelberg New York, Springer, 1978, pp. 144-157.

[77] J. R. R. A. Martins, P. Sturdza and J. J. Alonso, "The complex-step derivative approximation," *ACM Transactions on Mathematical Software*, vol. 29, pp. 245-262, 2003.

[78] N. Xue, W. Du, A. Gupta, W. Shyy, A. M. Sastry and J. R. R. A. Martins, "Optimization of a single lithium-ion battery cell with a gradient-based algorithm," *Journal of the Electrochemical Society*, vol. 160, pp. A1071-A1078, 2013.

[79] D. Kehrwald, P. R. Shearing, N. P. Brandon, P. K. Sinha and S. J. Harris, "Local tortuosity inhomogeneities in a lithium battery composite electrode," *Journal of the Electrochemical Society*, vol. 158, pp. A1393-A1399, 2011.

[80] K. K. Patel, J. M. Paulsen and J. Desilvestro, "Numerical simulation of porous networks in relation to battery electrodes and separators," *Journal of Power Sources*, vol. 122, pp. 144-152, 2003.

[81] A. Donev, S. Torquato and F. H. Stillinger, "Neighbor list collision-driven molecular dynamics simulation for nonspherical hard particles. I. Algorithmic

details," *Journal of Computational Physics,* vol. 202, pp. 737-764, 2005.

[82] S. J. Hollister, J. M. Brennan and N. Kikuchi, "A homogenization sampling procedure for calculating trabecular bone effective stiffness and tissue level stress," *Journal of Biomechanics,* vol. 27, pp. 433-444, 1994.

[83] K. Koketsu, H. Fujiwara and Y. Ikegami, "Finite-element simulation of seismic ground motion with a voxel mesh," *Pure and Applied Geophysics,* vol. 161, pp. 2183-2198, 2004.

[84] D. B. West, Introduction to Graph Theory, Prentice Hall, 2001.

[85] I. V. Thorat, D. E. Stephenson, N. A. Zacharias, K. Zaghib, J. N. Harb and D. R. Wheeler, "Quantifying tortuosity in porous Li-ion battery materials," *Journal of Power Sources,* vol. 188, pp. 592-600, 2009.

[86] C. H. Lu and S. W. Lin, "Influence of the particle size on the electrochemical properties of lithium manganese oxide," *Journal of Power Sources,* vol. 97, pp. 458-460, 2001.

[87] T. Drezen, N. H. Kwon, P. Bowen, I. Teerlinck, M. Isono and I. Exnar, "Effect of particle size on LiMnPO4 cathode," *Journal of Power Sources,* vol. 174, pp. 949-953, 2007.

[88] T. D. Tran, J. H. Feikert, R. W. Pekala and K. Kinoshita, "Rate effect of lithium-ion graphite electrode performance," *Journal of Applied Electrochemistry,* vol. 26, pp. 1161-1167, 1996.

[89] S. Ahn, Y. Kim, K. J. Kim, T. H. Kim, H. Lee and M. H. Kim, "Development of high capacity, high rate lithium ion batteries utilizing metal fiber conductive additives," *Journal of Power Sources,* vol. 81, pp. 896-901, 1999.

[90] R. E. Garcia, Y. M. Chiang, W. C. Carter, P. Limthongkul and C. M. Bishop, "Microstructural modeling and design of rechargeable lithium-ion batteries," *Journal of the Electrochemical Society,* vol. 152, pp. A255-A263, 2005.

[91] R. Darling and J. Newman, "Modeling a porous intercalation electrode with two characteristic particle sizes," *Journal of the Electrochemical Society,* vol. 144, pp. 4201-4208, 1997.

[92] D. Guyomard and J. M. Tarascon, "Rechargeable Li1+xMn2O4/carbon cels with a new electrolyte composition: potentiostatic studies and application to practical cells," *Journal of the Electrochemical Society,* vol. 140, pp. 3071-3081, 1993.

[93] M. D. Levi and D. Aurbach, "Diffusion coefficients of lithium ions during intercalation into graphite derived from the simultaneous measurements and modeling of electrochemical impedance and potentiostatic intermittent titration characteristics of thin graphite electrodes," *Journal of Physical Chemistry B,* vol. 101, pp. 4641-4647, 1997.

[94] D. Zhang, B. N. Popov and R. E. White, "Modeling lithium intercalation of a single spinel particle under potentiodynamic control," *Journal of the Electrochemical Society,* vol. 147, pp. 831-838, 2000.

[95] J. R. Dygas, M. Kopec, F. Krok, D. Lisovytskiy and J. Pielaszek, "Conductivity and dielectric relaxation of phenomena in lithium manganese spinel," *Solid State Ionics,* vol. 176, pp. 2153-2161, 2005.

[96] Y. H. Chen, C. W. Wang, X. Zhang and A. M. Sastry, "Porous cathode optimization for lithium cells: ionic and electronic conductivity, capacity, and selection of materials," *Journal of Power Sources,* vol. 195, pp. 2851-2862, 2010.

[97] P. Arora, R. E. White and M. Doyle, "Capacity fade mechanisms and side reactions in lithium-ion batteries," *Journal of the Electrochemical Society,* vol. 145, pp. 3647-3667, 1998.

[98] W. Du, N. Xue, A. Gupta, A. M. Sastry, J. R. R. A. Martins and W. Shyy, "Optimization of LiMn2O4 electrode properties in a gradient- and surrogate-based framework," *Acta Mechanica Sinica,* vol. 29, pp. 335-347, 2013.

[99] W. Du, N. Xue, A. M. Sastry, J. R. R. A. Martins and W. Shyy, "Energy density comparison of Li-ion cathode materials using dimensional analysis," *Journal of the Electrochemical Society,* vol. 160, pp. A1187-A1193, 2013.

[100] J. Crank and P. Nicolson, "A practical method for numerical evaluation of solutions of partial differential equations of the heat-conduction type," *Mathematical Proceedings of the Cambridge Philosophical Society,* vol. 43, pp. 50-67, 1947.

[101] M. Park, X. Zhang, M. Chung, G. B. Less and A. M. Sastry, "A review of conduction phenomena in Li-ion batteries," *Journal of Power Sources,* vol. 195, pp. 7904-7929, 2010.

[102] J. Cho, H. Kim and B. Park, "Comparison of overcharge behavior of AlPO4-coated LiCoO2 and LiNi0.8Co0.1Mn0.1O2 cathode materials in Li-ion cells," *Journal of the Electrochemical Society,* vol. 151, pp. A1707-A1711, 2004.

[103] D. D. MacNeil, Z. Lu, Z. Chen and J. R. Dahn, "A comparison of the electrode/electrolyte reaction at elevated temperatures for various Li-ion battery

cathodes," *Journal of Power Sources,* vol. 108, pp. 8-14, 2002.

[104] W. F. Howard and R. M. Spotnitz, "Theoretical evaluation of high-energy lithium metal phosphate cathode materials in Li-ion batteries," *Journal of Power Sources,* vol. 165, pp. 887-891, 2007.

[105] M. Doyle and J. Newman, "Analysis of capacity-rate data for lithium batteries using simplified models of the discharge process," *Journal of Applied Electrochemistry,* vol. 27, pp. 846-856, 1997.

[106] H. L. Langhaar, Dimensional Analysis and Theory of Models, New York: Wiley and Sons Inc., 1951.

[107] M. Y. Saidi, J. Barker and R. Koksbang, "Thermodynamic and kinetic investigation of lithium insertion in the Li1-xMn2O4 spinel phase," *Journal of Solid State Chemistry,* vol. 122, pp. 195-199, 1996.

[108] K. Dokko, M. Nishizawa, M. Mohamedi, M. Umeda, I. Uchida, J. Akimoto, Y. Takahashi, Y. Gotoh and S. Mizuta, "Electrochemical studies of Li-ion extraction and insertion of LiMn2O4 single crystal," *Electrochemical and Solid-State Letters,* vol. 4, pp. A151-A153, 2001.

[109] F. Cao and J. Prakash, "A comparative electrochemical study of LiMn2O4 spinel thin-film and porous laminate," *Electrochemica Acta,* vol. 47, pp. 1607-1613, 2002.

[110] J. Marzec, K. Swierczek, J. Przewoznik, J. Molenda, D. R. Simon, E. M. Kelder and J. Schoonman, "Conduction mechanism in operating a LiMn2O4 cathode," *Solid State Ionics,* vol. 146, pp. 225-237, 2002.

[111] M. Gaberscek, R. Dominko and J. Jamnik, "Is small particle size more important than carbon coating? An example study on LiFePO4 cathodes," *Electrochemistry Communications,* vol. 9, pp. 2778-2783, 2007.

[112] R. Amin, P. Balaya and J. Maier, "Anisotropy of electronic and ionic transport in LiFePO4 single crystals," *Electrochemical and Solid-State Letters,* vol. 10, pp. A13-A16, 2007.

[113] R. Amin, C. Lin and J. Maier, "Aluminium-doped LiFePO4 single crystals Part I. Growth, characterization and total conductivity," *Physical Chemistry Chemical Physics,* vol. 10, pp. 3519-3523, 2008.

[114] S. L. Bewlay, K. Konstantinov, G. W. Wang, S. X. Dou and H. K. Liu, "Conductivity improvements to spray-produced LiFePO4 for addition of a carbon

source," *Materials Letters,* vol. 11, pp. 1788-1791, 2004.

[115] S. H. Choi, J. W. Son, Y. S. Yoon and J. Kim, "Particle size effects on temperature-dependent performance of LiCoO2 in lithium batteries," *Journal of Power Sources,* vol. 158, pp. 1419-1424, 2006.

[116] A. Van der Ven and G. Ceder, "Lithium diffusion in layered LixCoO2," *Electrochemical and Solid-State Letters,* vol. 3, pp. 301-304, 2000.

[117] J. Xie, N. Imanishi, T. Matsumura, A. Hirano, Y. Takeda and O. Yamamoto, "Orientation dependence of Li-ion diffusion kinetics in LiCoO2 thin films prepared by RF magnetron sputtering," *Solid State Ionics,* vol. 9, pp. 362-370, 2008.

[118] Y. I. Jang, B. J. Neudecker and N. J. Dudney, "Lithium diffusion in LixCoO2 (0.45<x<0.7) intercalation cathodes," *Electrochemical and Solid-State Letters,* vol. 4, pp. A74-A77, 2001.

[119] Y. Takahashi, N. Kijima, K. Tokiwa, T. Watanabe and J. Akimoto, "Single-crystal synthesis, structure refinement and electrical properties of Li0.5CoO2," *Journal of Physics: Condensed Matter,* vol. 19, p. 436202, 2007.

[120] G. Pistoia, M. Pasquali, Y. Geronov, V. Manev and R. V. Moshtev, "Small particle-size lithium vanadium oxide: an improved cathode material for high rate rechargeable lithium batteries," *Journal of Power Sources,* vol. 27, pp. 35-43, 1989.

[121] C. Lampe-Onnerud, J. O. Thomas, M. Hardgrave and S. Yde-Andersen, "The performance of single-phase V6O13 in the lithium/polymer electrolyte battery," *Journal of the Electrochemical Society,* vol. 142, pp. 3648-3651, 1995.

[122] P. C. Spurdens and B. C. H. Steele, "An investigation of lithium transport properties in V6O13 single crystals," *Solid State Ionics,* vol. 21, pp. 151-158, 1986.

[123] D. Zehnder, C. Deshpandey, B. Dunn and R. F. Bunshah, "Transport properties of thin film TiS2 produced by are," *Solid State Ionics,* vol. 18, pp. 813-817, 1986.

[124] C. Julien, I. Samaras, O. Gorochov and A. M. Ghorayeb, "Optical and electrical-transport studies on lithium-intercalated TiS2," *Physical Review B,* vol. 45, p. 13390, 1992.

[125] A. Van der Ven, J. C. Thomas, Q. Xu, B. Swoboda and D. Morgan, "Nondilute diffusion from first principles: Li diffusion in LixTiS2," *Physical Review B,* vol.

78, p. 104306, 2008.

[126] G. B. Less, J. H. Seo, S. Han, A. M. Sastry, J. Zausch, A. Latz, S. Schmidt, C. Wieser, D. Kehrwald and S. Fell, "Micro-scale modeling of Li-ion batteries: parameterization and validation," *Journal of the Electrochemical Society,* vol. 159, pp. A697-A704, 2012.

[127] M. Zhu, J. Park and A. M. Sastry, "Particle interaction and aggregation in cathode material of Li-ion batteries: a numerical study," *Journal of the Electrochemical Society,* vol. 158, pp. A1155-A1159, 2011.

[128] F. J. Richards, "A flexible growth function for empirical use," *Journal of Experimental Biology,* vol. 10, pp. 290-301, 1959.

[129] M. Z. A. Munshi and B. B. Owens, "Assessment of thin film batteries based on polymer electrolytes. I. Energy density.," *Solid State Ionics,* vol. 38, pp. 87-94, 1990.

[130] K. Brandt, "Historical development of secondary lithium batteries," *Solid State Ionics,* vol. 69, pp. 173-183, 1994.

[131] W. Du, A. Gupta, N. Xue, J. R. R. A. Martins, A. M. Sastry and W. Shyy, "Microscopic scale modeling of effective transport properties in Li-ion cathodes with network theory," in *221st Meeting of the Electrochemical Society,* Seattle, 2012.

[132] W. Du, N. Xue, A. M. Sastry, J. R. R. A. Martins and W. Shyy, "Scale bridging via surrogate modeling for multi-scale analysis of Li-ion cathodes," in *Pacific Rim Meeting on Electrochemical and Solid-State Science*, Honolulu, 2012.

[133] E. Sozer and W. Shyy, "Multi-scale thermo-fluid transport in porous media," *International Journal of Numerical Methods for Heat & Fluid Flow,* vol. 18, pp. 883-899, 2008.

[134] R. E. Meredith and C. W. Tobias, "Conduction in heterogeneous systems," *Advances in electrochemistry and electrochemical engineering,* vol. 2, pp. 15-47, 1962.

[135] Y. Saad and M. H. Schultz, "GMRES: a generalized minimal residual algorithm for solving nonsymmetric linear systems," *SIAM Journal on Scientific and Statistical Computing,* vol. 7, pp. 856-869, 1986.

[136] O. Axelsson, "A generalized SSOR method," *BIT Numerical Mathematics,* vol. 12, pp. 443-467, 1972.

[137] R. Fletcher, "Conjugate gradient methods for indefinite systems," in *Numerical Analysis,* Berlin Heidelberg, Springer, 1976, pp. 73-89.

[138] K. Stuben, "A review of algebraic multigrid," *Journal of Computational and Applied Mathematics,* vol. 128, pp. 281-309, 2001.

[139] B. Vijayaraghavan, D. R. Ely, Y. M. Chiang, R. Garcia-Garcia and R. E. Garcia, "An analytical method to determine tortuosity in rechargeable battery electrodes," *Journal of the Electrochemical Society,* vol. 159, pp. A548-A552, 2012.

[140] Z. Yu and R. N. Carter, "Measurement of effective oxygen diffusivity in electrodes for proton exchange membrane fuel cells," *Journal of Power Sources,* vol. 195, pp. 1079-1084, 2010.

[141] A. Yamada, S. C. Chung and K. Hinokuma, "Optimized LiFePO4 for lithium battery cathodes," *Journal of the Electrochemical Society,* vol. 148, pp. A224-A229, 2001.

[142] S. Golmon, K. Maute and M. L. Dunn, "Numerical modeling of electrochemical-mechanical interactions in lithium polymer batteries," *Computers and Structures,* vol. 87, pp. 1567-1579, 2009.

[143] T. Mori and K. Tanaka, "Average stress in matrix and average elastic energy of materials with misfitting inclusions," *Acta Metalligurca,* vol. 21, pp. 571-574, 1973.

[144] S. Golmon, K. Maute and M. L. Dunn, "Multiscale design optimization of lithium ion batteries using adjoint sensitivity analysis," *International Journal of Numerical Methods in Engineering,* vol. 92, pp. 475-494, 2012.

[145] X. Xiao, W. Wu and X. Huang, "A multi-scale approach for the stress analysis of polymeric separators in a lithium-ion battery," *Journal of Power Sources,* vol. 195, pp. 7649-7660, 2010.

[146] G. H. Kim, K. Smith, K. J. Lee, S. Santhanagopalan and A. Pesaran, "Multi-domain modeling of lithium-ion batteries encompassing multi-physics at varied length scales," *Journal of the Electrochemical Society,* vol. 158, pp. A955-A969, 2011.

[147] A. Awarke, S. Lauer, M. Wittler and S. Pischinger, "Quantifying the effects of strains on the conductivity and porosity of LiFePO4 based Li-ion composite cathodes using a multi-scale approach," *Computational Materials Science,* vol. 50, pp. 871-879, 2011.

[148] Q. H. Zeng, A. B. Yu and G. Q. Lu, "Multiscale modeling and simulation of polymer nanocomposites," *Progress in Polymer Science,* vol. 33, pp. 191-269, 2008.

[149] A. A. Franco, "Multiscale modelling and numerical simulation of rechargeable lithium ion batteries: concepts, methods and challenges," *RSC Advances,* 2013.

[150] M. Yonemura, A. Yamada, Y. Takei, N. Sonoyama and R. Kanno, "Comparative kinetic study of olivine LixMPO4 (M= Fe, Mn)," *Journal of the Electrochemical Society,* vol. 151, pp. A1352-A1356, 2004.

[151] M. Ecker, J. B. Gerschler, J. Vogel, S. Kabitz, F. Hust, P. Dechent and D. U. Sauer, "Development of a lifetime prediction models for lithium-ion batteries based on extended accelerated aging test data," *Journal of Power Sources,* vol. 215, pp. 248-257, 2012.

[152] Y. Ye, Y. Shi and A. A. O. Tay, "Electro-thermal cycle life model for lithium iron phosphate battery," *Journal of Power Sources,* vol. 217, pp. 509-518, 2012.

[153] A. Awarke, S. Pischinger and J. Ogrzewalla, "Pseudo 3D modeling and analysis of the SEI growth distribution in large format Li-ion polymer pouch cells," *Journal of the Electrochemical Society,* vol. 160, pp. A172-A181, 2013.

[154] S. B. Lee, T. S. Key, Z. Liang, R. E. Garcia, S. Wang, X. Tricoche, G. S. Rohrer, Y. Saito, C. Ito and T. Tani, "Microstructure design of lead-free piezoelectric ceramics," *Journal of the European Ceramic Society,* vol. 33, pp. 313-326, 2013.

[155] J. D. Anderson, Aircraft performance and design, New York: McGraw-Hill, 1999.